# Study of Dynamics and Structure of Anisotropic Colloidal Suspensions using Confocal Laser Scanning Microscopy

**by**

**Deshpremy Mukhija**

A dissertation submitted in partial fulfillment
of the requirements for the degree of
Doctor of Philosophy
(Chemical Engineering)
in The University of Michigan
2009

Doctoral Committee:

Associate Professor Michael J. Solomon, Chair
Professor Ronald G. Larson
Associate Professor Joanna M. Millunchick
Assistant Professor Jeorg Lahann

2009

# Dedication

I would like to dedicate this thesis to my grandfather, Shri Bhagwan Das Mukhija, who always wanted me to pursue higher studies

# Table of Contents

# List of Figures

# List of Tables

# Abstract

Although understanding of the phase behavior, assembly and dynamics of spherical colloids interacting through isotropic potentials is advanced, comparatively little is known about such properties of anisotropic suspensions. In this dissertation, we experimentally investigate the role of one kind of anisotropy, shape anisometry, on the assembly and dynamics of colloids. By application of the direct visualization methodology of confocal laser scanning microscopy, we discover new features of the behavior of colloidal rods with regards to their dynamics in dilute solution and their assembly under applied fields. These results are applicable to the application of anisometric particles in materials with orientational order, such as colloidal liquid crystals.

We developed a direct visualization method to characterize rotational and translational movement of colloidal rods in three dimensions. The method was applied to study the rotational and translational dynamics of dilute rod suspensions. The Brownian motion of rods in the solution was characterized by measuring the probability distributions of displacements for translation and rotation in addition to mean diffusivities. Experimental values were found to be in good agreement with theoretical predictions and errors in the method were fully characterized.

The assembly of colloidal rods was achieved by application of an applied gravitational field of variable strength in a refractive index matched solvent. The quality of the orientational ordering was quantified by direct measurement of the order parameter. Although very different effects of the applied field strength were found for rods of high and low aspect ratio, all the measurements were found to be consistent with a primary mechanism for orientational ordering based on the local volume fraction of the sediment relative to the equilibrium isotropic to nematic transition. A role of the rod glass transition in the effect of the applied field on the sediment volume fraction was also inferred from the measurements. The effect of attractive pair potential interactions due to depletion forces on the assembly of rods during sedimentation (under gravitational field) was investigated. We found that depletion interactions combined with gravitation enhanced the orientational ordering of the sediments at particular, optimum concentrations of non-adsorbing polymer.

# Chapter 1

# Introduction

## 1.1. Colloidal suspensions and forces

Colloidal science is the study of suspensions of particles that are of the order of nanometers to microns in size. Traditional industries in the field of ink, paint and ceramics depend largely on colloidal suspension for their product development [1, 2]. Application of colloidal systems in areas like personal care, food and drug delivery along with their intriguing phase behavior has long been of interest to the scientific community [2, 3]. Also, there use in producing advanced materials like photonic band-gap, microelectronics, chemical sensors and energy transfer materials has given impetus to the field [4-6].

The small size of the colloidal particles provides a significant surface area to volume ratio and therefore their interaction with each other becomes crucial in defining the final physical response of these suspensions. Typical forces present in these suspensions are hydrodynamic, diffusive, gravitational and electrostatic [7]. These forces are functions of temperature, concentration, charge, size and shape of the particles. The nature of interactions defines the physical state of the suspension, which can vary from

fully dispersed to an ordered assembly [7]. The concentration of particles also plays a significant role in defining the structure. At low concentrations and low interactions a dispersed phase is a possibility [7], however, a balance of attractive and repulsive forces at sufficiently high concentrations can lead to ordered phases, along with the entropy of the system [8, 9]. Intermediate and high concentrations with large interparticle interactions may lead to aggregated and jammed structures [10, 11].

A key feature of colloids is their interaction through the excluded volume potential [7, 12]. The excluded volume potential for hard bodies is a short-range repulsive interaction, which prohibits interpenetration of particles. The value of this potential is infinity when the particles are in contact and zero otherwise [13]. Such hard body interactions lead to disorder-order transitions at sufficiently high concentrations. Electrostatic and induced dipole moments give rise to repulsive (e.g. electrostatic) or attractive (e.g. van der Waals) forces that act on longer length scales than the excluded volume potential [7, 12]. Attractive forces favor aggregation of the particles. Large clusters of the particles are seen in the suspensions where net forces are of attractive nature. The addition of non-adsorbing polymer to colloidal suspension can induce such attractive interactions. Addition of non-adsorbing polymer promotes the overlapping of excluded volume of the colloidal particles and thereby creates an imbalance in osmotic pressure. This imbalance in the osmotic pressure gives rise to an attractive force which is known as the depletion effect. If of sufficient strength, the depletion potential can often lead to phase separation [14, 15].

### 1.2. Anisometricity

Depending upon their shape and functionality colloids can be categorized either into isotropic or anisotropic colloids. Spherical colloids with homogeneous functionality are called isotropic colloids. Spherical colloids are readily available in nature and are also easy to synthesize in the laboratory. Isotropic nature of spherical colloids makes their behavior less complicated and relatively easy to study. Researchers have developed methods to synthesize both amorphous and ordered structures of spherical colloids with great control. Also, the techniques to characterize the structure and dynamics of these suspensions are developed quite extensively in literature [16, 17]. Introducing heterogeneity to either shape or functionality of the particle can induce anisotropy [12]. Anisotropy introduced due to shape heterogeneity is known as anisometricity. Colloidal rods, dumbbells and disks are few examples of the anisometric colloids [18]. Anisometric colloids have more number of dynamic degrees of freedom than spherical colloids making their behavior more complex and interesting [19]. The added degrees of freedom change the interaction of these colloids with the surroundings as well as interparticle forces.

The single particle behavior, assembled morphology, rheology and dynamics of anisometric colloids differ significantly from spherical colloids [7, 12]. Following are few examples of dependence of these properties on the shape for rod shaped colloids. In a recent study by Champion and Mitragotri (PNAS), it's been found that rod shaped particles are difficult to phagocytosis compared to spherical particles [20]. Phagocytosis is the process in which white blood cells or macrophases engulf any external particles. The interaction between macrophage and particles is purely physical and these

experiments confirm that the interaction of a colloidal rod is different to the surroundings compared to spherical colloids.

Structural studies of colloidal rod suspensions have shown that rods can assemble into structures that are not seen for suspension of spherical colloids. Rods can make space-filling structures (i.e. gel structures) at low volume fractions, while spheres need sufficiently high volume fraction to sustain a networked structure [21]. Ellipsoid shape colloids can pack at relatively higher volume fractions than spherical colloids [19]. Also, rods can assemble into structures like liquid crystal structures that have interesting optical properties [22-24].

Not only the structure but the rheology and dynamics of the colloidal suspensions are also greatly dependent upon the shape and degree of anisometricity of the colloidal particles. For colloidal rods the anisometricity can be measured by the aspect ratio of the rod. In a study where the effect of shear on intrinsic viscosity was studied, it was found that the intrinsic viscosity varies rapidly with the aspect ratio of the colloidal rods. At a particular shear rate the intrinsic viscosity decreases with increasing aspect ratios [25]. Similarly, in another study where dynamics was investigated for colloidal rod gels, it was observed that rod-gels with higher aspect ratios showed restrained dynamics compared to smaller aspect ratios [21].

### 1.3. Single particle motion

Properties like rheological response and collective dynamics of colloidal suspensions depend significantly on single particle motion. Brownian motion study is crucial for understanding the parameters for single particle motion. Brownian motion is

the random motion of the particles suspended in a liquid or gas [7]. The molecules of the suspension media collide with the larger particles suspended into it, giving them their random movement. The force applied by these solvent molecules is responsible for the diffusion of the suspended particles. The solvent properties e.g. viscosity, temperature and shape of particle define the diffusion value of the particles. Also, there is a limit on the particle size for them to have Brownian motion, typically particles bigger than 8-10 μm in size would not get affected by the bombardment of solvent molecules.

Indirect measurement techniques like dynamic light scattering (DLS), transient electric birefringence (TEB) decay and fluorescence recovery after photobleaching (FRAP) have given us insight into rod dynamics [1, 26, 27]. However, these indirect measurement techniques provide us with mean quantities and ensemble averages; and cannot be used to identify the full distribution of particle displacements in translation and rotation. Also, these methods could associate some errors due to scattering, photo bleaching or unknown internal dynamics.

Direct visualization of colloidal rod suspensions can help us eliminate the above-mentioned limitations of indirect measurement techniques. Recently, real space measurement of anisotropic particles in two dimensions has been reported [2, 28,29]. For example, Han and co-workers [28] have studied the Brownian motion of isolated ellipsoidal particles by confining it in two dimensions, Hong and co-workers [2] have investigated the rotation around the long axis of rod-shaped colloids and Lettinga et al [29] have reported the self diffusion of rod-like viruses using fluorescent and non fluorescent microscopy. Still, there is a need to understand the dynamics of these colloids in 3 dimensions [30]. Study of the dynamics and structure of anisometric colloids will

lead to a better understanding of phase transition, liquid crystal structures, rod-gel dynamics, cell transportation and the polymer physics [2, 6, 27, 31, 32].

## 1.4. Assembly of colloidal rods

Since not only the dynamics but also the structure of these colloidal rod suspensions dictate their final properties. An understanding of the assembly and its synthesis is useful for the development of the field. In this section, we discuss the equilibrium theory that explains order-disorder transition of colloidal rod suspensions and methods involved to synthesize ordered assemblies.

### *1.4.1. Overview of Onsager's Theory*

In early 20$^{th}$ century, experimentalists [33] observed separation of colloidal rod suspensions into isotropic and anisotropic phases. This phase separation was only observed when the concentration of the particles crossed a critical concentration. This phenomenon is referred as isotropic-nematic phase transition, since in the anisotropic phase particles possess a preferred orientation. In 1949, Lars Onsager explained the reason behind this phenomenon and proposed that minimization of Helmholtz free energy of the system leads to the phase separation at higher volume fractions [9]. Since, for hard particles Helmholtz free energy is consisted of only entropic part, minimization of free energy is directly related to the entropy of the system. He separated the entropy associated to the particles into two parts, first, the entropy associated to the orientation of the particles and second, the entropy associated to mixing (associated with the orientation-dependent excluded volume of rod particle). Thus minimization of free energy is nothing but the competition between the orientation and mixing entropies. The

oreintational entropy favors disorder while mixing entropy promotes ordering. At volume fractions above critical volume fraction the contribution from the mixing entropy exceeds the contribution from orientation part. In other words, isotropic-nematic phase transition can be explained by a decrease in excluded volume to compensate the loss of orientational entropy [34]. However, Onsager conducted most of his entropic calculation of the transitional volume fractions for asymptotically long rigid rods. Self-assembly of long colloidal rods into ordered structures is well explained by Onsager's theory [35]. The theory also explains the assembly for rods having short aspect ratios with few modifications [35].

### *1.4.2. Field assisted assembly*

Self-assembly has been used effectively to produce ordered aggregates of molecules and colloidal particles. If the appropriate conditions are implemented, components of size ranging from the molecular to the macroscopic, can be self-assembled [4]. Bottom-up assembly of colloidal particles (size: nanometers to micrometers) promises new ways to synthesize photonic crystals, 3D microelectronic systems, displays, or sensors [4]. Along with these practical applications; these larger sizes also make fundamental investigations tractable. However, self-assembly can have limitations like monodispersity of the particles , assembly times, orientation and stability of the colloids [4, 36].

Field-assisted assembly of anisometric particles has received attention because fields can improve results of assembly in three ways: (i) fields can accelerate ordering by improving the kinetics of assembly; (ii) fields can potentially shift order disorder transition boundaries; (iii) if the field can generate a spatial gradient in colloidal volume

fraction, a range of locally co-existing phases can be generated in a single experiment. Few of the examples of the field assisted ordering methods for rods include spin coating, convective assembly, gravitational field and shear induced assembly. Sun and Sirringhaus (JACS, 2006) proposed a new method to produce highly aligned structures of ZnO nanorods in quick time by optimizing the combination of surface energy of the components and fluid flow direction during assembly [37]. They used spin coating effectively to produce long aligned structures of low surface energy ZnO nanorods. Similarly, use of convective assembly to fabricate 2D ordered films of tobacco mosaic virus with a high degree of long-range order is recently proposed by Wargacki et.al [38]. The quality of the ordering was controlled by controlling the parameters of the external field i.e. assembly speed. It has also been seen in the previous work that the shear field can change the nature and location of the phase transition for the suspension of the hard rods [39, 40]. In another recent study, Ripoll and coworkers have studied the facilitation provided by shear to align isotropic phase in suspension of attractive colloidal rods [41]. However, most of these methods yield in to two-dimensional assemblies and not too many methods are known to synthesize three-dimensional assemblies of colloidal rods with controlled order.

The literature suggests that there has been reasonable progress done in the area of anisometric colloids as far as their dynamics and structural studies are concerned. However, there still remains a significant gap when the full characterization of their dynamics is concerned. Development of new methods to synthesize three-dimensional assemblies with higher control is also required. This study presents new experimental

methods to a) characterize the dynamics for colloidal rod suspensions and b) produce and investigate the assemblies of colloidal rods.

### 1.5. Research Objectives:

The main objectives of this research were to characterize the dynamics and structure of colloidal rod suspensions using direct visualization. However, the study doesn't limit itself to just characterization and also explores new methods to generate colloidal rod assemblies. A model system consisting of poly(methyl methacrylate) (PMMA) spheroids was used to achieve these objectives. Following studies were conducted in this work:

1. Colloidal rods were suspended in a viscous solvent mixture that was both density and refractive index matched with the particles. Concentration of the particles in the suspension was kept in the dilute regime in order to avoid interparticle interactions. A time series of three dimensional image volumes of the suspensions were collected to capture the movement of individual colloids using confocal microscopy. Image processing and trajectory linking algorithms were used to identify and track the location and orientation of each colloidal rod in every image volume. The purpose of this experiment was to develop a method that could characterize the motion of colloidal rods in a 3D space by measuring quantities related to both translational and rotational movement.

2. Colloidal rods at dilute concentrations were suspended into a density mismatched solvent mixture. The solvent system was chosen such that it was refractive index matched with the particles. These suspensions were then subjected under various

gravitation fields to generate sediment assemblies. Final sediment structures were imaged using confocal microscopy and ordering was quantified with the help of image processing algorithms. These experiments were conducted to understand the effect of gravitation on assembly of rods of various aspect ratios.

3. In a refractive index matched solvent system that is density mismatched, attractive interactions were induced among the colloidal rods by adding a non-adsorbing polymer. These attractive colloidal rod suspensions with varying polymer concentrations were centrifuged to fabricate three-dimensional assemblies. Direct visualization and image processing algorithms were used to quantify the ordering of the sediment structures. The purpose of this set of experiments was to understand the effect of depletion during the assembly of colloidal rods under sedimentation.

## 1.6. Outline of the Dissertation

In this dissertation, we describe the direct visualization studies that are conducted in order to understand the three-dimensional dynamics and structure of colloidal rod suspensions. In chapter 2, movement of individual colloidal rods is characterized by measuring their translational and rotational diffusivities for dilute suspensions. We also probe the distributions of displacements in both translation and rotation along with the mean quantities. In chapter 3, the sediment structures of colloidal rods that are made by applying various strengths of gravitational field to dilute rod suspensions are investigated. These structures are characterized as isotropic or nematic liquid crystal phase based upon the order parameter and the contact number calculations along with the visual images. Effect of depletion on the assemblies that are synthesized under gravitational field is

studied in chapter 4. In chapter 5, we conclude the dissertation by discussing the conclusions and future work.

## References


1. R. Cush; D. Dorman; P. S. Russo, *Macromolecules* **2004,** 37, (25), 9577-9584.
2. L. Hong; S. M. Anthony; S. Granick, *Langmuir* **2006,** 22, (17), 7128-7131.
3. A. D. Dinsmore; M. F. Hsu; M. G. Nikolaides; M. Marquez; A. R. Bausch; D. A. Weitz, *Science* **2002,** 298, (5595), 1006-1009.
4. G. M. Whitesides; M. Boncheva, *Proceedings of the National Academy of Sciences of the United States of America* **2002,** 99, (8), 4769-4774.
5. M. A. Horsch; Z. Zhang; S. C. Glotzer, *Nano Letters* **2006,** 6, 2406-2413.
6. C. M. van Kats; P. M. Johnson; J. van den Meerakker; A. van Blaaderen, *Langmuir* **2004,** 20, (25), 11201-11207.
7. S. D. A. Russel W.B., Schowalter W.R., *Cambridge Univ. Press, Cambridge* **1989**.
8. A. P. Hynninen; M. E. Leunissen; A. van Blaaderen; M. Dijkstra, *Physical Review Letters* **2006,** 96, (1), 4.
9. L. Onsager, *Annals of the New York Academy of Sciences* **1949,** 51, (4), 627-659.
10. E. Sanz; M. E. Leunissen; A. Fortini; A. van Blaaderen; M. Dijkstra, *Journal of Physical Chemistry B* **2008,** 112, (35), 10861-10872.
11. J. M. Valverde; M. A. S. Quintanilla; A. Castellanos, *Physical Review Letters* **2004,** 92, (25).
12. R.G. Larson, The Structure and Rheology of Complex Fluids, *Oxford University Press, Oxford* **1999**.
13. K. V. Tretiakov; K. W. Wojciechowski, *Physica Status Solidi B-Basic Solid State Physics* **2005,** 242, (3), 730-741.
14. S. Asakura; F. Oosawa, *Journal of Chemical Physics* **1954,** 22, (7), 1255-1256.
15. S. Asakura; F. Oosawa, *Journal of Polymer Science* **1958,** 33, (126), 183-192.
16. C. J. Dibble; M. Kogan; M. J. Solomon, *Physical Review E* **2006,** 74, 041403.
17. T. Solomon; M. J. Solomon, *Journal of Chemical Physics* **2006,** 124, (13), 134905.
18. S. C. Glotzer; M. J. Solomon, *Nature Materials* **2007,** 6, 557-562.
19. A. Donev; I. Cisse; D. Sachs; E. Variano; F. H. Stillinger; R. Connelly; S. Torquato; P. M. Chaikin, *Science* **2004,** 303, (5660), 990-993.
20. J. A. Champion; S. Mitragotri, *Proceedings of the National Academy of Sciences of the United States of America* **2006,** 103, (13), 4930-4934.
21. A. Mohraz; M. J. Solomon, *Journal of Colloid and Interface Science* **2006,** 300, (1), 155-162.
22. M. P. B. vanBruggen; F. M. vanderKooij; H. N. W. Lekkerkerker in: *Liquid crystal phase transitions in dispersions of rod-like colloidal particles*, 3rd Liquid Matter Conference, Norwich, England, Jul 06-10, 1996; Iop Publishing Ltd: Norwich, England, 1996; pp 9451-9456.
23. E. Belamie; P. Davidson; M. M. Giraud-Guille, *Journal of Physical Chemistry B* **2004,** 108, (39), 14991-15000.
24. M. Adams; Z. Dogic; S. L. Keller; S. Fraden, *Nature* **1998,** 393, (6683), 349-352.

25. Karilla. S. Kim S., Microhydrodynamics: principles and selected applications *Butterworth-Heinemann, Boston* **1991**.
26. M. P. B. van Bruggen; H. N. W. Lekkerkerker; G. Maret; J. K. G. Dhont, *Physical Review E* **1998,** 58, (6), 7668-7677.
27. J. K. Phalakornkul; A. P. Gast; R. Pecora, *Journal of Chemical Physics* **2000,** 112, (14), 6487-6494.
28. Y. Han; A. M. Alsayed; M. Nobili; J. Zhang; T. C. Lubensky; A. G. Yodh, *Science* **2006,** 314, (5799), 626-630.
29. M. P. Lettinga; E. Barry; Z. Dogic, *Europhysics Letters* **2005,** 71, (4), 692-698.
30. S. Sacanna; L. Rossi; B. W. M. Kuipers; A. P. Philipse, *Langmuir* **2006,** 22, (4), 1822-1827.
31. G. H. Koenderink; D. Aarts; A. P. Philipse, *Journal of Chemical Physics* **2003,** 119, (8), 4490-4499.
32. P. D. Cobb; J. E. Butler, *Journal of Chemical Physics* **2005,** 123, (5), 054908.
33. H. Zocher, *Zeitschrift Fur Anorganische Und Allgemeine Chemie* **1925,** 147, (1/3), 91-U15.
34. H. N. W. Lekkerkerker; P. Coulon; R. Vanderhaegen; R. Deblieck, *Journal of Chemical Physics* **1984,** 80, (7), 3427-3433.
35. B. Tjiptomargo; G. T. Evans, *Journal of Chemical Physics* **1990,** 93, (6), 4254-4265.
36. M. P. B. van Bruggen; H. N. W. Lekkerkerker, *Macromolecules* **2000,** 33, (15), 5532-5535.
37. B. Q. Sun; H. Sirringhaus, *Journal of the American Chemical Society* **2006,** 128, (50), 16231-16237.
38. S. P. Wargacki; B. Pate; R. A. Vaia, *Langmuir* **2008,** 24, (10), 5439-5444.
39. W. Hess; K. Schonert, *Chemical Engineer-London* **1976**, (306), 103-103.
40. T. A. J. Lenstra; Z. Dogic; J. K. G. Dhont, *Journal of Chemical Physics* **2001,** 114, (22), 10151-10162.
41. M. Ripoll; P. Holmqvist; R. G. Winkler; G. Gompper; J. K. G. Dhont; M. P. Lettinga, *Phys Rev Lett* **2008,** 101, (16), 168302.

# Chapter 2

# Translational and Rotational Dynamics of Colloidal Rods by Direct Visualization with Confocal Microscopy


## Chapter Summary

We report an experimental method to characterize the dynamics of colloidal rods by measuring their rotation and translation in three dimensions with confocal microscopy. The method relies on solvent viscosification to retard dynamics to time scales that are compatible with 3D confocal optical microscopy. Because the method yields a full three dimensional characterization of rod displacement and orientation, it is applicable to situations in which complex, anisotropic dynamics emerge. Examples include behavior in liquid crystal phases with both orientational and positional order, suspensions subjected to applied fields such as shear flow or sedimentation, and the emerging area of anisotropic particle dynamics. We demonstrate the performance of the method by quantifying the Brownian motion of fluorescent poly (methyl methacrylate) rods (aspect ratio, L/D = 3.1 and 7.0) grafted with poly (dimethylsiloxane) stabilizer. The rods are dispersed at dilute concentration in a solvent mixture of viscosity 2.0 Pa.s. Rod translational and rotational diffusivities are extracted from the measured translational mean square displacement of the centroid positions and of the rod unit vector $\boldsymbol{u}$,

respectively. Rod orientational dynamics are characterized relative to both their azimuthal and polar angles. Probability distributions for the translation and rotation in the frame of rod are computed from the measurements. Experimental values obtained agree well with theory available for the dynamics of isolated rods.

## 2.1. Introduction

The synthesis, characterization and assembly of anisotropic particles are of interest due to potential applications in areas such as microelectronics, photonic band-gap and energy transfer materials [1-3]. Paints, ceramics, ink and pharmaceutics industries also use anisometric particles for product formulation [4, 5]. In addition, the structure, dynamics and rheology of anisometric colloidal suspensions all differ significantly from systems composed of spherical particles. For example, suspensions of colloidal rods show unusual aggregate, gel, packing and equilibrium phase behavior [6-10]. Recently, improved methods to synthesize monodisperse colloidal rod suspensions have opened up new possibilities for fundamental studies of anisotropic particle structure, phase behavior and dynamics [2, 10-12]. Because of its role in mediating both the development of structure and the rheological response, the Brownian motion of anisometric rod suspensions is of special interest. Tools such as dynamic light scattering, fluorescence recovery after photobleaching and transient electric birefringence decay have contributed to our understanding of rod dynamics [4, 13, 14].

Liquid crystal phases with both translational and orientational order, colloidal glasses and gels, and suspensions subjected to applied flow and electric fields may yield complex, anisotropic dynamics. In these cases, fully three-dimensional characterization of mean colloidal translational and orientational dynamics would be a powerful tool to

study the fundamental fluid physics of these processes. Access to the full distribution of particle displacements and rotation would also be beneficial. Very recent publications of new particle tracking methods for quantifying translation and rotation of anisometric particles [5, 15-17] have brought the field closer to achieving these two aims.

Time-resolved direct visualization of colloidal rod dynamics in three dimensions with confocal microscopy could possibly accomplish these two aims in a single experiment. This method has been a powerful tool to study analogous phenomena in spherical colloidal suspensions [18-20]. Rod tracking in two-dimensions has also been studied [16, 17]. Methods such as these, if developed for three dimensions, would be powerful because they could be applied for simultaneous tracking of multiple particles, thereby improving signal to noise ratio [15, 18].

Here we assess the scope to apply time-resolved confocal microscopy to characterize the translational and orientational dynamics of colloidal rods with three-dimensional resolution. We use a laser scanning confocal microscope to acquire image volumes with the high spatial resolution needed to resolve orientational dynamics. We address the slow-scan speed of laser scanning instruments through the strategy of solvent viscosification that is reminiscent of the scheme developed by Boger for dilute polymer solutions [21]. To establish the potential future utility of this method to the emerging area of complex, anisotropic dynamics [22], we emphasize identification of resolution limits, quantification of measurement errors and comparison to theory in this chapter.

## 2.2. Materials

Our model system is a dilute suspension of colloidal rods dispersed in a viscous solvent that is density and refractive index matched with the rods. The density matching minimizes sedimentation. Refractive index matching improves confocal microscopy image quality in addition to promoting rod stability by minimizing attractive van der Waals interactions between rods. Fluorescent poly(methyl methacrylate)-g-poly(dimethylsiloxane) rods were synthesized as in Mohraz and Solomon [10][9] and Keville et al [23]. Briefly, colloidal spheres were subjected to uniaxial extension above their softening temperature to transform particle shape into a spheroid. The fluorescent PMMA-g-PDMS colloidal spheres (diameter = 1.0 ± 0.04 μm, Dye: Nile Red) were synthesized using dispersion polymerization. These colloidal spheres were then suspended in a polymerizable liquid (silanol-terminated PDMS) and an elastic matrix was formed by polymerization and cross-linking with methylhydro-dimethyl siloxane. This elastic matrix was heated above the glass transition, $T_g$ ($T_{heating}$ =195°C) of the colloidal particles and subjected to uniaxial extension. The material was then cooled to a temperature below the $T_{g,}$ thereby fixing the spheroidal shape of the particles. Finally, the spheroids were harvested from the elastic film by chemical degradation (degradation mixture: 0.15 g sodium methoxide in 75 g isopropyl alcohol) of the matrix. These colloids were washed by centrifugation and transferred to the test solvent. Spheroids of aspect ratio 3.1 ± 0.2 (major and minor axes of 2.15 (±0.11) and 0.71 (±0.03) μm, respectively) and 7.0 ± 0.6 (major and minor axes of 3.65 (±0.13) and 0.52 (±0.03) μm, respectively) were synthesized by applying different extensions to the films. Scanning electron microscopy (SEM) was used to characterize the dimensions and shape of the

model materials. Based on these images, we approximate the particle shape as prolate spheroid for purposes of comparison to the available theory.

The test solvent is a ternary mixture of cyclohexyl bromide (CXB), decalin and polydimethylsiloxane (PDMS). Cyclohexyl bromide (CXB) and decalin were mixed in a ratio of 68 / 32 to match the refractive index and density of the solvent and particles. Sterically stabilized PMMA spheres dispersed in organic solvents like those here are charged[24, 25]. The rods synthesized here are thus likely charged as well. Polydimethylsiloxane of approximate viscosity 10.0 Pa.s (MW = 62,700 g/mol, $R_{g,\ theta}$ ~ 5 nm) was mixed with a mixture of CXB/decalin in a ratio of 2 to 1 to obtain a final solvent viscosity of 2.0 ± 0.03 Pa.s as measured by cone and plate rheometer (AR1000, TA Instruments). At this high viscosity Brownian motion is damped such that characteristic rod displacements between each time step are ~ 25% of the rod minor axis dimension (for example, the orientationally averaged translational diffusivity ($D_0$) for a rod of aspect ratio (L/D) = 3.1 (L = 2.15 μm and D =0.71 μm) is $2.0\times10^{-4}$ $\mu m^2/s$ at this viscosity. For a typical delay time between image volumes ~ 60 s, rod displacement ~ $((2D_0t)^{1/2}$ ~ 155 nm.). The stability of the rods in this solvent mixture suggests that depletion interactions are not appreciable. This observation is consistent with the fact that the polymer concentration is much greater than the overlap threshold; $c/c^* > 10$.

### *2.2.1. Direct visualization of rod dynamics*

Experiments were conducted at a temperature of 23°C at a typical volume fraction of ~ 0.25%. At this volume fraction the rod number density, ρ is about an order of magnitude less than the threshold ~ $1/L^3$ at which semi-dilute and anisotropic excluded volume effects become appreciable [26]. Thus, comparison of results to theoretical

expressions available for free rod diffusion is warranted. Measurements were conducted in a custom-made sample cell. The cell was constructed by mounting cylindrical glass vials of I.D. 4 mm and height 1.5 cm on a glass cover-slip (to facilitate imaging from the bottom). Once the samples were prepared, the vials were sealed with another cover-slip to avoid any evaporation. The samples were allowed to equilibrate for ~3 hours before imaging.

To capture particle motion in all four dimensions (x, y, z, t), stacks of 120-130 2-D images (in a plane parallel to the coverslip) were acquired at fixed time intervals $\Delta t$ = 50-60s using confocal laser scanning microscopy (CLSM). The instrument is a Leica TCS SP2 confocal microscope operating with a 100× oil immersion objective (numerical aperture 1.4) and image acquisition time of 0.336 s/frame. 20 to 30 image volumes of approximate dimension $42 \times 11 \times 11\ \mu m^3$ were collected with the cubic voxel dimension of 0.0814 μm. At the test number density, the dynamics of ~ 10 rods were tracked. Image volumes were collected approximately 15 to 20 microns above the cover-slip to minimize the magnitude of wall hydrodynamic interactions.

The image volume series was then processed using particle finding and trajectory linking algorithms to obtain translational and rotational diffusivities. These algorithms are an extension of the algorithm described by Crocker and Grier [27], Mohraz and Solomon [10], and Dibble and co-workers [18] to identify anisotropic centroid location and track centroid dynamics. Here, we extend the approach to track both translational and rotational dynamics of rods. After Gaussian filtering, we apply an anisotropic local brightness criterion to identify the backbone (major axis) of the colloidal rod. Centroid location and orientation of spheroids are computed by computing moments of the

backbone configuration [10]. After a (small) time-independent, uniform translation of the image volume coordinates is implemented to compensate for instrument drift ($\Delta v \sim 100$ nm/min), displacements of the centroid locations of individual particles are tracked and compared from one frame to yield trajectory linking. Trajectories are linked if they satisfy the following condition: A rod in the $j^{th}$ time frame is linked to a rod from the $(j-1)^{th}$ time frame if the change in centroid location is less than its smallest dimension (D/2) [27].

Note that our image processing algorithm locates rod orientation uniquely only on a hemisphere ($0 < \theta < \pi$ and $0 < \phi < \pi$) of the unit sphere whereas, for theory, the usual definition of a unit vector parallel to the major axis $\boldsymbol{u}(t)$ is defined on the full unit sphere. The difference is due to the fact that the two tips of the rod are not optically distinguishable by CLSM. This discrepancy would preclude a simple comparison of our experiments to theory if the probability of a large excursion of $\boldsymbol{u}(t)$ over the surface of the unit sphere were significant [15]. However, because of slow dynamics in our viscous system, these large excursions are rare. By requiring for each rod $[\boldsymbol{u}(j+1)-\boldsymbol{u}(j)]^2 < 2$ between any two sequential frames we uniquely track just one of the two rod ends for the duration of an experiment. Because Eq. 10 is Gaussian and $D_r(t_{j+1} - t_j) << 1$ for our experiments the potential for tip mis-identification due to the condition $[\boldsymbol{u}(j+1)-\boldsymbol{u}(j)]^2 < 2$ is very small.

Figure 2.1 reports real space imaging and particle identification and tracking results for a representative experiment. The images are two-dimensional projections (in a plane parallel to the coverslip) of image volumes collected at three different times (t = 0, 510, 1020 s). Corresponding linked-sphere Rasmol reconstructions of the results of

image processing and particle tracking are shown. The consistent color-coding between the frames identifies individual rod trajectories. Figure 2.1 allows a qualitative assessment of the fidelity of rod image processing and trajectory linking. To quantify this error, we applied the particle tracking and linking algorithm to a specimen of immobilized rods as suggested by Savin and Doyle [28]. The immobilization was accomplished by cross-linking a rod suspension in PDMS. The specimen was then imaged under the same conditions as the other experiments. As per [28], these static error estimates were applied to the translational and rotational diffusion measurements in the next sections. Briefly, we find that static errors for centroid diffusion, parallel to the rod unit vector are, $<\varepsilon_{\parallel}^2> = 0.003\ \mu m^2$, perpendicular to the rod unit vector are, $<\varepsilon_{\perp}^2> = 0.002\ \mu m^2$ and error in the unit vector rotation are, $<\varepsilon_{\boldsymbol{u}}^2> = 0.06\ (rad)^2$.

### 2.3. Quantification of rod dynamics

Image processing and trajectory linking algorithms yield the centroid location and polar, $\theta$ and azimuthal orientation angle, $\phi$ for each individual colloidal rod in the laboratory (CLSM) frame at each time step (The polar angle, $\theta$, is defined relative to an axis perpendicular to the CLSM coverslip on the interval $0 < \theta < \pi$; The azimuthal angle, $\phi$, is defined relative to the axis of the CLSM line scanner on the interval $0 < \phi < \pi$). However, for dilute solutions, dynamical quantities of interest are best reported in the frame of the particle, relative to its unit vector (e.g. Figure 2.2). After that transformation, we compute the following: (i) mean squared centroid displacement parallel ($<(\Delta x_{\parallel}(t))^2>$) and perpendicular ($<(\Delta x_{\perp}(t))^2>$) to the rod unit vector; (ii) mean squared displacements of

rod unit vector ($<(\Delta \boldsymbol{u}(t))^2>$); (iii) probability distribution function of the parallel translation ($P(\Delta x_{\|})$, perpendicular translation ($P(\Delta x_{\perp})$) and unit vector ($P(|\Delta \boldsymbol{u}|)$). The first two data sets yield estimates of translational and rotational diffusivities that can be compared to theory. The third quantity can be used to assess any non-Gaussian effects on translation and orientation. In each case we assess aggregate errors of measurement, image processing and particle tracking by plotting mean data and standard error of the mean assessed from specimen replication and multiple particle tracking. Standard errors of the mean are based on measurement for ~ 23 rods for the aspect ratio 3.1 and ~ 7 rods for the aspect ratio 7.0.

### *2.3.1. Laboratory frame characterization*

Quantification of rod Brownian motion is plotted in Figure 2.3. Figure 2.3 a plots both the change in orientation and displacement of a rod during a representative experiment (20 time frames with $\Delta t = 51$ s). The figure shows that a rod undergoes significant displacement and rotation during an experiment: summed displacement is ~ 3 μm and rotation is ~ 175° in θ and 190° in ϕ measured along the contour of the trajectory. Figure 2.3 b shows the rod mean-squared displacement projected along each of the three-laboratory frame coordinate dimensions. The coincidence of the three measurements indicates that potential bias due to specimen drift, point spread function and sedimentation is not greater than random measurement error. Also, the power law slope of the three-dimensional mean-squared displacement (the sum of each of the measurement in the three coordinate directions) agrees well with the expectation for free particles ($<(\Delta r(t))^2> \sim t^{0.95\pm0.01}$). The multiple particle tracking method also resolves

rotational dynamics. Figures 2.4 a and b show the probability distributions of the azimuthal angle, $\phi$, and polar angle, $\theta$, respectively. Phenomenologically, we find that these distributions are approximated by a Gaussian function [4].

### *2.3.2. Measurement of parallel and perpendicular translational diffusion*

Trajectory linking and image processing yields rod centroid position (x,y,z) as well as the polar and azimuthal angle ($\theta$, $\phi$) of the rod orientation. We transformed between Cartesian and spherical coordinates to compute translation and rotation of the rod unit vector. Briefly, if the laboratory frame displacement vector of the $i^{th}$ rod between frames j-1 and j is $\partial \mathbf{r}_{ij} = \partial r_{x,ij}\mathbf{e}_x + \partial r_{y,ij}\mathbf{e}_y + \partial r_{z,ij}\mathbf{e}_z$, then the transformation matrix to the rod frame displacement vector $\partial \mathbf{x}_{ij} = \partial x_{r,ij}\mathbf{e}_r + \partial x_{\theta,ij}\mathbf{e}_\theta + \partial x_{\phi,ij}\mathbf{e}_\phi$ is as per Eq. 1 [29]. Here $\boldsymbol{e}_r$, $\boldsymbol{e}_\theta$ and $\boldsymbol{e}_\phi$ are the spherical coordinate unit vectors shown in Figure 2.2 defined relative to the polar and azimuthal angles ($\theta_{ij}$, $\phi_{ij}$). (These angles are taken as the average of the orientation in frames j and j-1.)

$$\begin{bmatrix} \partial x_{r,ij} \\ \partial x_{\theta,ij} \\ \partial x_{\phi,ij} \end{bmatrix} = \begin{vmatrix} \sin\theta_{ij}\cos\phi_{ij} & \sin\theta_{ij}\sin\phi_{ij} & \cos\theta_{ij} \\ \cos\theta_{ij}\cos\phi_{ij} & \cos\theta_{ij}\sin\phi_{ij} & -\sin\theta_{ij} \\ -\sin\phi_{ij} & \cos\phi_{ij} & 0 \end{vmatrix} \begin{bmatrix} \partial r_{x,ij} \\ \partial r_{y,ij} \\ \partial r_{z,ij} \end{bmatrix} \qquad (1)$$

From the definitions of Figure 2.2, $\partial x_{\parallel,ij} = \partial x_{r,ij}$ and $\partial x_{\perp,ij} = \left(\partial x_{\theta,ij}^2 + \partial x_{\phi,ij}^2\right)^{1/2}$, where the parallel and perpendicular directions are defined relative to the rod unit vector. By averaging over all times and particles we obtain expressions for the rod parallel and perpendicular mean squared displacement. In the long time limit these mean squared displacements are related to the components of the rod translational diffusivity [26][26]:

$$<[(x_{r,i}(t)-x_{r,i}(0)]^2>=2D_t^{\|}t \tag{2}$$

$$<[x_{\theta,i}(t)-x_{\theta,i}(0)]^2>+<[x_{\phi,i}(t)-x_{\phi,i}(0)]^2> \;=\; 4D_t^{\perp}t \tag{3}$$

Theoretical values of these translational diffusivities are available from Brenner H (1974) [30].

$$D_t^{\|} = k_BT/\eta_S \hat{K}_t^{\|} \quad \text{and} \quad D_t^{\perp} = k_BT/\eta_S \hat{K}_t^{\perp} \tag{4}$$

Here, $\hat{K}_t^{\|}$ and $\hat{K}_t^{\perp}$ are material constants (available in ref. [30]), which depend upon the shape and size of the particle. Comparison of the measurements to Eq. 4 is justified in the case where the effects of wall hydrodynamic interactions and particle charge are minimal. For the conditions of our experiments, the distance of any point in the image volume to a sample boundary is always as least 18 times greater than the half-length of the 3.1 aspect ratio rod, and at least 12 times greater than for the aspect ratio 7.0 rods. From these values we estimate from Happel and Brenner [31] that deviations in friction coefficients in the parallel and perpendicular directions will vary, in the worst case, from 5% to 26% depending on aspect ratio and orientation. Deviations due to charge are difficult to quantitatively estimate for non-spherical particles. As a point of reference, a recent study for charged disks of aspect ratio 5-10 suggests no effect of charge for Debye layers that are asymptotically thick or thin relative to the largest dimension of the particle [32]. However, deviations in the dilute friction coefficient that depend on aspect ratio and degree of charge are found for Debye layers of intermediate thickness due to the interplay between hydrodynamic dissipation and electrolyte diffusion. However, these effects tend to be less than the overall effect of particle shape on friction coefficient [32].

In Figures 2.5 a and b we plot the experimental and corresponding (Eq. 4) theoretical values of parallel and perpendicular translational mean square displacements for the rods of the two aspect ratios studied (3.1 and 7.0). The parallel and perpendicular diffusion coefficients can be obtained using the Eq. 2 and 3, once the respective mean square displacements are calculated. These diffusion coefficients are reported in the Table 2.1. The linearity of the measured mean squared displacement is excellent and the relative error between the theory and experiments is small (mean relative error for the four quantities ~ 15%).

### *2.3.3. Measurement of rotational diffusion*

Stochastic motion of the unit vector ***u(t)***, oriented in the direction parallel to the rod major axis, defines the rotational Brownian motion of the rod [26][26]:

$$\boldsymbol{u}(t) = \cos\phi \sin\theta\, \boldsymbol{e}_x + \sin\phi \sin\theta\, \boldsymbol{e}_y + \cos\theta\, \boldsymbol{e}_z \tag{5}$$

Because the dynamics of ***u(t)*** has been well studied theoretically [26, 33], we choose to quantify orientational dynamics with this quantity rather than the measured polar and azimuthal angles. In particular, we quantify rotational diffusion by computing the unit vector's mean-square displacement $<(\boldsymbol{u}(t)-\boldsymbol{u}(0))^2>$**.** For a free rod, we expect [26]:

$$< [\boldsymbol{u}(t) - \boldsymbol{u}(0)]^2 >= 2(1 - \exp(-2D_r t)) \tag{6}$$

For a free rod (prolate spheroid), the rotational diffusivity depends on aspect ratio [26]:

$$D_r = \frac{3k_B T(\ln(2r) - 0.5)}{\pi \eta_s L^3} \tag{7}$$

Here, $k_B$ is the Boltzmann's constant, T is the temperature, r =L/D, (L and D are the major and minor axis of the rod respectively) and $\eta_s$ is the solvent viscosity.

In Figure 2.6, we plot $\langle[\boldsymbol{u}(t)-\boldsymbol{u}(0)]^2\rangle$ for the two aspect ratio rods studied. The corresponding theoretical prediction based on the rod's aspect ratio is shown. Best estimates of the rotational diffusivity are reported in Table 2.1. The relative error is 7% for r = 3.1 and 13% for r = 7.0.

### *2.3.4. Probability distribution functions of displacement and rotation for Brownian motion of a free rod*

While a number of other methods (e.g. light scattering) can be used to characterize the mean translation and rotation of anisotropic particles we have reported to this point, the particle-tracking confocal microscopy approach also yields the full distribution of displacements and rotations. To our knowledge, these distributions have not been reported, even for isolated rods in three dimensional bulk solutions. Characterization of their behavior and errors is thus a useful reference data set upon which to base future studies of three-dimensional motion of anisotropic particles in complex phases and geometries.

The quantity of interest is the probability of a displacement $\Delta x_i$ along a particular coordinate axis in a time interval t. This probability distribution function is a strong function of the diffusion coefficient in that direction [34]. Choosing to work in the frame of the rod unit vector, we can identify a probability distribution function of the centroid in directions parallel and perpendicular to the rod unit vector. At long times, these functions are Gaussian [33]:

$$f(\Delta x_{\|},\, t) = \left(4\pi D_{\|} t\right)^{-\frac{1}{2}} \exp\left(-\frac{\Delta x_{\|}^{\,2}}{4D_{\|} t}\right) \tag{8}$$

$$f(\Delta x_{\perp},\, t) = \left(4\pi D_{\perp} t\right)^{-\frac{1}{2}} \exp\left(-\frac{\Delta x_{\perp}^{\,2}}{4D_{\perp} t}\right) \tag{9}$$

Because the argument of the exponential is non-dimensional, it is a useful scale to compare measurements across times and aspect ratios. Thus, in Figures 2.7 a and b, we plot probability distribution functions measured at a range of times for the two aspect ratios scaled per Eq. 8 and 9. The measured probability distribution functions in the figure are normalized by the prefactor that multiplies the exponential to facilitate the comparison (In this way, the intercept is unity). We see that the shape and scaling of the data are well modeled by the Gaussian functional form for values of the argument of the exponential up to about 3.5. Agreement between theory and experiment progressively deteriorates beyond this point. Noise increases as well. The data quality for translation parallel to the unit vector is slightly better than for perpendicular translation, likely because rod mobility is greater in the parallel direction.

We propose a similar analysis for the probability distribution function of rotations. For short times ($D_r t << 1$), the unit vector displacements are equivalent to a random walk on a (flat) 2D surface [26]. Thus, in this limit, we anticipate:

$$f(|\Delta \boldsymbol{u}|,\, t) = \left(4\pi D_r t\right)^{-1} \exp\left(-\frac{\Delta \boldsymbol{u}^2}{4D_r t}\right) \tag{10}$$

Where $|\Delta \boldsymbol{u}|$ is the magnitude of the unit vector displacement on the unit sphere over a time interval t. In Figure 2.8 we plot measurements for different times and aspect ratios. The figure shows that for $D_r t << 1$, the distribution follows the functional form of

Eq. 10 for $\frac{\Delta u^2}{4D_r t} < \sim 3$. However, we note that relative to the figure 2.7 (translational distributions) random error is greater for the orientation distribution of figure 2.8. The underlying origin of the large error bars in figure 2.8 is the significant static error in determination of the unit vector. That is error in the unit vector ~$1/P_a$, where $P_a$ is the half-length of a rod in pixels. For our measurement $P_a$ is ~ 16 for our smallest aspect ratio rod. Increasing this value would lead to improved resolution in $\boldsymbol{u}(t)$. Indeed, the particular $P_a$ value implicitly sets a lower limit of aspect ratio for which orientational dynamics could be tracked by our method. This discussion shows that errors in orientational dynamics (e.g. Figs 6 and 8) depend in a complex way on particle shape, image resolution, static error and image acquisition time. Comparison of this study and refs [5, 15, 16] shows that angular errors are in the range ~ 1-15°.

## 2.4. Discussion

Recent chapters have reported new experimental methods and results characterizing the Brownian motion of isolated anisotropic particles. Here we assess the relationship between the present study and these reports.

Han et al. [16] observed the coupling between rotational and translational diffusion in colloidal rods restricted to two dimensions. The confinement in two dimensions both simplified the imaging and exploited the fact that friction anisotropy is greater in 2D than in 3D. The work demonstrates that, in the laboratory frame, translational diffusion crosses over from anisotropic to isotropic displacement due to the randomizing of orientation that occurs due to rotational diffusion. We note that even

though the duration of our experiments is less than a characteristic time for orientational decorrelation, our measured laboratory frame mean-squared displacements in 3D (figure 2.3 b) are fully isotropic because data are averaged over many different particles, each with an initial orientation that is uniformly distributed. The crossover from anisotropic to isotropic diffusion can have implications for both the phase behavior and rheology of anisotropic colloids and our particle tracking method could be applied to study this relationship in 3D.

Hong et al. [5] applied particle tracking methods to optically anisotropic, connected spheres to characterize the probability distribution function of rotations both in plane and around the long axis of the particles. Our confocal microscopy method extends the quantification of in plane rotations of the long axis of the rod into three dimensions. This extension allows the full orientational dynamics of the rod unit vector to be characterized, as per figure 2.6 and 2.8.

Anthony et al. [15] reported a method to monitor the time dependence of two translational and two orientational degrees of freedom in optically anisotropic spheres. The method was applied to measure mean rotational and translational diffusion. Our approach is complementary: by means of solvent viscosification, we retard dynamics so that all five degrees of freedom are tracked. For rods, this full field tracking allows quantification of both the parallel and perpendicular components of the rod translational diffusivity and probability distribution functions.

Our work and the three other particle tracking studies discussed above demonstrate that experimental tools now exist to quantify every degree of freedom of the complex Brownian motion of anisotropic nanocolloids. By demonstrating the application

of the 3D particle tracking method to quantify the Brownian motion of isolated rods, and by assessing errors in both diffusivities and probability distributions, this chapter can further the application of these methods to the cases of complex anisotropic shape, applied fields and non-dilute concentrations.

## 2.5. Conclusion

In this work, we report a particle tracking confocal microscopy method to characterize the translational and orientational dynamics of rods in three dimensions by retarding dynamics into a resolvable range through solvent viscosification. We apply our method to suspensions of colloidal rods (r= 3.1 and 7.0) undergoing Brownian motion and find that measured rotational and translational diffusion coefficients agree well with theory valid for infinite dilution. (For both the aspect ratios the discrepancy between measurements and theory is ~ 15%). Because both the image processing method that resolves the rod backbones [9] and the particle linking algorithms [18] have been successfully applied at high concentrations, the method could immediately be applied to study semi-dilute and concentrated systems -- including systems with orientational order due to phase transitions or applied fields. In addition, the ability of the method to simultaneously resolve three spatial and two orientational dimensions suggests potential applications to study the dynamics of complex particles that combine anisotropy in shape and potential interactions [22].

**Table 2-1:** Comparison between theoretical and experimental values of translational and rotational diffusion coefficients (aspect ratio 3.1 and 7.0).

| D | Experimental Value | Theoretical Value |
|---|---|---|
| $D_t^{\parallel}$ (r =3.1) | $2.57 \pm 0.31 \times 10^{-4}$ μm$^2$/s | $2.27 \times 10^{-4}$ μm$^2$/s |
| $D_t^{\perp}$ (r=3.1) | $1.94 \pm 0.05 \times 10^{-4}$ μm$^2$/s | $1.83 \times 10^{-4}$ μm$^2$/s |
| $D_r$ *(r=3.1)* | $2.41 \pm 0.35 \times 10^{-4}$ (rad)$^2$/s | $2.58 \times 10^{-4}$ (rad)$^2$/s |
| $D_t^{\parallel}$ (r=7) | $2.01 \pm 0.03 \times 10^{-4}$ μm$^2$/s | $2.03 \times 10^{-4}$ μm$^2$/s |
| $D_t^{\perp}$ (r =7) | $1.26 \pm 0.04 \times 10^{-4}$ μm$^2$/s | $1.47 \times 10^{-4}$ μm$^2$/s |
| $D_r$ (r =7) | $7.79 \pm 0.26 \times 10^{-5}$ (rad)$^2$/s | $8.95 \times 10^{-5}$ (rad)$^2$/s |

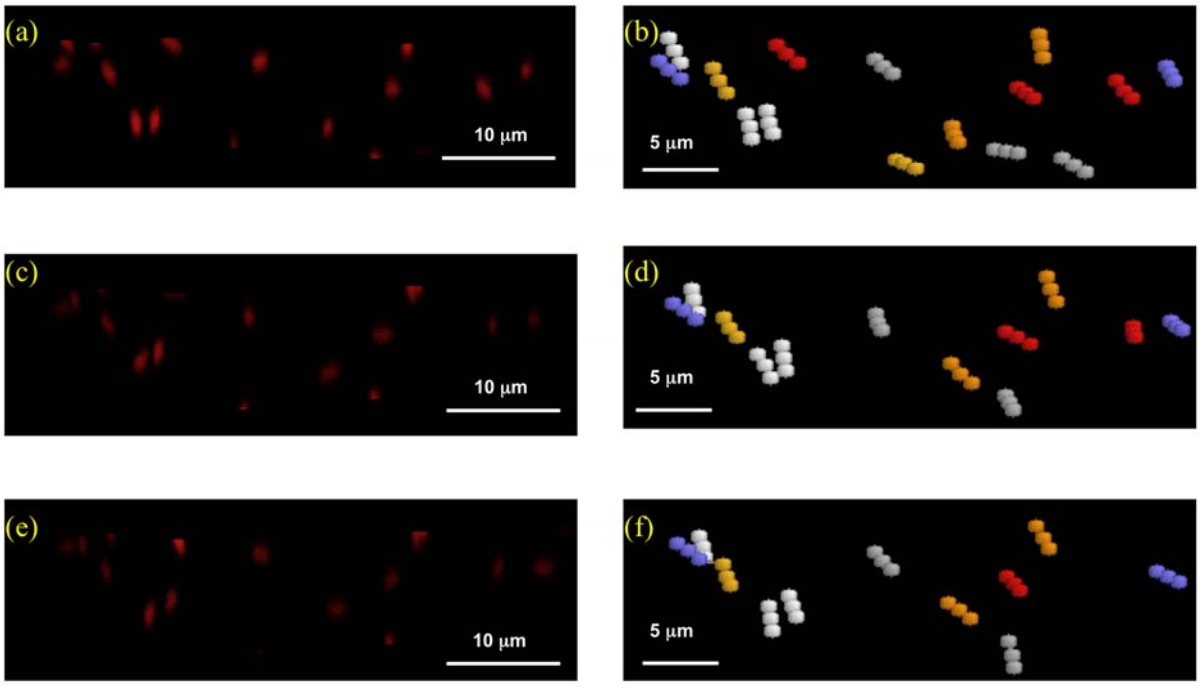


**Figure 2-1:** 2D projections of three 3D (XYZ) volumes (t = 0, 510, 1020 s) of CLSM images of colloidal rods suspended in solvent mixture (a, c, e) and their linked-sphere Rasmol reconstructions (b, d, f) (aspect ratio 3.1).

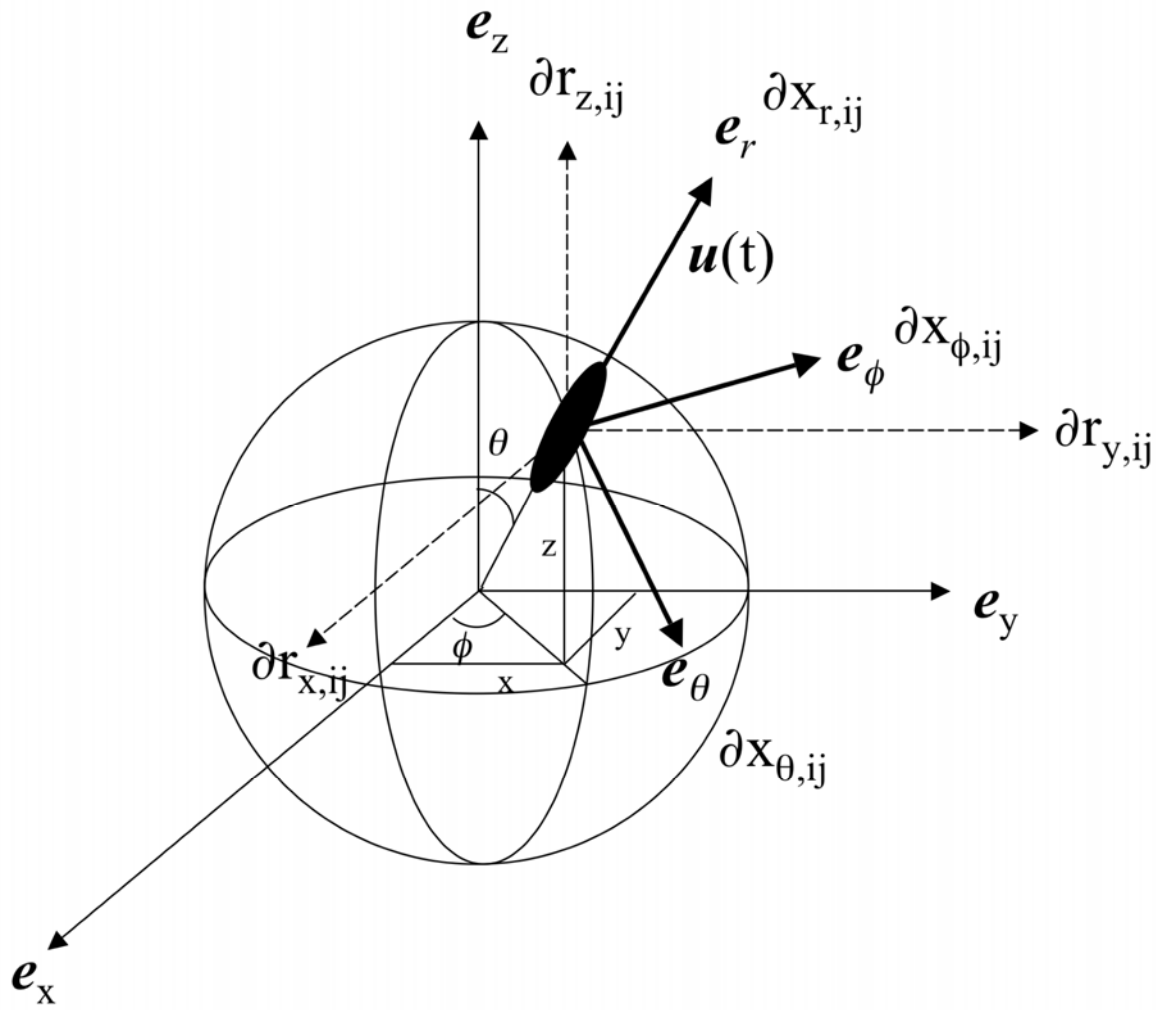


**Figure 2-2**: Schematic representation of parallel and perpendicular axes of a rod with respect to Cartesian coordinates.

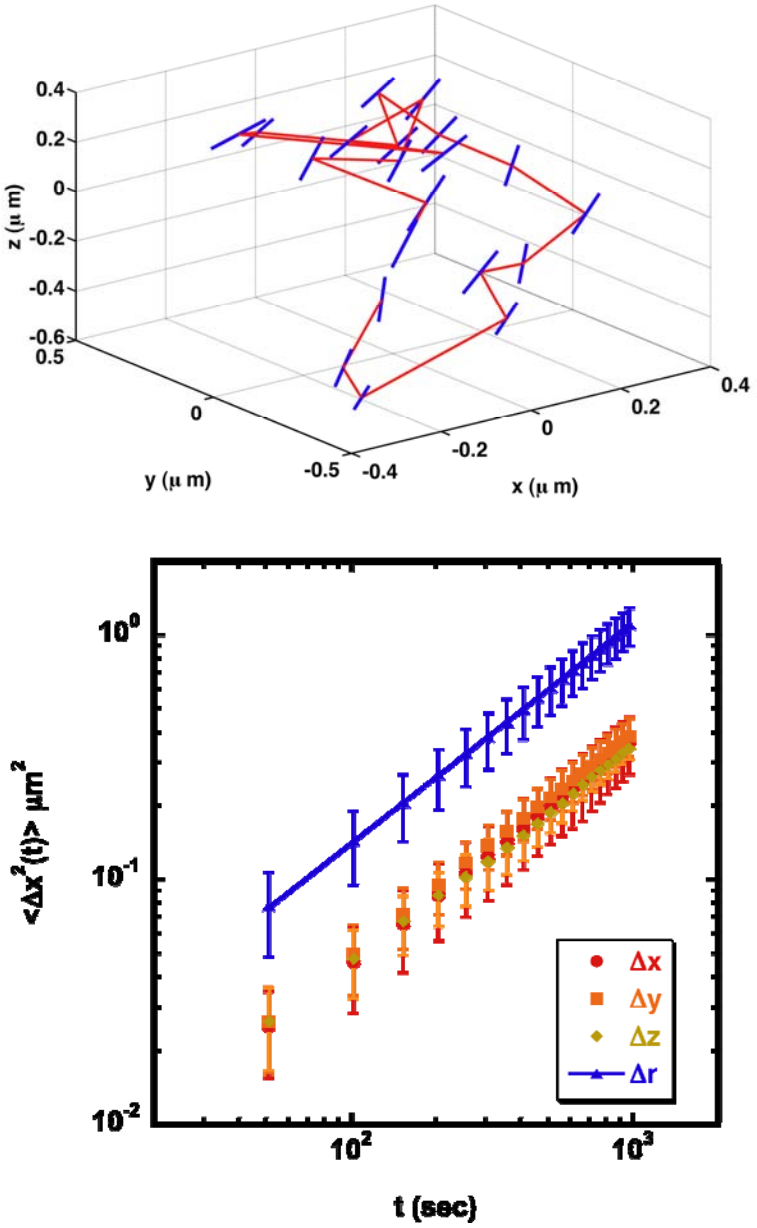


**Figure 2-3:** Laboratory frame data: (a) Rotational and translational Brownian motion of the rod-unit vector in 3D space (b) mean square displacements (averaged over all particles) in the laboratory frame for the rod of aspect ratio 3.1.

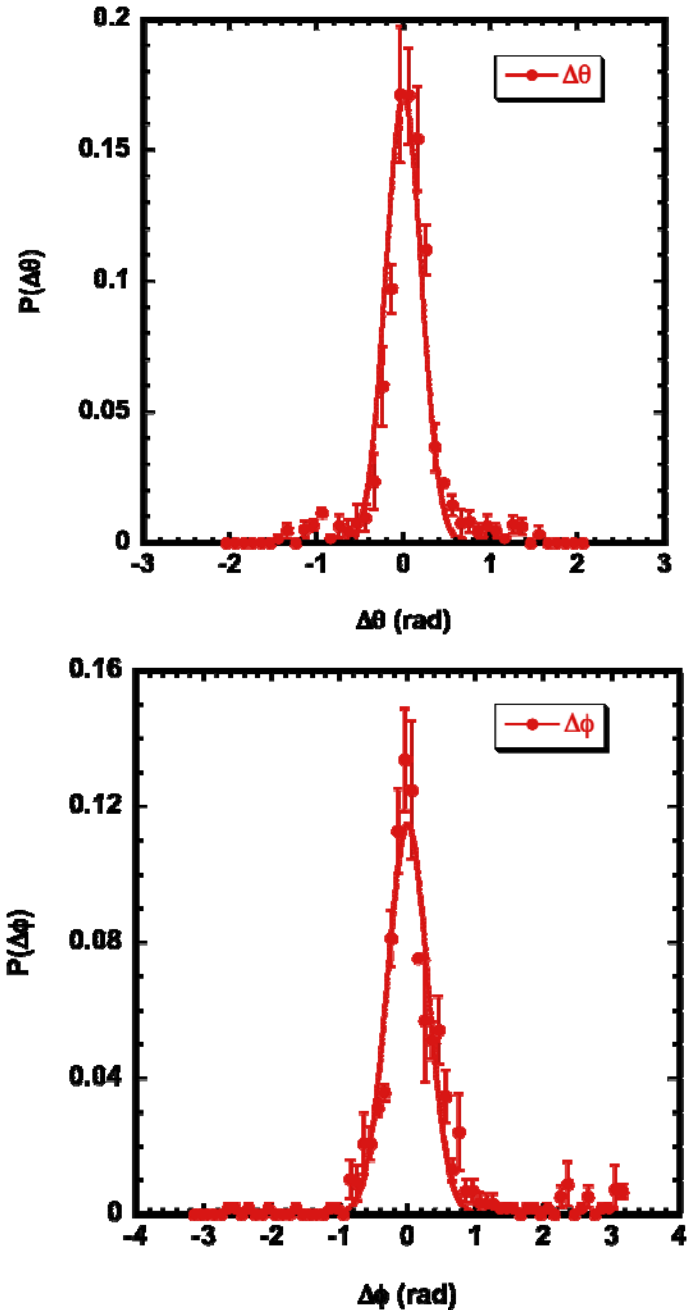


**Figure 2-4:** Probability distribution functions of (a) azimuthal and (b) polar angle (for $\Delta t$ =153 s) and their Gaussian fits for rods of aspect ratio 3.1. The curves are best fits of a Gaussian function.

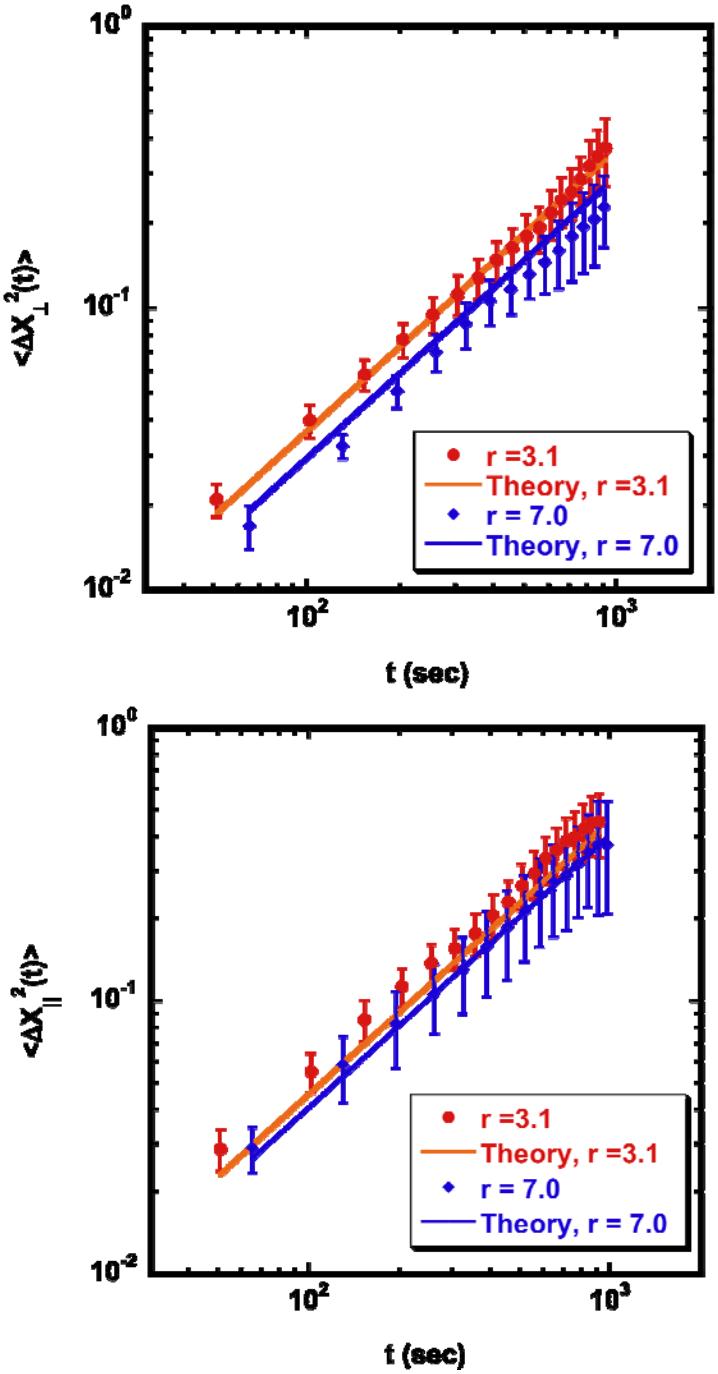


**Figure 2-5:** Comparison between experimental and theoretical values for (a) rod parallel and (b) rod perpendicular translational mean square displacements for colloidal rods of aspect ratios 3.1 and 7.0.

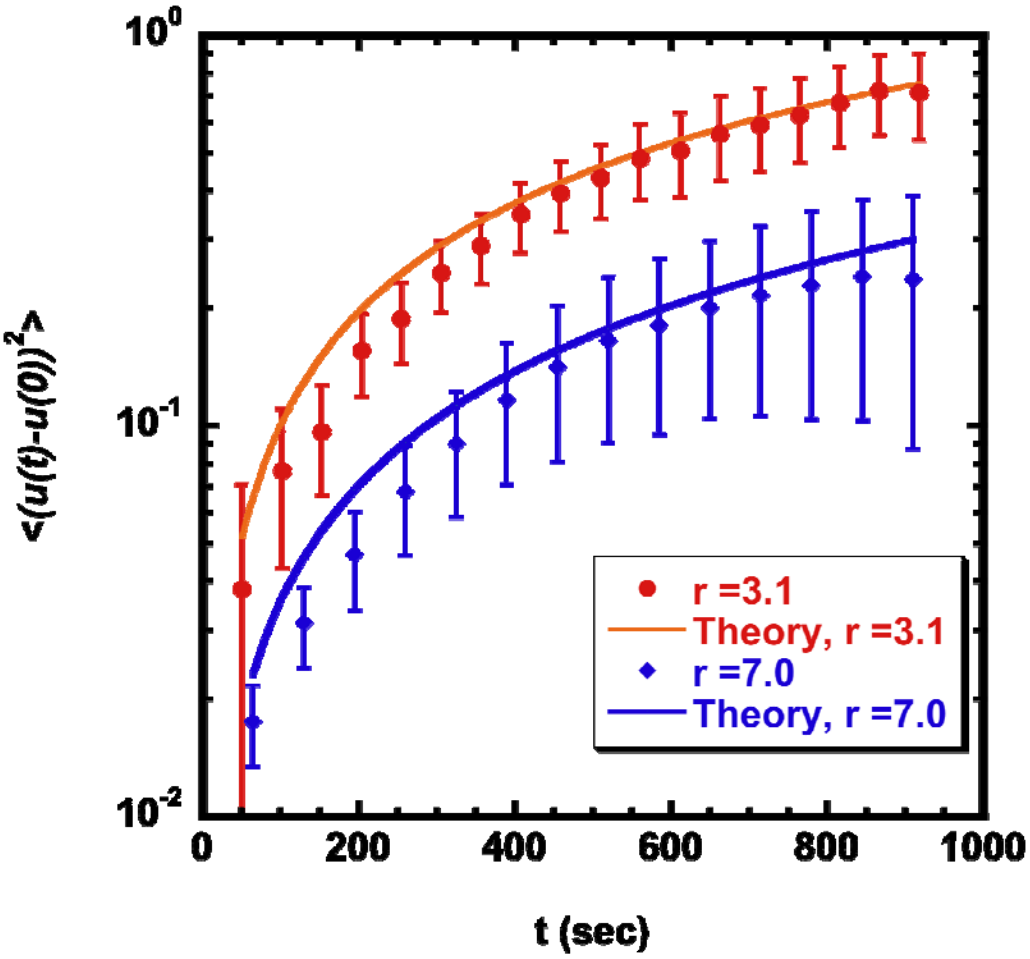


**Figure 2-6:** Comparison between experimental and theoretical values for the mean square displacement of the rod unit vector for the colloidal rods of aspect ratios 3.1 and 7.0.

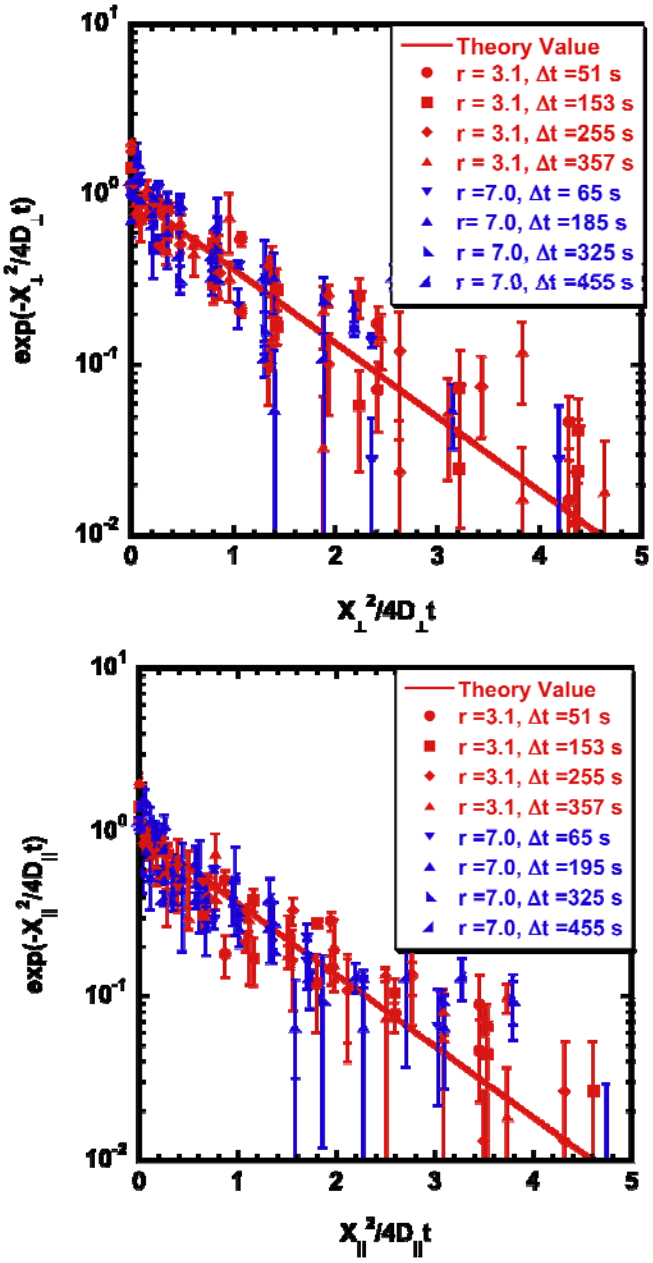


**Figure 2-7:** Probability distribution function for translational displacement along axes parallel (a) and perpendicular (b) to the rod unit vector.

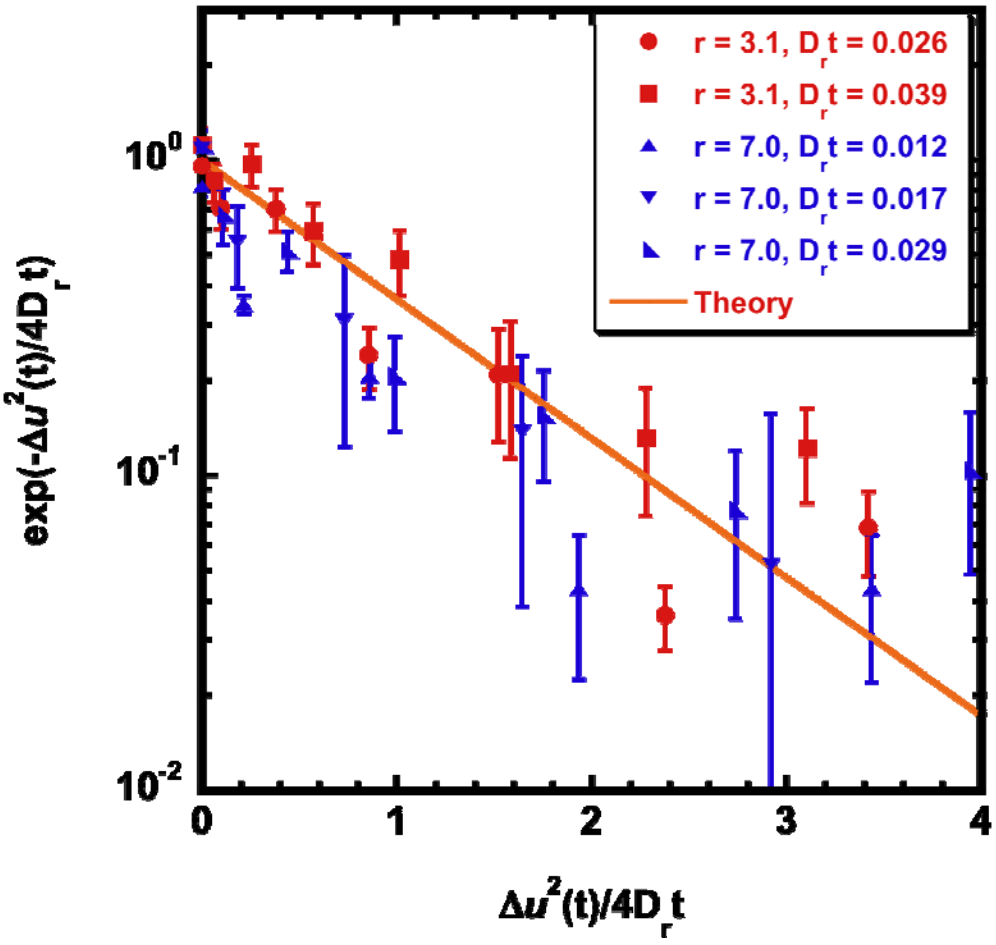


**Figure 2-8:** Probability distribution function for rotational displacement of the rod unit vector for Drt <<1.

## References


1. M. A. Horsch; Z. Zhang; S. C. Glotzer, *Nano Letters* **2006,** 6, (11), 2406-2413.
2. C. M. van Kats; P. M. Johnson; J. van den Meerakker; A. van Blaaderen, *Langmuir* **2004,** 20, (25), 11201-11207.
3. G. M. Whitesides; M. Boncheva, *Proceedings of the National Academy of Sciences of the United States of America* **2002,** 99, (8), 4769-4774.
4. R. Cush; D. Dorman; P. S. Russo, *Macromolecules* **2004,** 37, (25), 9577-9584.
5. L. Hong; S. M. Anthony; S. Granick, *Langmuir* **2006,** 22, (17), 7128-7131.
6. M. G. Basavaraj; G. G. Fuller; J. Fransaer; J. Vermant, *Langmuir* **2006,** 22, (15), 6605-6612.
7. A. Donev; I. Cisse; D. Sachs; E. Variano; F. H. Stillinger; R. Connelly; S. Torquato; P. M. Chaikin, *Science* **2004,** 303, (5660), 990-993.
8. G. H. Koenderink; D. Aarts; A. P. Philipse, *Journal of Chemical Physics* **2003,** 119, (8), 4490-4499.
9. A. Mohraz; D. B. Moler; R. M. Ziff; M. J. Solomon, *Physical Review Letters* **2004,** 92, (15), 155503.
10. A. Mohraz; M. J. Solomon, *Langmuir* **2005,** 21, 5298-5306.
11. S. Sacanna; L. Rossi; B. W. M. Kuipers; A. P. Philipse, *Langmuir* **2006,** 22, (4), 1822-1827.
12. Z. Y. Tang; Z. L. Zhang; Y. Wang; S. C. Glotzer; N. A. Kotov, *Science* **2006,** 314, (5797), 274-278.
13. J. K. Phalakornkul; A. P. Gast; R. Pecora, *Journal of Chemical Physics* **2000,** 112, (14), 6487-6494.
14. M. P. B. van Bruggen; H. N. W. Lekkerkerker; G. Maret; J. K. G. Dhont, *Physical Review E* **1998,** 58, (6), 7668-7677.
15. S. M. Anthony; L. Hong; M. Kim; S. Granick, *Langmuir* **2006,** 22, (24), 9812-9815.
16. Y. Han; A. M. Alsayed; M. Nobili; J. Zhang; T. C. Lubensky; A. G. Yodh, *Science* **2006,** 314, (5799), 626-630.
17. M. P. Lettinga; E. Barry; Z. Dogic, *Europhysics Letters* **2005,** 71, (4), 692-698.
18. C. J. Dibble; M. Kogan; M. J. Solomon, *Physical Review E* **2006,** 74, 041403.
19. V. Prasad; D. Semwogerere; E. R. Weeks, *Journal of Physics-Condensed Matter* **2007,** 19, (11), 113102.
20. E. R. Weeks; J. C. Crocker; A. C. Levitt; A. Schofield; D. A. Weitz, *Science* **2000,** 287, (5453), 627-631.
21. D. V. Boger, *Journal of Non-Newtonian Fluid Mechanics* **1977,** 3, (1), 87-91.
22. S. C. Glotzer; M. J. Solomon; N. A. Kotov, *Aiche Journal* **2004,** 50, 2978-2985.
23. K. M. Keville; E. I. Franses; J. M. Caruthers, *Journal of Colloid and Interface Science* **1991,** 144, (1), 103-126.
24. R. Sanchez; P. Bartlett, *Journal of Physics-Condensed Matter* **2005,** 17, (45), S3551-S3556.
25. A. Yethiraj; A. van Blaaderen, *Nature* **2003,** 421, (6922), 513-517.
26. Edwards S.F; Doi M., *Oxford University Press, New York* **1986**.

27. J. C. Crocker; D. G. Grier, *Journal of Colloid and Interface Science* **1996,** 179, (1), 298-310.
28. T. Savin; P. S. Doyle, *Biophysical Journal* **2005,** 88, (1), 623-638.
29. Bird R.B., Stewart W., Lightfoot, E.N., *John Wiley & Sons Inc., New York* **1960**.
30. H. Brenner, *Int. J. Multiphase Flow* **1974,** 1, 195-347.
31. B. Happel J., H., *Low Reynolds number hydrodynamics*. Kluwer Academic Publishers: Dordrecht, 1991.
32. F. Capuani; I. Pagonabarraga; D. Frenkel, *Journal of Chemical Physics* **2006,** 124, (12).
33. J. K. G. Dhont *An Introduction to Dynamics of Colloids*. Elsevier Science B.V: Amsterdam, 1996.
34. S. D. A. Russel W.B., Schowalter W.R., *Cambridge Univ. Press, Cambridge* **1989**.

# Chapter 3

# An Experimental Investigation of Effect of Gravitational Field on Assembly of Colloidal Rods with Confocal Microscopy

## Chapter Summary

We used the centrifugation force (an effective gravitational field) as an external field to produce 3D ordered assemblies of monodisperse colloidal rods that vary from 2 to 5 microns in the length and are of aspect ratio from 3.6 to 8.0. By means of confocal laser scanning microscopy and quantitative image processing, we quantified the extent of ordering, identified variables that controlled the assembly, and evaluated possible mechanisms to explain the orientational ordering. The quality of orientational order was quantified by direct calculation of the nematic order parameter (S). The dimensionless magnitude of the applied field was assessed by means of the Peclet number, a parameter that compares the time scale for rotational diffusion to the time scale for sedimentation. Experimental data shows that the effect of field strength on order parameter is a function that displays a complex dependence on aspect ratio. However, the scaling of the results for all aspect ratio with the equilibrium isotropic-nematic volume fraction suggests that the achievement of orientational order in the sediment is principally determined by the

local volume fraction of the sediment. Non-equilibrium effects, however, perturb quantitative details of the dependence of S on the local sediment volume fraction from the known behavior for equilibrium rod suspensions. The effect of gravitational field on sediment volume fraction also varies significantly betweeen long and small aspect ratio rods at low strength of gravitational field, however, at large gravitational fields volume fraction for both large and small aspect ratio rods show similar behavior. This behavior leads to the conjecture that $\phi_{glass} \sim 1.25\phi_{nematic}$ over the aspect ratio range studied

## 3.1. Introduction

Anisotropic colloidal particles are useful building blocks for assembly of ordered arrays because they may self-organize into structures with symmetry more complex than the close-packed order typical of isotropic spheres [1-4]. Accordingly, anisotropic particles with patchy [5, 6], Janus [7-9] and faceted [10-12] morphology have been synthesized and interest in their assembly has grown. However, even for the simplest types of building blocks, unexpected effects of anisotropy on assembly arise. For example, shape anisotropy, known as anisometry, leads to a greater maximum packing fraction for ellipsoidal rods and disks than spheres [13]. In disordered aggregation, colloidal rods form denser fractal clusters than spheres [14]. Even fine details of particle shape are important: simulations predict that hard spherocylinders exhibit a smectic liquid crystal phase that is absent for the prolate spheroid shape [15, 16]. Although two-dimensional assembly of anisotropic particles on surfaces and interfaces is of interest [17-20], many applications such as optical materials require assemblies with high quality ordering in a three dimensional (3D) volume. [1]

Among such bulk, 3D colloidal phases that have been targeted for assembly from anisotropic building blocks, liquid crystal phases with orientational order are of particular interest. Orientational order in colloidal suspensions at equilibrium can be described by statistical thermodynamics. A disorder-order transition occurs as the consequence of a competition between translational and orientational contributions to the free energy. For example, Onsager's theory [21] of the isotropic-nematic phase transition for hard cylinders predicts coexistence of orientational order for combinations of aspect ratio and volume fraction that satisfy the inequality [22] $\phi \frac{L}{D}\left[4\frac{L}{D}+\frac{3(L/D}{3(L/D)+2}\right] \geq 3.29$ . Here, L and D are the length and diameter of the rod and $\phi$ is the volume fraction. Recent theory and simulation have refined the transition boundary to account for the effects of aspect ratio, volume fraction and attractive interactions [15, 16, 20, 22-26]. The implications of colloidal anisometry for equilibrium self-assembly have been amply confirmed by experiment. For example, ordered liquid crystal phases of both biological (bacteriophage fd [27], tobacco mosaic virus [28]) and synthetic colloidal rods (poly (methyl methacrylate) [29], bohemite [30], metallic [31]) of different aspect ratios have been produced. The effect of attractive interactions due to depletion forces has also been investigated [24, 27, 32-34].

Although self-assembly methods have been effective, the application of an external field to generate orientational order is also of interest for reasons of both fundamental science and technological application. Statistical thermodynamics shows that an external field is balanced locally by a spatial gradient in osmotic pressure, a quantity that itself is a sensitive function of colloid volume fraction [35]. Thus, an external field, such as a gravitational or centrifugal force, will induce a spatially varying

density field in a colloidal suspension. If the variation in colloid density spans the boundaries of an equilibrium phase transition, then interesting and useful colloidal assemblies can be achieved. External fields can also accelerate the kinetics of the assembly process, perhaps by, for example, perturbing the relative orientation of rods from isotropy [36]. This effect is also of interest for applications, since self-assembly processes can sometimes require many days to achieve completion in micron-sized colloidal suspensions [37].

Most studies of the field-assisted assembly of colloidal rods have been designed to yield 2D arrays [18, 20, 38] rather than the 3D bulk assemblies of greatest interest for applications. However, some examples of 3D field-assisted assembly have been reported, including the shear-induced assembly [39] and sedimentation [29] under earth gravity (g = 9.8 $m^2/s$) of *fd* virus and poly (methyl methacrylate) rods. In the former study, mixture of isotropic and nematic phase of attractive *fd* virus suspensions were subjected under shear. However, in the latter assembly of poly (methyl methacrylate) rods was realized under sedimentation starting from a dilute suspension. Interestingly, however, previous work using field-assisted assembly to densify colloids has been largely unsuccessful in generating liquid crystalline order from the typical initial condition of an isotropic suspension at dilute rod concentration. For example, Dogic and coworkers [40] (jcp 2000) observed that initially isotropic suspensions of bacteriophage *fd* (L/D ~ 130) compressed into sediments with isotropic orientation upon sedimentation.. Likewise, Sacanna et al. [41] found that the orientationally disordered structure of silica rods of aspect ratio 4.4 persisted up to volume fractions as great as 48% when concentrated by sedimentation or centrifugation. The sole report of field-assisted assembly of anisometric

colloids is the work of ref 29; however, even in this case orientational order was achieved only for very particular conditions.

Although generation of bulk order by field-assisted assembly has not yet been systematically demonstrated in experiments, recent computer simulations suggest that order-disorder transitions ought to be accessible by this method. For example, simulations of rigid rods of both short (r =5.0) and asymptotically long aspect ratio suggest that liquid crystal transitions are assisted by external gravitational field. In these cases, ordering is greatest at the region of highest colloidal density at the boundary of the cell against which the field acts [23, 42-44]. An increase in the field strength leads to an increase in both the sediment volume fraction and the realized degree of orientational order. Moreover, an applied field of sufficient strength can affect order-disorder transitions by broadening the region of phase coexistence. [42]

Thus, the simulation literature has suggested that external fields can concentrate colloidal rods into bulk phases with orientational order; however, generation of such order in experiments has proven elusive. In thie paper we address the question of whether or not field-assisted assembly can produce bulk nematic phases of anisotropic colloids, and if so, what are the variables that control the ordering and what is the quality of orientational ordering that can be produced. The quality of ordering in this case is quantified by the nematic order parameter *S* [23], *where S* is the largest eigenvalue of the orientation tensor **Q**, defined as

$$\mathbf{Q} = \frac{1}{n_r}\left(\sum_{i=1}^{n_r} \frac{3\mathbf{u}_i\mathbf{u}_i - \mathbf{I}}{2}\right) \qquad (1)$$

Here, $n_r$ is the number of rods in the specimen, $\mathbf{u}_i$ is the director of the $i^{th}$ rod, and **I** is the identify matrix. *S* is zero for a perfectly isotropic system while one for a perfectly aligned suspension. This quantity is simply quantified in simulation by analysis of the orientation of all the rods in the simulation box. However, an analogous experimental characterization of the order parameter has never been performed in colloidal suspensions even for equilibrium self-assembly likely because previous experiments were not performed with materials and methods in which the director of all rods in a 3D volume could be individually quantified.

In addition to establishing conditions required for ordering and the quality of orientational ordering achieved, additional scientific questions of interest include identifying the effect of aspect ratio on ordering transitions and the potential effect of dynamic arrest on the scope for achieving ordering. For example, statistical thermodynamics would predict that increasing the aspect ratio of anisometric particles would induce liquid crystallinity at lower colloidal volume fractions; however, recent simulations [45] and theories [46] of dynamic arrest suggest that vitrification of the isotropic phase could interfere with thermodynamic ordering transition as the aspect ratio of the rods becomes greater.

In this study we address these questions by studying the effect of a variable external centrifugal force on orientational order in colloidal rod suspensions. We find these Brownian rods initially prepared as dilute suspensions with isotropic structure form nematic order given application of an external field of sufficient strength. The rods studied, of aspect ratio ranging from 3.6 to 8.0, are of micron size, thereby allowing their individual positions and orientations in the sediment to be quantified by 3D confocal

microscopy. We find high quality ordering ($S > 0.6$) for regions as deep as 400 rod diameters into the sediment. We find that the ordering is controlled by the strength of the applied field relative to thermal energy, as quantified by the dimensionless group the Peclet number. At low aspect ratios, orientational order monotonically increases with this dimensionless field strength. However, at higher aspect ratios ($r \sim 8$), a glass transition intervenes and reduces the quality of orientational ordering. Relative to equilibrium self-assembly, this method of field-assisted assembly is an easy, reproducible and fast way to produce 3D colloidal assemblies with high quality orientational order.

### 3.2. Materials

The colloids studied are fluorescent rods comprised of poly(methyl methacrylate) (PMMA) that has been sterically stabilized by a surface layer of poly(dimethyl siloxane) (PDMS), here referred to as PMMA-g-PDMS rods. The particles were dispersed in a 62/38 (v/v) mixture of cyclohexyl bromide (CXB) and decalin (Sigma-Aldrich, USA), a mixture that is refractive index matched with the rods. At this ratio of CXB and decalin the rods are approximately 9% more dense than the solvent ($\Delta\rho \sim 0.1$ mg/ml).

The synthesis of fluorescent poly(methyl methacrylate)-g-poly(dimethylsiloxane) (PMMA-g-PDMS) rods was carried out as described by Mohraz and Solomon [29], Mukhija and Solomon [47] and Keville et al [48]. Briefly, colloidal spheres were subjected to uniaxial extension above their softening temperature to transform the shape of the particles from a sphere to a spheroid. Dispersion polymerization was used to synthesize fluorescent PMMA-g-PDMS colloidal spheres [48] (approximate diameter = $1.0 \pm 0.04$ μm, Dye: Nile Red).

These colloidal spheres were then suspended in a polymerizable liquid (silanol-terminated PDMS, 50,000 cS, lot # 20850086, United Chemical Technologies, USA). An elastic matrix was formed by subsequent polymerization and cross-linking with methylhydro-dimethyl siloxane (25-35 cS, Lot # 20850039, United Chemical Technologies, USA). The elastic matrix was then subjected to uniaxial extension after heating it above the glass transition, $T_g$ ($T_{heating}$ =195°C) of the colloidal particles for 20 minutes. The spheroidal shape of the particles was fixed by cooling the material to a temperature below $T_g$. Finally, chemical degradation (degradation mixture: 0.01 g sodium methoxide in 5.0 g isopropyl alcohol for a film of mass approximately 1.0 g) of the matrix released the spheroids from the elastic film. The colloids were allowed to sediment and then were transferred to the test solvent once the supernatant was removed. Spheroids of aspect ratio 3.6 ± 0.2 (L and D of 2.8 (± 0.11) and 0.78 (± 0.03) μm, respectively), 5.0 ± 0.3 (L and D of 3.30 (± 0.13) and 0.66 (± 0.03) μm, respectively) and 8.0 ± 0.6 (L and D of 4.50 (± 0.16) and 0.56 (± 0.04) μm, respectively) were synthesized by applying different extensions to the films. Here L and D are major and minor axis dimensions of the rods, respectively. Scanning electron microscopy (SEM) was used to characterize the dimensions and shape of the model colloids. We analyzed approximately 40 particles from the images to determine the dimension of each rod system studied using the freely available software ImageJ64 (available for download at *rsb.info.nih.gov/ij/download.html*).

Stable rod dispersions in the 62/38 binary mixture of cyclohexyl bromide (CXB) and decalin were prepared by mixing the solvents and the rods with a vortex mixer. Except in the case of a study of the effect of initial volume fraction on assembly,

typically an approximately 2 % (w/v) dispersion of colloidal rods was subjected to different centrifugation speeds in custom-made centrifugation cells. The shape of the centrifugation cell is shown in Figure 1a. The centrifugation cell was constructed by mounting a cylindrical glass vial of inner diameter (I.D.) 4 mm and height 1.5 cm on a round glass cover-slip (thickness 0.16-0.19 mm, diameter 1.2 cm). The thickness of the cover slip was chosen to allow imaging through the bottom of the cell with an oil immersion objective. Another round ring of I.D. 1.0 cm (outer diameter 1.2 cm) and height 1.0 cm was mounted on the cover slip. The space between the two rings was filled with PDMS (Sylgard 184 elastomer kit, Ellswoth Adhesive, WI) and polymerized to support the cell so that it could sustain the applied centrifugal force (cf. Figure 1a). The orientation of the cell relative to the applied gravitational field was typically as shown in Figure 1a; however, the orientation of the container relative to the field was found to not affect the results presented here. For example, the colloidal nematic phases introduced in Fig. 1 were equally well produced by centrifugation if the cell was rotated by 90° relative to the configuration shown in Fig. 1a. The dominant orientation of the rods in this case was also perpendicular to the applied field. Thus, the observed nematic ordering is purely a consequence of the applied field strength, rather than the orientation of the field relative to the container geometry.

In a typical experiment about 300 μl of rod suspension was added to the cell. Based on the results of the study to determine the time required to reach steady-state (discussed subsequently), samples were typically subjected to 12 hours of centrifugation in a desktop device (Allegra$^{TM}$ 21R, Beckman Coulter, Inc., USA) at the desired speed before being imaged on the confocal microscope. The time between the cessation of

centrifugation and imaging was typically about 15 min. However, this time did not significantly affect results because of the slow, immobilized dynamics of the dense rod sediments. The rotation (spin) speed of the centrifuge was varied from 100 rpm to 10000 rpm. The rotation arm (R) of the centrifuge was 6 cm long. Therefore, the effective gravitational force ($g' = \omega^2 R$) varied from 0.67g to 6700g. Here, $\omega$ is the rotation frequency ($2\pi/N$, here N is revolutions per seconds) and $g = 9.8\ m/s^2$ is the gravitational constant.

A confocal laser scanning microscope (Leica TCS SP2, Leica Microsystems Wetzlar, Germany) was used to acquire 3D image volumes of the sediment structure. Imaging was performed with a 100× oil immersion objective (numerical aperture 1.4). Except for experiments in which the volume fraction profile of the sediment was quantified (c.f. Fig 1C), a 3D image stack of approximate dimension 20 x 20 x 20 $\mu m^3$ was typically collected. The bottom edge of the image volume was typically located ~ 5-10 μm above the bottom of the centrifuge tube, since this region was the densest part of the sediment. The offset of the image volume from the lower boundary was introduced to allow all rods in the volume to be located by image processing. Each image of the stack was acquired at a pixel size of 0.0407 μm x 0.0407 μm. Each stack was comprised of approximately 500 images with a slice spacing of 0.0407 μm. The time of acquisition of each image volume was ~ 8 minutes. Note that in the frame of the microscope the centrifugation force was applied in a direction parallel to the objective plane. Thus, the major axis of rods with in plane nematic order in the figures are oriented perpendicular to the applied field.

We used image-processing algorithms followed by data analysis to extract quantitative information from the image volumes collected. These codes find, in three dimensions, the position and orientation of the central backbones of all the rods in the specimen by applying an anisotropic intensity maxima criterion. The detailed description of the image processing method is published elsewhere [29]. The method uses the fact that in fluorescence confocal microscopy the region of maximum intensity of a rod lies on its central axis (backbone). Briefly, an anisotropic local brightness criterion to identify the backbone (major axis) of the colloidal rod is applied to the image stack after Gaussian filtering. Moments of the backbone configuration are then computed to identify centroid location and orientation of spheroids. As discussed in our ref 47, the errors in locating the centroid of any spheroids are approximately 55 nm in the objective plane and and 45 nm along an axis perpendicular to objective plane. The error in the orientation of the rod director, **u**, is a function of rod aspect ratio. The error is greatest at lowest aspect ratio. For r = 3.1, the error is approximately 0.25 radians. [47]

Our simulations showed that the Mohraz and Solomon [29] algorithm for estimation of the rod orientation from second moment properties of the rod backbone introduced systematic error (estimated magnitude ~ 10%) in the orientation of directors pointed nearly parallel to any of the three Cartesian axes. The error was linked to the finite width of the rod backbone along directions perpendicular to its major axis. This effect was resolved by computing the orientation angle with the following method: First, the image processing backbone was split into two half-lengths and the average position of each was found by averaging points of the half-backbones. Second, the orientation of the rod was determined from the best-fit line between these two points and the rod centroid.

After implementation of this method, the systematic error in orientation was reduced to less than 2%, as tested by processing of simulated rod images.

Thus, the image-processing algorithm yields the orientation angles (both polar and azimuthal) and centroid location of rods in the specimen. Rod orientation angles are then used to construct its unit vector **u,** which is subsequently used to measure the nematic order parameter (*S*).

### 3.3. Results and Discussion

Since this study seeks to determine the role of an effective gravitational field on the orientational ordering of micron-sized rods, optimum conditions for the experiments were evaluated. Figure 3.1 reports results of a typical centrifugation experiment. Figure 3.1a shows of the orientation of the centrifugation cell relative to the direction of imaging and the direction of the applied gravitational field. The cell was placed in the centrifuge such that the bottom of the tube was perpendicular to the direction of centrifugation; therefore the sediment is formed at the bottom of the cell. Since the objective was placed below the bottom of the cell, the direction in which image stacks were collected was also perpendicular to the direction of applied gravitational field.

From classical simulations of rod sedimentation, the volume fraction of rods in the sediment will be a maximum at the bottom of the container and thus, at any condition, the greatest potential for observing ordering is at this region. Figure 3.1b, c illustrate typical results at 2000 rpm for a suspension of rods of r = 3.6 and an initial volume fraction of 2 %. Figure 3.1b shows a CLSM image of the rod sediment in the plane parallel to the imaging objective. The image, Figure 3.1b, suggests that a very high rod concentration is observed at the bottom of the container. This high concentration persists

far into the sediment – about 400-600 rod diameters, before rapidly falling to zero at the sediment boundary. This axial dependence of rod concentration is consistent with typical behavior of colloidal sediments at steady-state [35].

We measured the local volume fraction of the sediment at different heights as extracted from image processing and plot these results in Figure 3.1c. The plot shows that the volume fraction remains almost a constant for the dense part of the sediment and becomes close to zero where structure becomes sparse. For this strength of gravitational field, the magnitude of the volume fraction in the densest region, $\phi \sim 0.52$, is consistent with the existence of orientational order at equilibrium conditions. However, note that the quality ordering is not as great as suggested by simulation: Tjipto-Margo and Evans (1990) [49] predicted a nematic phase with order parameter above 0.7 at this $\phi$; however, we measure $S = 0.37 \pm 0.03$ for this sediment. The maximum concentration of the rods includes at least a region extending from height 10D to 220D, where D is the (minor axis) diameter of the rod. We found that the region of high density was not a strong function of study parameters such as centrifugation speed and aspect ratio. Thus, to study these effects, we typically imaged a 3D volume extended from about 10D to 220D for all experiments.

Figure 3.1d shows the two-dimensional projection of one of the three dimensional image stacks acquired for analysis of sediment structure. Figure 3.1e presents the reconstruction of this image stack, once image processing and rendering algorithms are applied to it. We present the accuracy of our image-processing algorithm by comparing this regenerated image with the projection of original image stack (Figure 3.1d). The regeneration of image stack depicts the original stack very well.

The initially homogeneous concentration of rods requires time to respond to the effective gravitational force that is imposed by centrifugation. Two separate studies were conducted at two different centrifugation speeds for aspect ratio 3.6 rods at an initial rod volume fraction of 2 % to assess the time required to achieve a steady-state concentration profile. For these experiments (executed at about the device's lowest and highest centrifugation speeds of 100 rpm and 10,000 rpm), Figure 3.2 shows how the order parameter (*S*) of sediments evolves with centrifugation duration of 6, 12, 24 and 40 hours. Figure 3.2 also shows that the order parameter *S* of the two sediments achieves steady-state conditions within about 12 hours. We thus compare all samples by subjecting them to centrifugation times of 12 hours. Other properties of the image volumes, such as the sediment volume fraction, are also unchanged after 12 hours.

Finally, simulations of rod assembly show an effect of initial volume fraction on the equilibrium volume fraction profile of rods in sedimentation. Simulations suggest that at low initial volume fractions, the final sediment structure will be isotropic while if the initial volume fraction is higher, the nematic phase will be observed at the bottom of the sediment [23]. Therefore, simulations suggest that there is a minimum volume fraction below which formation of nematic phase is not possible. Although our scope to characterize this effect of initial volume fraction is limited (because the small quantity of model material does not allow the freedom to operate at high initial volume fractions), Figure 3.3 presents data to assess this effect. A set of experiments was conducted at initial volume fractions of 0.5%, 1% and 2% for rods of r ~3.6 at 10,000 rpm for 12 hours. No ordering was observed for the volume fraction of 0.5% but ordering was seen for volume fractions of 1% and 2%. Therefore, it appears that initial volume fractions of

1% or greater are sufficient to lead to final near-wall sediment conditions that allow for a nematic phase. Thus, all experiments were conducted at 2% initial volume fraction.

To report subsequent data, we seek a dimensionless measure of the field strength. A number of complementary approaches are available. The first, reported by refs 23 and 42 scales a gravitational potential energy evaluated over the rod diameter on thermal energy, $\beta = mg'L/kT$. Here m is the buoyant mass, g' is the effective gravitational acceleration and L is the length of rods. The, second compares the time scale for rotational diffusion to the time scale for sedimentation. This quantity is the Peclet number (Pe), and equation 2 shows its dependent on aspect ratio and length of the rod.

$$Pe = \left(\frac{mg'}{6\pi\eta L^2 D_{r0}}\right) = \frac{mg'L}{18k_B T(\ln(2r - 0.5))} \qquad (2)$$

Here $D_{r0}$ is the rotational diffusivity of the rod and r is the aspect ratio of the rod. The two measures, $\beta$ and Pe, are related through the equation $\beta = 18\ Pe\ (\ln(2*r-0.5))$. Here, r is the aspect ratio of the rod. The difference between the two parameters increases with increasing aspect ratio. At the low aspect ratio studied here ($r < 10$), the two differ by at most a factor of 50. We prefer the latter measure to report data because it explicitly quantifies a potential effect for rotational diffusion on the propensity for ordering, and thus allows for the possibility of non-equilibrium ordering effects in a straightforward way.

We applied different effective gravitational fields (g') by varying the spin speed of the centrifuge. For this study, $0.67g < g' < 6700g$. This range corresponds to a Peclet number varying from 0.04 to 400 for the rods of aspect ratio 3.6.

Confocal microscopy images that present the qualitative effect of centrifugation on ordering are shown in Figure 3.4. These images were acquired in the region where the

colloidal volume fraction in the sediment was the greatest as discussed earlier. (The plane of these images is perpendicular to the direction of the effective gravitational field induced by centrifugation). Suspensions of the rods of aspect ratio 3.6 (initial volume fraction = 2 % were centrifuged at 100, 500, 1000, 2000, 4000, 6000 and 10,000 rpms for 12 hours to achieve these sediments. The corresponding values of Pe are 0.04, 1.0, 4.0, 16, 64, 144 and 400 respectively. The images, in which the value of Peclet number varies from 0.04 in Figure 3.4a to 400 in Figure 3.4, show qualitative effects of the applied field on the in-plane ordering. Qualitatively, an increase is observed in both volume fraction and ordering with increasing gravitational force. We note that although only 2D images are shown, rods were fully aligned in 3D across the full image volume (of dimension ~ 10 rod lengths).

In Figure 3.5, we plot the dependence of the nematic order parameter (*S*), computed as per eqn (1), on the Peclet number (dimensionless field magnitude) for these sediments. The value of *S* increases from 0.12 to 0.56 when the gravitational field is increased from 0.67g to 6700g (over the span of two decades of Peclet number), consistent with the images of Figure 3.4. The increase in S is accompanied by an increase in sediment volume fraction, as report in Table 3.1. For example, for S = 0.12, $\phi = 0.18$, while the volume fraction of the most ordered sediment (S = 0.56) is $\phi = 0.58$. We also notice that initially (Pe $\leq$ 16) volume fraction and the nematic order parameter both increase rapidly with increase in Peclet number while on a further increase in the Peclet number (Pe > 16) volume fraction does not change as rapidly as the nematic order parameter.

There are two possible hypotheses to explain this observed trend of nematic order parameters. The first hypothesis would be to apply theory and simulation results developed to understand the order-disorder transition for equilibrium systems of colloidal rod suspensions [21, 49]. In this case, the location of the isotropic-nematic transition in sedimentation is purely based on the competition between configurational and orientational entropy in the system, which, for hard rods, is determined uniquely by the local volume fraction of the sediment. In this case, the value of the nematic order parameter S is zero for the isotropic phase ($\phi < \phi_{nem}$). The nematic phase ($\phi \geq \phi_{nem}$) has a non-zero value of the nematic order parameter and S increases with the volume fraction. According to ref 40, application of local equilibrium ideas to the field-assisted assembly process of sedimentation requires that, $\frac{12k_BT}{mg'L} >> 1$. For the system reported in Figure 3.5, this criterion is met only for the first data point (Pe = 0.04). For the whole data set, this quantity varies between $7.0 \times 10^{-3}$ and 7.0.

The second hypothesis to explain the onset of ordering in Figure 3.5 is based on a non-equilibrium effect of the applied field. An example of a non-equilibrium effect would be a preferred orientation of the rods induced by the applied field that is subsequently locked in by the high rod concentration. Such an effect, dependent on the balance between field-induced alignment and orientational disorder induced by rotational diffusion, would be controlled by the magnitude of the Pe number. Indeed, theory and simulation of rod ordering under gravitational field suggests that the applied field can affect both the location of the isotropic-nematic transition and the breadth of its coexistence region [23, 42]. Theory also suggests that increasing the gravitational

strength increases the nematic order parameter of the suspension in the nematic phase [43] relative to the equilibrium case.

Although both hypotheses are plausible, it is difficult to distinguish between them by means of Figure 3.5 alone. Therefore, to gain more insight into the mechanism we studied the effect of aspect ratio on the ordering. Because the equilibrium volume fraction for the nematic transition is a sensitive function of aspect ratio, the equilibrium hypothesis would predict substantial changes in the S vs Pe behavior reported in Figure 3.5.

Rods of aspect ratio 5.0 and 8.0 were subjected to various gravitational fields that varied from 6g to 6700g. For example, Figure 3.6 (a-f) reports confocal microscopy images of centrifugation experiments for colloidal rods of aspect ratio 8.0. As before, the plane of these images is perpendicular to the direction of the effective gravitational field induced by centrifugation. The image stacks were collected approximately 5-10 μm above the coverslip. These results, for r = 8.0, suggest a very different dependence of orientational ordering on Peclet number than the low aspect ratio (r = 3.6) data of Figure 3.5. Indeed, Figure 3.7 compares S vs Pe for the two aspect ratios, as well as additional data for r = 5.0. While S monotonically increases with Pe for r = 3.6 and 5.0, it monotonically decreases with Pe for r = 8.0. Table 3.1 and 3.2 reports the sediment volume fractions that accompany these order parameters and Peclet numbers.

Interestingly, the above experimental results suggest that a high gravitational field has adverse effects on ordering for rods of aspect ratio 8.0. That is, at low Peclet numbers the rod densification, and thus the I-N transition, is facilitated by centrifugation. Indeed, simulations suggest that the *I-N* transition volume fraction for rods (ellipsoids) of aspect

ratio 8.0 is 0.29 [49] are for our experiments the volume fractions at which S > 0.5 is observed is approximately 0.40. However, despite the ordering at low dimensionless field strengths, at high spin speeds and Pe number, ordering progressively deteriorates.

To understand the qualitatively different results for the rods of different aspect ratios, we present Figure 3.8, a plot of S vs $\phi/\phi_{nem}$ for rods of aspect ratio 3.6, 5.0 and 8.0. Here the sediment volume fraction is normalized by the volume fraction of the nematic phase, as per Tjipto-Margo and Evans (1990) [49] for ellipsoids. Although the Pe dependence of orientational ordering in these suspensions differs significant (cf. Figure 3.7), interestingly, the data collapse to a single curve when the local volume fraction is scaled on the equilibrium thermodynamic transition. This collapse provides strong support for a role for the equilibrium isotropic-nematic transition is mediating orientational order in this field-assisted assembly operation.

In Figure 3.8, we also plot the equilibrium theoretical predictions of *S* for ellipsoids of aspect ratio 5.0 and 10.0 [49]. The theory predicts a transition to a finite S at $\phi/\phi_{nem} \sim 1$ and the experiments are consistent with this point. There are, however, four interesting differences between the theory and experiment. First, the magnitudes of the measured order parameters are less than the equilibrium theory. For example, at $\phi/\phi_{nem} \sim 1.2$, the theory is shifted upward from the experiment by about 50%. Second, while theory predicts an abrupt transition from isotropic to nematic phase, a much smoother transition is observed for experimental measurements. Third, the concavity of the dependence of S on $\phi/\phi_{nem}$ differs – the theory is concave downward, the experiments are concave upward. Fourth, the experiments show a finite S for $\phi/\phi_{nem} < 1$, a region for which the equilibrium theory predicts S = 0.

Figure 3.8, also allows us to check the validity of our equilibrium vs non-equilibrium hypothesis behind the ordering. If the assembly were completely governed by equilibrium free energy minimization, the order parameter will strictly depend on the volume fraction of the sediment i.e. S = 0 for $\phi/\phi_{nem} < 1$ and a concave downward dependence of S on $\phi/\phi_{nem}$ would result for the entire volume fraction range. However, the experiments deviate significantly from these trends. Thus, although the primary driver for the development of field-assisted orientational order appears to be thermodynamic, since all the data are well correlated by the parameter $\phi/\phi_{nem}$, non-equilibrium effects appear to play a significant secondary role, because the form of the S vs $\phi/\phi_{nem}$ measurements deviate from the equilibrium theory.

Figure 3.8 therefore suggests that the role of the applied field strength on orientational ordering is principally mediated by the sediment volume fraction that results from the application of the centrifugal force. That is, although non-equilibrium effects play a role in the magnitude of S for a particular sediment, whether or not a certain spin speed will achieve a nematic sediment is principally determined by what the local volume fraction that results from application of the applied field. Thus, the most significant effect of the field is to densify the rod suspension. In Figure 3.9, we examine that effect by plotting $\phi/\phi_{nem}$ vs Pe for all the aspect ratios studied.

The plot suggests that initially ($Pe <\sim 10^1$) the dependence of volume fraction on Peclet number for long aspect ratio rods (r =8.0) is very different from low aspect ratio rods of 3.6 and 5.0. However, for $Pe >\sim 10^2$, the results for the different aspect ratio rods increasingly coverage to a volume fraction that is ~ $1.25*\phi_{nem}$. The physical origin of this complex behavior is unknown at this time. However, we note the following two

points. First, the monotonically increasing results for the low aspect ratio rods are qualitatively consistent with expectations for how increase in applied field strength would affect the sedimentation; volume fraction, however, we can think of no reason based on equilibrium considerations why the sediment volume fraction ought to plateau at $\phi \sim 1.25*\phi_{nem}$ with increasing field strength. Second, the monotonically decreasing dependence of $\phi$ with Pe is very hard to reconcile with equilibrium ideas. How could an increased applied field strength lead to a less dense sediment in a system at local equilibrium?

These observations lead to the hypothesis that a non-equilibrium mechanism explains the Figure 3.9 results. Our conjecture is that the phenomena that intervenes is the rod glass transition, and that the plateau at high Pe in Figure 3.9 suggest that $\phi_{glass} \sim 1.25*\phi_{nem}$ for the aspect ratio ($r \sim 3$-8) range studied here. A loss of ergodicity could explain both observations discussed above. Indeed, the earlier theory of Edwards and Evans suggests that $\phi_g \sim C*\phi_{nematic}$, where C is a constant of order unity [50]. The more detail calculations of ref 46, suggest that $C \sim 0.9$ and 0.8 for spherocylinders of aspect ratio 5.0 and 0.8, respectively [46]. Experimentally, Buining and Lekkerkerker (1993) have observed $C \sim 1.4$ for boehmite rods of aspect ratio 20.0 [30].

The intervention of the rod glass transition at higher Peclet numbers could also be the reason for the observed discrepancy in the theoretical (equilibrium predictions) and the experimental values of *S* for $\phi > \phi_{nem}$. Since intervention of the glassy state would retard the macroscopic phase separation between the isotropic and nematic state, the glass transition might explain why *S* was found to be lower than the theoretically predicated values in Figure 3-8.

## 3.4. Conclusions

In this study, we investigated the role of gravitational field to produce ordered assemblies of colloidal rods. We applied a gravitational field over a range of strengths to dilute suspensions of colloidal rods of various aspect ratios (r = 3.6 to 8.0) and found that the volume fraction of the sediment was the principal determinant of the observed orientational ordering. An isotropic to nematic phase transition of the field-assisted assembly agreed well with the predictions of equilibrium thermodynamics. Gravitational field plays a significant role in desifying the suspension and determining the value of order parameter. Suspensions of rods of different aspect ratios, however, responded in different ways to the applied field. For example, we observed a continuous increase in the ordering with an increase in Peclet number for rods of aspect ratio 5.0 and less. In contrast, ordering decreased with increasing Peclet number for rods of aspect ratio 8.0 because the glass transition intervenes at higher field strengths.

This study is the first experimental work to produce ordered assembly of colloidal rods using gravitational field. However, the experimental results deviate from theoretical predictions; which predict an increase in the order parameter of assembly with an increase in gravitation field, irrespective of the aspect ratio of the rod. Previous theoretical and simulation work done to understand the assembly of colloidal rods under gravitational field does not consider the possibility of a glass phase. This experimental work, however, requests development of new theory to incorporate the possibility of glass transition.

**Table 3-1:** Dependence of volume fractions and nematic order parameter of aspect ratio 3.6 rod sediments on Peclet number.

| **rpm** | **g'** | **Pe** | **$\phi$** | **S** |
|---|---|---|---|---|
| 100 | 0.67g | 0.04 | 0.18 | 0.12 |
| 500 | 17g | 1.0 | 0.35 | 0.21 |
| 1000 | 67g | 4.0 | 0.44 | 0.26 |
| 2000 | 270g | 16 | 0.52 | 0.37 |
| 4000 | 1100g | 64 | 0.57 | 0.43 |
| 6000 | 2400g | 144 | 0.55 | 0.52 |
| 10000 | 6700g | 400 | 0.58 | 0.56 |

**Table 3-2:** Dependence of volume fractions and nematic order parameter of aspect ratio 8.0 rod sediments on Peclet number.

| **rpm** | **g'** | **Pe** | **$\phi$** | **S** |
|---|---|---|---|---|
| 300 | 6g | 0.40 | 0.43 | 0.52 |
| 500 | 17g | 1.0 | 0.41 | 0.54 |
| 1000 | 67g | 4.0 | 0.42 | 0.49 |
| 2000 | 270g | 16 | 0.41 | 0.48 |
| 4000 | 1100g | 62 | 0.34 | 0.42 |
| 10000 | 6700g | 400 | 0.36 | 0.38 |

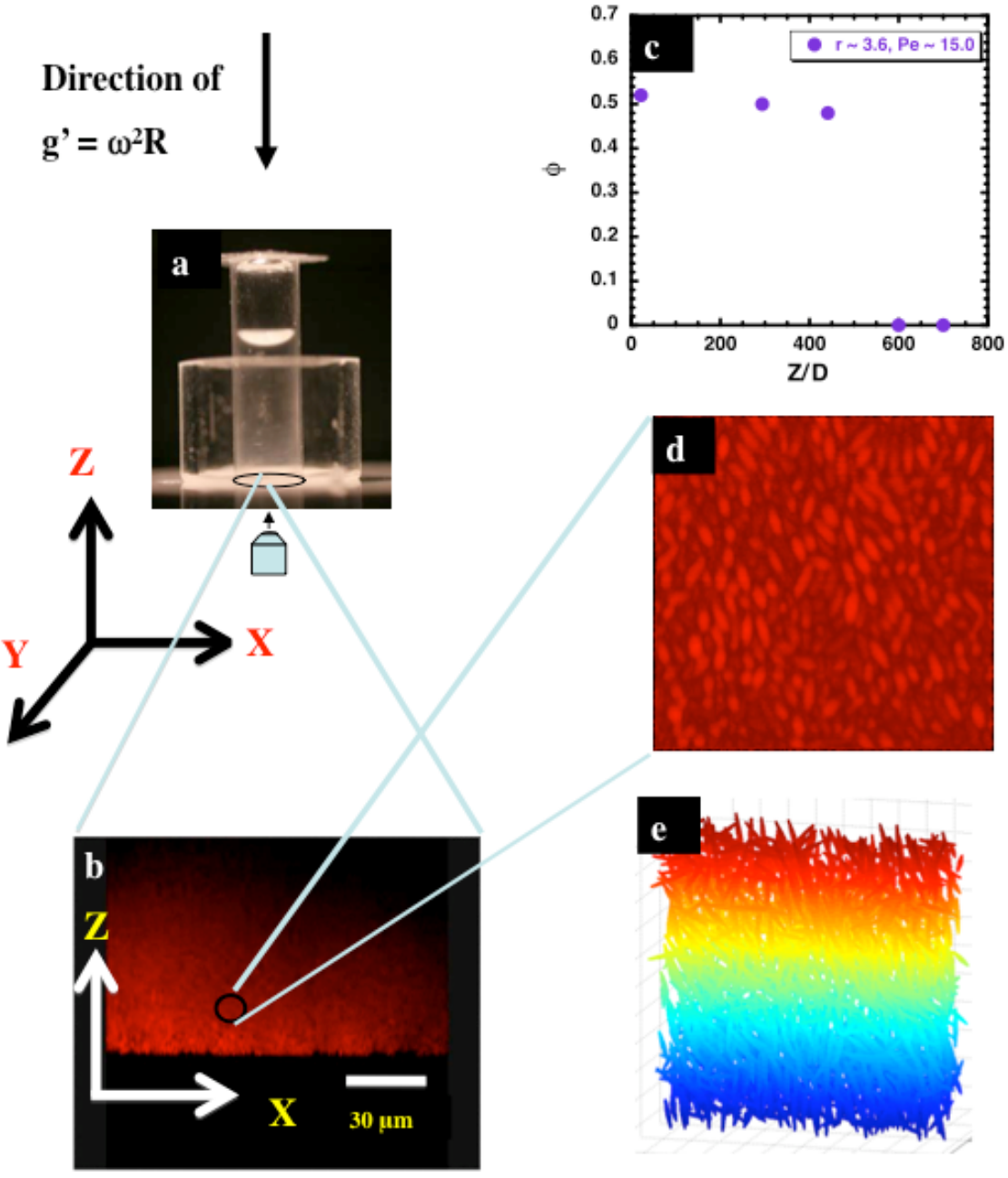


**Figure 3-1:** a) Design of centrifugation cell and the direction of gravitational field. b) CLSM image of a sediment (2000 rpm, r = 3.6, 2 % (w/v) init. vol. frac.) in the plane parallel to the direction of gravitational field. c) Dependence of final volume fraction on height from coverslip. d) 2D projection of a 3D image volume collected for data analysis and e) Reconstruction of the image volume.

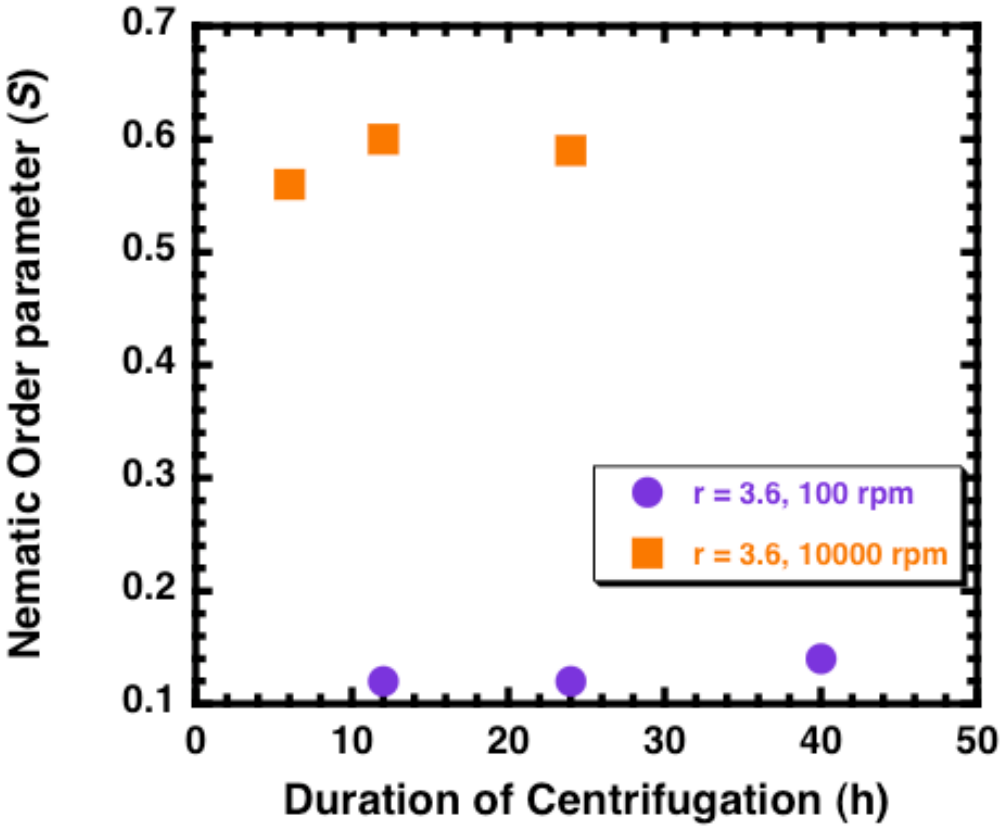


**Figure 3-2:** Time dependence of nematic order parameter for rods of aspect ratio 3.6 at 100 and 10000 rpm centrifugation speeds.

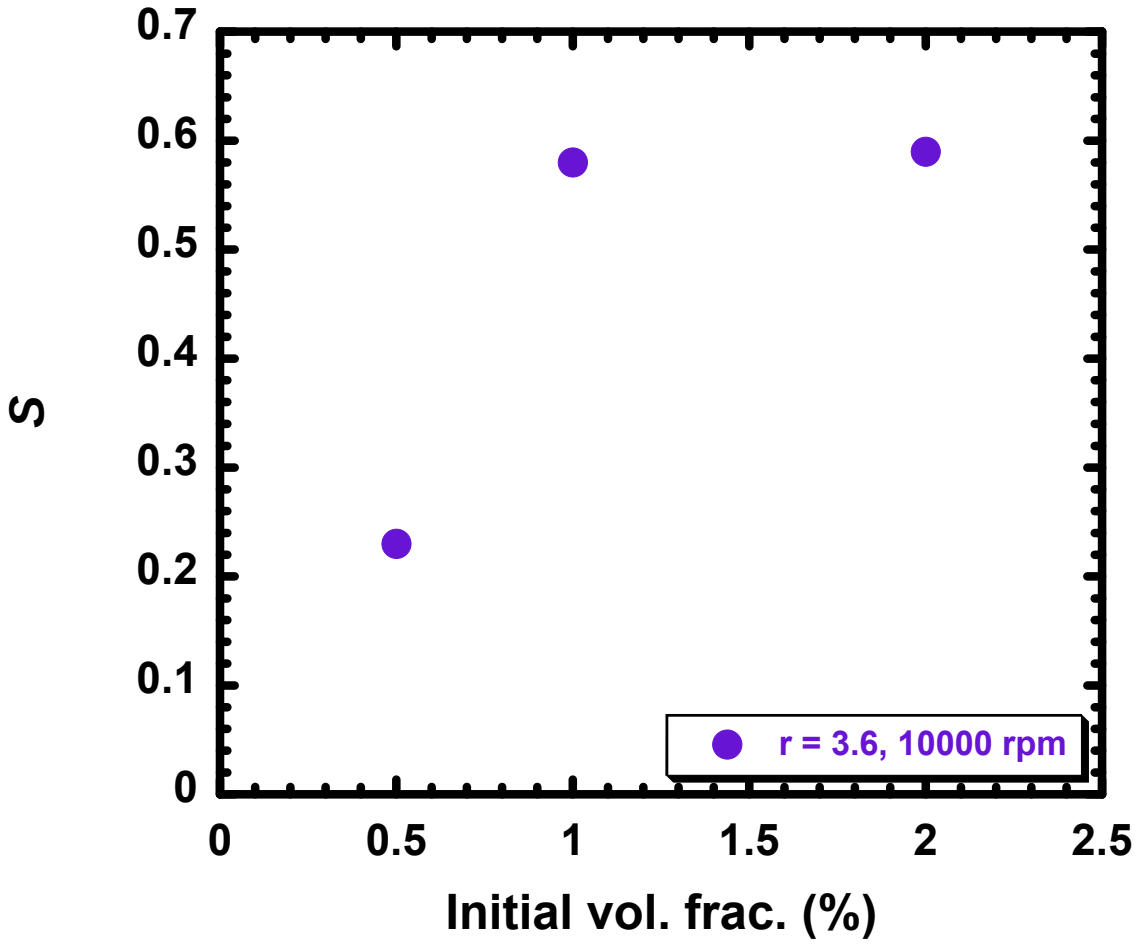


**Figure 3-3:** Dependence of nematic order parameter on initial volume fraction of suspension for rods of aspect ratio 3.6 experiment conducted at 10000 rpm centrifugation speed.

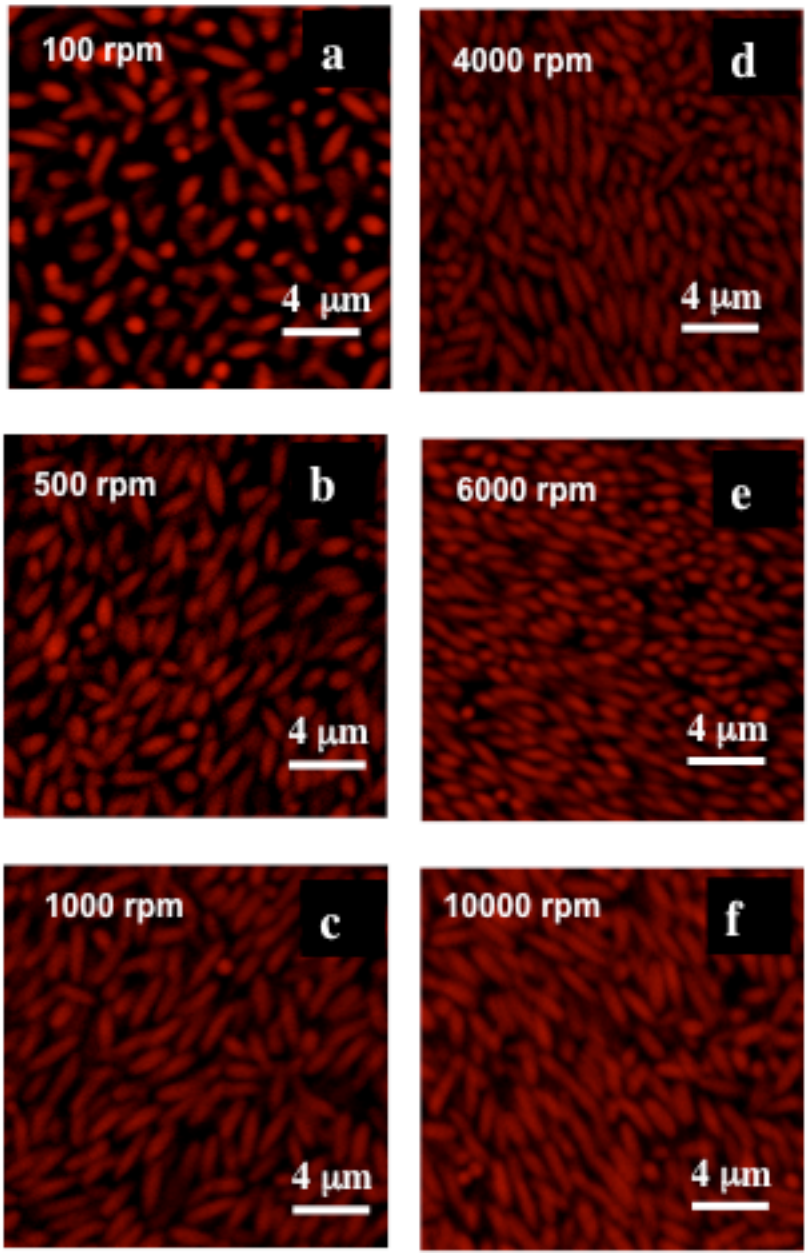


**Figure 3-4:** Confocal Laser scanning microscopy images of sediments made under different gravitational fields for the rods of aspect ratio 3.6 in the increasing order of spin speed. The images are acquired in the plane that is perpendicular to the direction of applied gravitational field.

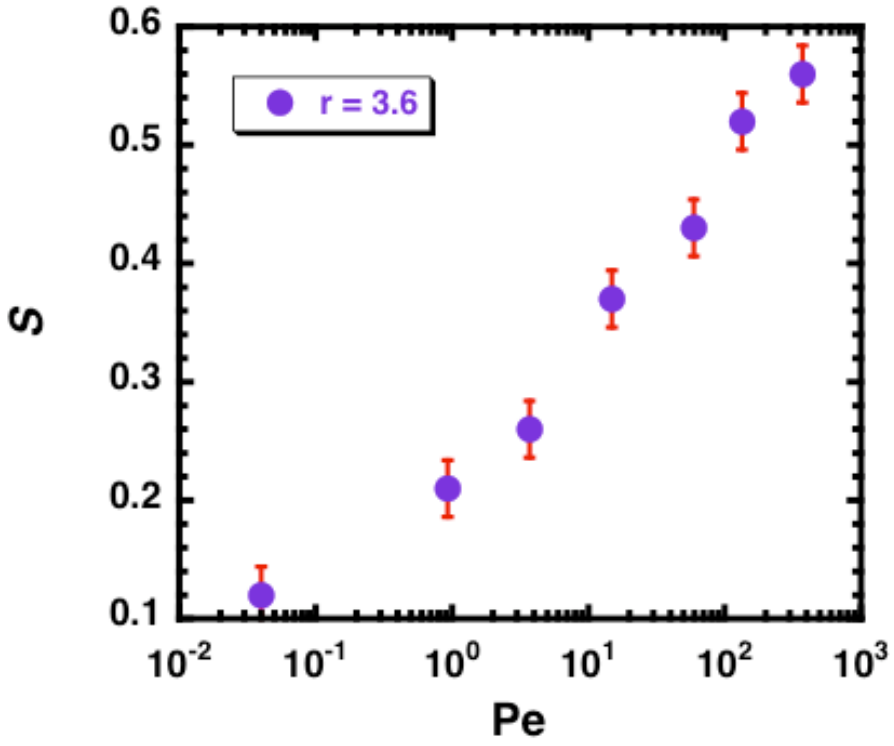


**Figure 3-5:** Dependence of nematic order parameter (S) on the Peclet number (Pe) for the rods of all the aspect ratios 3.6.

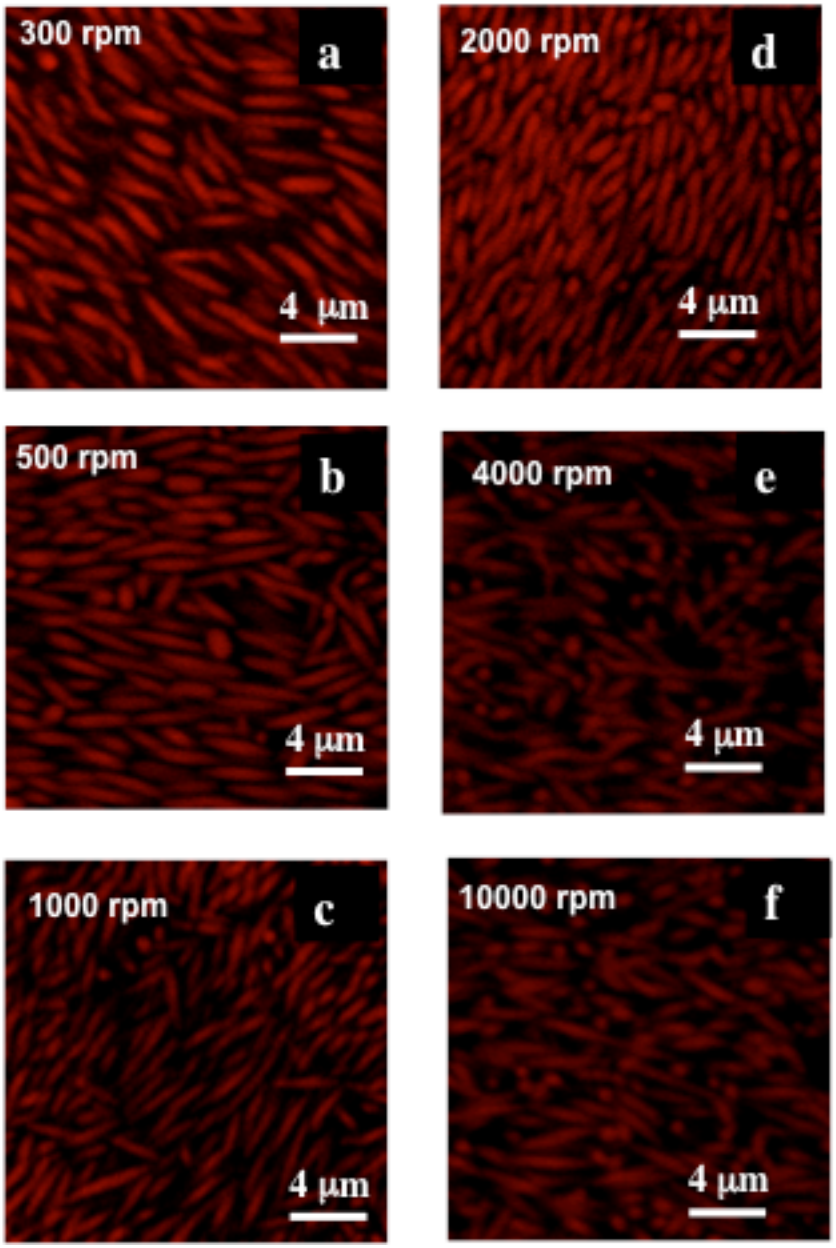


**Figure 3-6:** Confocal Laser scanning microscopy images of sediments made under different gravitational fields for the rods of aspect ratio 8.0 in the increasing order of spin speed. The images are acquired in the plane that is perpendicular to the direction of applied gravitation field.

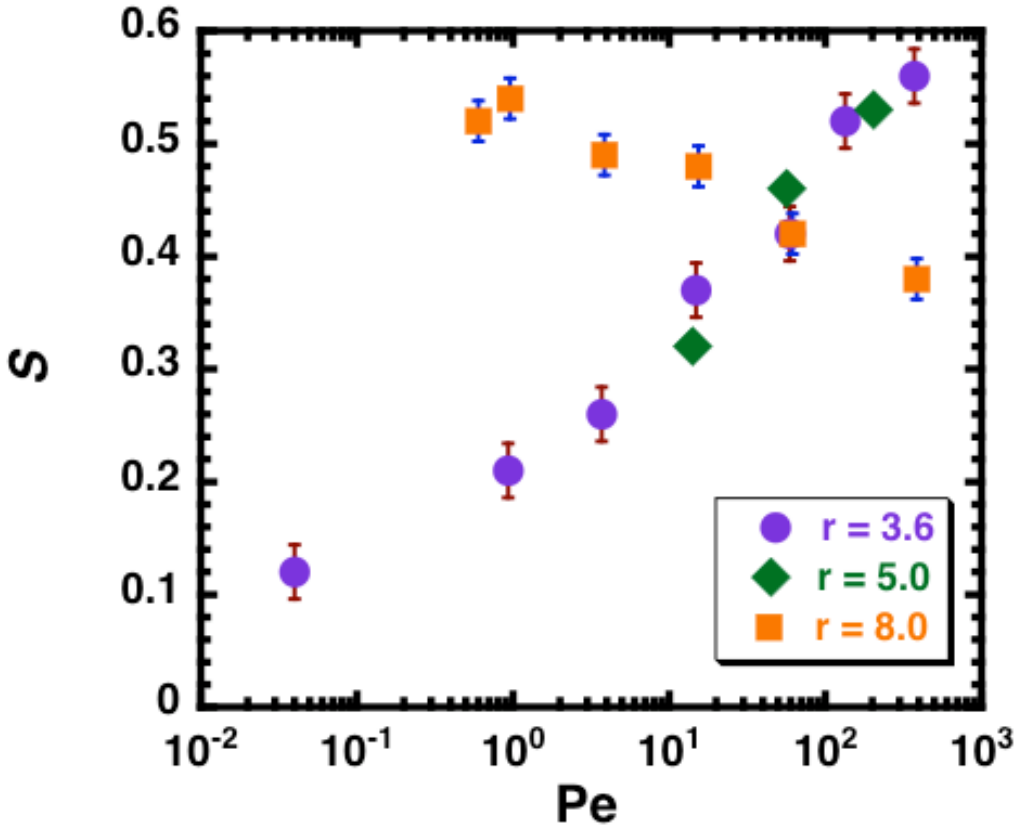


**Figure 3-7:** Dependence of nematic order parameter (S) on the Peclet number (Pe) for the rods of all the aspect ratios 3.6, 5.0 and 8.0.

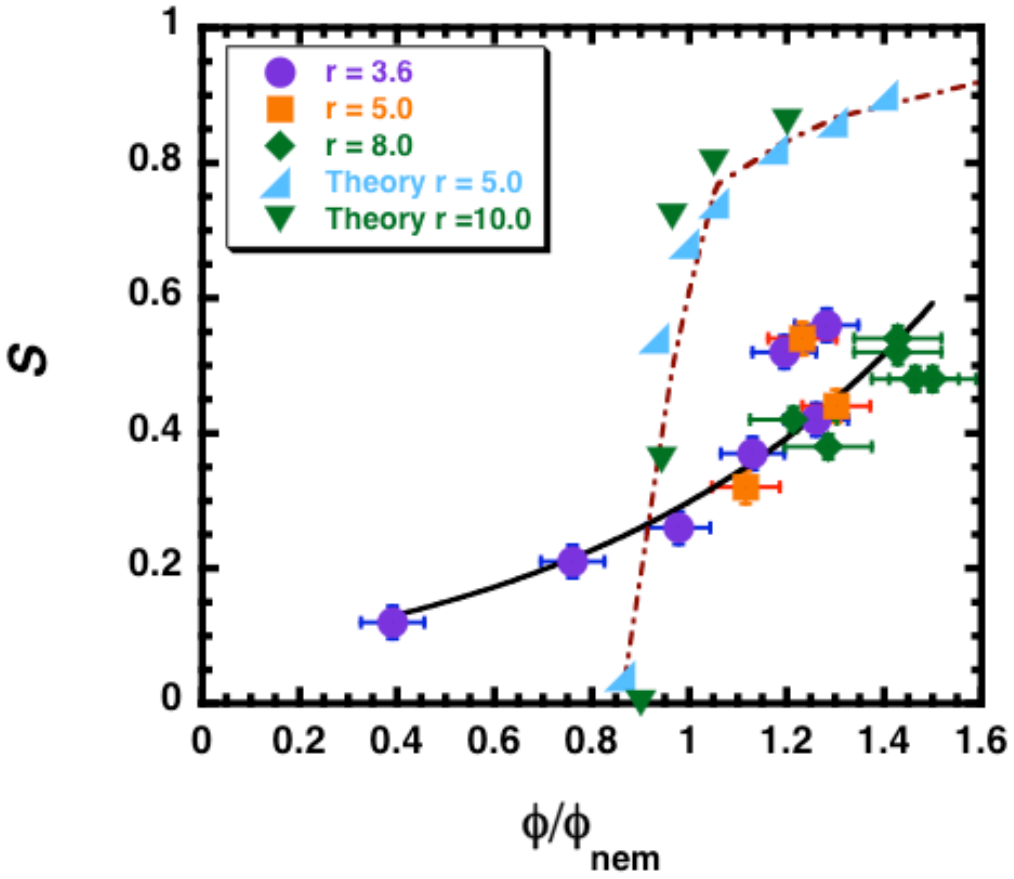


**Figure 3-8:** Dependence of nematic order parameter (S) on the volume fraction ($\phi$) for the rods of aspect ratio 3.6, 5.0 and 8.0.

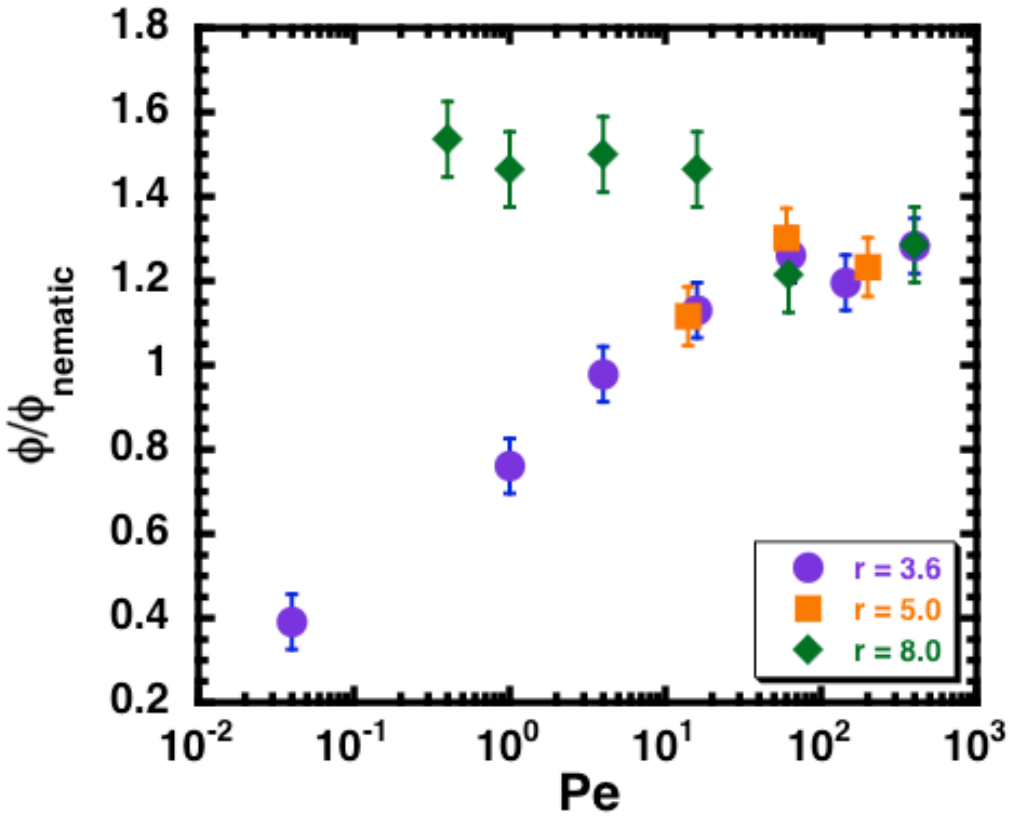


**Figure 3-9:** Dependence of dimensionless volume fraction on the Peclet number for the rods of aspect ratio 3.6, 5.0 and 8.0. The values of $\phi_{nem}$ adopted from Tjipto-Margo and Evans, 1990 for hard ellipsoids.

## References


1. G. M. Whitesides; M. Boncheva, *Proceedings of the National Academy of Sciences of the United States of America* **2002,** 99, (8), 4769-4774.
2. M. A. Horsch; Z. Zhang; S. C. Glotzer, *Nano Letters* **2006,** 6, (11), 2406-2413.
3. S. C. Glotzer; M. J. Solomon, *Nature Materials* **2007,** 6, (8), 557-562.
4. Z. L. Zhang; S. C. Glotzer, *Nano Letters* **2004,** 4, (8), 1407-1413.
5. T. T. Chastek; S. D. Hudson; V. A. Hackley, *Langmuir* **2008,** 24, (24), 13897-13903.
6. A. B. Pawar; I. Kretzschmar, *Langmuir* **2008,** 24, (2), 355-358.
7. A. Perro; S. Reculusa; S. Ravaine; E. B. Bourgeat-Lami; E. Duguet, *Journal of Materials Chemistry* **2005,** 15, (35-36), 3745-3760.
8. D. Dendukuri; D. C. Pregibon; J. Collins; T. A. Hatton; P. S. Doyle, *Nature Materials* **2006,** 5, (5), 365-369.
9. K. H. Roh; D. C. Martin; J. Lahann, *Nature Materials* **2005,** 4, (10), 759-763.
10. T. Kubo; M. Hogiri; H. Kagata; A. Nakahira, *Journal of the American Ceramic Society* **2009,** 92, (1), S172-S176.
11. C. M. Muller; F. C. F. Mornaghini; R. Spolenak, *Nanotechnology* **2008,** 19, (48), 12.
12. C. S. Du; J. D. Yun; R. K. Dumas; X. Y. Yuan; K. Liu; N. D. Browning; N. Pan, *Acta Materialia* **2008,** 56, (14), 3516-3522.
13. A. Donev; I. Cisse; D. Sachs; E. Variano; F. H. Stillinger; R. Connelly; S. Torquato; P. M. Chaikin, *Science* **2004,** 303, (5660), 990-993.
14. A. Mohraz; M. J. Solomon, *Journal of Colloid and Interface Science* **2006,** 300, (1), 155-162.
15. A. Bezrukov; D. Stoyan, *Particle & Particle Systems Characterization* **2007,** 23, (5), 388-398.
16. P. Bolhuis; D. Frenkel, *Journal of Chemical Physics* **1997,** 106, (2), 666-687.
17. B. Madivala; J. Fransaer; J. Vermant in: *Self-assembly and surface rheology of 2D suspension of ellipsoids*, 15th International Congress on Rheology/80th Annual Meeting of the Society-of-Rheology, Monterey, CA, Aug 03-08, 2008; A. Co; L. G. Leal; R. H. Colby; A. J. Giacomin, (Eds.) Amer Inst Physics: Monterey, CA, 2008; pp 1054-1056.
18. S. P. Wargacki; B. Pate; R. A. Vaia, *Langmuir* **2008,** 24, (10), 5439-5444.
19. M. G. Basavaraj; G. G. Fuller; J. Fransaer; J. Vermant, *Langmuir* **2006,** 22, (15), 6605-6612.
20. B. Q. Sun; H. Sirringhaus, *Journal of the American Chemical Society* **2006,** 128, (50), 16231-16237.
21. L. Onsager, *Annals of the New York Academy of Sciences* **1949,** 51, (4), 627-659.
22. A. P. Philipse, *Langmuir* **1996,** 12, (24), 5971-5971.
23. S. V. Savenko; M. Dijkstra, *Physical Review E* **2004,** 70, (5), 051401.
24. H. N. W. Lekkerkerker; A. Stroobants in: *Phase-Behavior Of Rod-Like Colloid Plus Flexible Polymer Mixtures*, I International Conference on Scaling Concepts

and Complex Fluids, Copanello, Italy, Jul 04-08, 1994; Copanello, Italy, 1994; pp 949-962.
25. P. J. Camp; M. P. Allen, *Journal of Chemical Physics* **1997,** 106, (16), 6681-6688.
26. J. A. C. Veerman; D. Frenkel, *Physical Review A* **1990,** 41, (6), 3237-3244.
27. Z. Dogic; K. R. Purdy; E. Grelet; M. Adams; S. Fraden, *Physical Review E* **2004,** 69, (5), 051702.
28. A. Nedoluzhko; T. Douglas, *Journal of Inorganic Biochemistry* **2001,** 84, (3-4), 233-240.
29. A. Mohraz; M. J. Solomon, *Langmuir* **2005,** 21, (12), 5298-5306.
30. P. A. Buining; H. N. W. Lekkerkerker, *Journal of Physical Chemistry* **1993,** 97, (44), 11510-11516.
31. H. Maeda; Y. Maeda, *Physical Review Letters* **2003,** 90, (1), 4, 018303.
32. M. Adams; Z. Dogic; S. L. Keller; S. Fraden, *Nature* **1998,** 393, (6683), 349-352.
33. Z. Dogic; S. Fraden, *Current Opinion in Colloid & Interface Science* **2006,** 11, (1), 47-55.
34. M. P. B. van Bruggen; H. N. W. Lekkerkerker, *Macromolecules* **2000,** 33, (15), 5532-5535.
35. S. D. A. Russel W.B., Schowalter W.R., *Cambridge Univ. Press, Cambridge* **1989**.
36. T. Schilling; D. Frenkel, *Physical Review Letters* **2004,** 92, (8), 085505.
37. M. P. B. van Bruggen; H. N. W. Lekkerkerker in: *Metastability and multistability: Gelation and liquid crystal formation in suspensions of colloidal rods*, 2nd International Conference on Self-Assembled Fibrillar Networks, Autrans, France, Nov 24-28, 2001; Amer Chemical Soc: Autrans, France, 2001; pp 7141-7145.
38. C. J. Orendorff; P. L. Hankins; C. J. Murphy, *Langmuir* **2005,** 21, (5), 2022-2026.
39. M. Ripoll; P. Holmqvist; R. G. Winkler; G. Gompper; J. K. G. Dhont; M. P. Lettinga, *Physical Review Letters* **2008,** 101, (16), 168302.
40. Z. Dogic; A. P. Philipse; S. Fraden; J. K. G. Dhont, *Journal of Chemical Physics* **2000,** 113, (18), 8368-8380.
41. S. Sacanna; L. Rossi; A. Wouterse; A. P. Philipse, *Journal of Physics-Condensed Matter* **2007,** 19, 376108.
42. V. A. Baulin, *Journal of Chemical Physics* **2003,** 119, (5), 2874-2885.
43. V. A. Baulin; A. R. Khokhlov, *Physical Review E* **1999,** 60, (3), 2973-2977.
44. J. Hu; X. J. Qiu; R. X. Li, *Journal of Biological Physics* **2006,** 32, (6), 497-506.
45. T. A. Schilling; D. Frenkel, *Computer Physics Communications* **2005,** 169, (1-3), 117-121.
46. G. Yatsenko; K. S. Schweizer, *Langmuir* **2008,** 24, (14), 7474-7484.
47. D. Mukhija; M. J. Solomon, *Journal of Colloid and Interface Science* **2007,** 314, (1), 98-106.
48. K. M. Keville; E. I. Franses; J. M. Caruthers, *Journal of Colloid and Interface Science* **1991,** 144, (1), 103-126.
49. B. Tjiptomargo; G. T. Evans, *Journal of Chemical Physics* **1990,** 93, (6), 4254-4265.
50. S. F. Edwards; K. E. Evans, *Journal of the Chemical Society-Faraday Transactions Ii* **1982,** 78, 113-121.

# Chapter 4

# Effect of non-adsorbing polymer on assembly of colloidal rods under sedimentation

## Chapter Summary

In this study the effect of depletion forces on ordering of colloidal rods under the action of centrifugation was investigated. Experiments were conducted at constant gravitational field strength while, the depletion strength, was controlled by varying the concentration of the polymer added. The rod suspensions studied are fluorescent poly(methyl methacrylate) colloids that are 2 to 5 micron in length and 4.0 to 8.0 in aspect ratio. Confocal laser scanning microscopy was used to image the three-dimensional ordering/structure. Three dimensional image volumes were analyzed using image-processing algorithms to extract the quantitative data. The ordering of the final sediment structures was then quantified by measuring nematic order parameter ($S$). We find that suspensions of small aspect ratio rods ($r \leq 5.0$) respond differently to the depletion and gravitational field when compared to the rods with longer aspect ratios ($r \sim 8.0$). For small aspect ratio rods, experiments showed that an increase in the polymer concentration leads to an increasing trend in the ordering. Further addition of polymer greater than $c/c^* = 0.92$ does not show any affect on the ordering. While for the rods of

aspect ratio 8.0, we observed that an initial increase in polymer concentration leads to an increase in ordering but further addition of polymer has adverse effect upon the ordering. The addition of non-adsorbing polymer helps the ordering by increasing the I-N transition volume fraction and by controlling the mechanism of phase separation. We analyze our experimental results in the light of the theoretical work available for the individual effect of depletion and the gravitational field. We observed that the combined effect of the two parameters could be explained by the combination of the individual effect of each phenomenon.

## 4.1. Introduction

Assembly of anisometric colloidal particles into ordered structures are of fundamental and commercial interest. A better understanding of the fabrication of defect-free assemblies not only can accelerate the development of advanced materials like, photonic band-gaps, microelectronics, chemical sensors and energy transfer materials, but also will be very beneficial for the traditional industries like paints, ceramics and pharmaceutics [1-5]. The extent of ordering for these final structures also defines their rheological, optical and electronic properties. Modulation of the optical responses upon change in the ordering of colloids is a good example reported in past [6, 7]. Although efforts are made to prepare defect-free structures, but the area is still in juvenile stage and needs to be explored thoroughly. Self-assembly of colloidal particles is one of the ways of making ordered structures. Ordered structures e.g. liquid crystalline phases of both biological and synthetic colloids have been produced by equilibrium self-assembly[8-12]. However, self-assembly suffers from the limitations like particle size, polydispersity, synthesis time and quality of ordering. A unique way to counter these challenges is to

apply external forces like electric field, magnetic field, gravity and shear force [13-15]. In the previous chapter, we discussed literature related to the application of the external field for the assembly of anisometric colloids. Other than the external forces applied, addition of polymers or small molecules to the colloidal suspensions leads to the ordering. In this chapter use of external forces and role of non-adsorbing polymer to induce ordering will be investigated in detail.

Addition of a non-adsorbing polymer at various concentrations to a colloidal suspension can cause aggregation, networked structures and phase separation of the colloidal particles [16-18]. Exclusion of polymer molecules from the region between closely spaced particles leads to imbalance in the osmotic pressure. This imbalance pushes these particles together and an effective interparticle interaction is felt by the particles even if the interparticle interaction is repulsive [19]. This phenomenon is known as depletion attraction in colloidal science. There has been significant theoretical work done to explore the effect of depletion on rod ordering. The theory of Stroobants and Lekkerkerker suggests that addition of non-adsorbing polymer to a suspension of colloidal rods has a significant effect on the type of phases present in the assembly [20]. Polymer concentration, ratio of polymer diameter to the rod diameter and aspect ratio of the rods are three important parameters that govern the type of phases present into the assembly [20]. More recent simulation studies have also suggested the broadening of coexistence region with addition of polymer [21, 22].

There has been some experimental work to understand the effect of depletion on equilibrium systems of colloidal rods; however, the field is still not fully understood due to contradictory findings by different research groups. For example, the phase diagram

generated by van Bruggen and Lekkerkerker for the mixture of Boehmite rods and poly (dimethyl siloxane) suggests that at different concentrations of polymer and rods, different mechanisms of phase separation such as: nucleation and growth, spinodal decomposition, aggregation, and gelation are possible [23]. Nucleation and growth, spinodal decomposition, and aggregation lead to macroscopic phase separation into nematic and isotropic phases; however, gelation will not necessarily lead to macroscopic phase separation [23]. Addition of polymer to the rod suspension affects the ordering by increasing the overlapping excluded volume. Overlapping of the excluded volume provides more free volume to the rods; which increases the translational entropy of the rods [19]. Low and intermediate polymer concentrations favor nucleation and growth, spinodal decomposition, and aggregation pathways while at very high polymer concentrations gelation is favored. Adams et al, monitored the extent and the type of ordering of filamentous bacteriophage *fd* virus by controlling the amount of spheres (poly(ethylene glycol or polystyrene spheres) added to the suspension [19]. They found along with the rod concentration, number of added spheres also dictates the type of ordering for entropically driven systems. Depending on the relative concentration of spheres present in the assembly, either isotropic, nematic, smectic, columnar or lamellar phases were observed.

In contrast, Dogic and coworkers discovered that depletion induced by adding a non-adsorbing polymer has no effect on the order parameter and the order parameter is solely determined by the rod concentration [8, 24]. They analyzed the effect of ionic strength on the phase behavior of the mixture of rods (bacteriophage *fd* virus) and polymer (dextran). They discovered that for their experimental system, addition of the

polymer widens the isotropic-nematic coexistence region at high ionic strength while addition of the polymer has no effect on the phase transition at low ionic strength. They also found that theory severely overestimates the strength of attractions induced by polymer at any ionic strength [8, 24].

Except for few experimental studies, theoretical and experimental literature suggests that depletion can affect the assembly of colloidal rods in more than one way. Our idea is that the combination of the depletion interaction and an applied external field might control the ordering even better since both the extent of the depletion and the external field could be controlled. Depletion affects the entropy of the suspension while external field can affect entropy, density or pre-alignment of the particles in the suspension. A very little work has been done to understand the combined effect of the two. For example, in a recent study, Ripoll and coworkers studied the facilitation provided by shear to align the isotropic phase in a suspension of attractive colloidal rods [14]. *fd* virus suspensions was used as the model system and attractions (depletion) were induced by adding the polymer dextran. In their experimental and simulation study, they found that shear aligns the isotropic phase in the direction of flow; however, the nematic phase goes through a collective rotational motion without breaking. Their study suggested that external fields like shear (or, in our case potentially, sedimentation) can affect the isotropic-nematic transition of attractive colloidal rod suspensions and the combined effect of the two was more powerful than just of depletion.

Here, we study the combined effect of depletion and gravitational field on assembly of colloidal rods by adding a non-adsorbing polymer to a dilute suspension of colloidal rods and by subjecting it under gravitational field. The studies are conducted for

a range of aspect ratios ranging from r = 4.0 to r =8.0. The experimental approach applied parallels that of Chapter 3. Three dimensional structures of the final sediments are visualized by confocal laser scanning microscopy due to its unique ability to image deep into the sample. Ordering is characterized by measuring the nematic order parameter (*S*). We also characterize the volume fraction of the sediments produced by centrifugation. The strength of the applied gravitational field is quantified according to the Peclet number, a ratio of the strength of the applied field relative to the effect of rotational diffusion. Colloidal attractions are induced by addition of non-adsorbing polymer. The range of the attraction relative to the rod size is given by the ratio 2*Rg/D = 0.1. The strength of the attraction is varied by varying polymer concentration. The results are analyzed in the light of the theory that is available to understand the individual effects of non adsorbing polymer and gravitation on colloidal rod assemblies.

## 4.2. Materials and methods

Fluorescent poly (methyl methacrylate) colloidal rods that are sterically stabilized with poly (dimethyl siloxane) were used as model material for the studies. Mixture of cyclohexyl bromide (CXB) and decalin was used as solvents. Non-adsorbing polymer polystyrene (MW = 900,000) was used as the depletion agent. The range of depletion potential is controlled by the ratio of the radius of gyration of the polymer and the diameter of the rod (Rg/D), the value of this parameter for our system is 0.05.

The synthesis scheme of the colloidal rods is explained in detail in the materials section of the Chapter 3. Briefly, colloidal spheres (approximate diameter = 1.0 ± 0.04 μm, Dye: Nile Red) were heated above their glass transition temperature and subjected to a uniaxial extension to transform into spheroids. Different magnitudes of uniaxial

extensions were applied in order to achieve different aspect ratios of rods. Solvents cyclohexyl bromide and decalin were mixed in a ratio of 62 to 38 to achieve the density mismatching (rods are approximately 9% more dense than the solvent) while still maintaining the refractive index matching. Based on the initial volume fraction study conducted in Chapter 3 for the zero polymer case, colloidal rods were suspended into the solvent mixture at approximately 2 % volume fraction for the depletion studies.

Stock polymer solutions (c_stock = 0.02 g/ml) was prepared separately by suspending polystyrene (MW=900,000) into the solvent mixture of CXB and decalin (62v/38v). To avoid chain scission, the polymer suspension was prepared at slow rolling speeds (10 rpm). The radius of gyration ($R_g$) and polymer overlap concentration c* for this polymer are reported to be 41±4 nm and 0.0053 g/ml in the mixture of CXB/decalin, respectively, by Dibble and co-workers [12]. Suspensions of the colloidal rods were mixed with the polymer solution in particular ratios to obtain desired polymer concentrations. Mixture of the colloidal rod dispersion and polymer suspension was rolled gently for approximately 5 minutes before centrifugation. Custom made centrifugation cells were used for the experiments. The centrifugation cells were filled to the top with the suspension, approximately 300 μl of suspension volume was required to nearly fill the cell. Samples were subjected to 12 hours of centrifugation to in a desktop device (Allegra$^{TM}$ 21R) at the desired spin speed before imaging. Duration of the centrifugation was chosen based upon the zero polymer study. The design of the centrifugation cell and the particulars of the centrifuge are explained in detail in materials and methods section of the Chapter 3.

3D image volumes of sediment structures were acquired using a confocal laser scanning microscope (Leica TCS SP2). A 100× oil immersion objective (numerical aperture 1.4) was used for imaging. Image stacks were collected approximately 5-10 μm above the bottom of the centrifuge cell, since we found that the maximum local rod volume fraction lies in this region. Approximately 500 images of size 512 pixel X 512 pixel were collected to construct a 3D image stacks of approximate dimension 20 X 20 X 20 $\mu m^3$. The image stack was acquired at a pixel size of 0.0407 μm X 0.0407 μm with a slice spacing of 0.0407 μm. The time of acquisition of each image was approximately 0.81 seconds. Note that, in the frame of the microscope, the centrifugation force was applied in the direction which is parallel to the imaging objective (cf. Figure 3.1, Chapter 3) and the image stack was acquired by collecting images perpendicular to the direction of centrifugation force.

The quantitative information from these image stacks was extracted using image processing algorithms and data analysis tools previously discussed in Chapter 3. (The detailed description of the image processing algorithm is published in ref [10] while a brief sketch of the method along with the modifications introduced were discussed in Chapter 3.) Image processing algorithm provided us with the centroid location and the orientation angles of the each individual rod present in the image stack. The orientation angles are then used to construct its rod unit vector u (vector parallel to the rod axis). The degree of alignment is quantified by measuring nematic order parameter ($S$).

## 4.3. Results and Discussion

Because the purpose of this Chapter is to investigate the effect of attractive depletion interactions on the orientational order of rods subjected to an applied gravitational field, most experimental conditions were kept same as for zero polymer, hard rod case (as described in Chapter 3). Rods of aspect ratio ranging from 4.0 to 8.0 were used for the study. At a fixed Peclet number, non-adsorbing polymer concentration, which is proportional to the strength of attraction, was varied in order to study the influence of attractive interactions on sedimentation.

Measurements of orientational order were made in the near-wall region at the bottom of the centrifugation cell, where the rod volume fraction was the greatest. To establish the location of this region, in Figure 4.1a we plot the dependence of local rod volume fraction on the dimensionless height above the cell bottom for rods of aspect ratio 8.0 at the polymer concentration of $c/c^* = 0.34$. This experiment is conducted for an applied dimensionless field strength of $Pe = 10.0$. We measured the local volume fractions of the sediment at different heights by counting all rods at a given height, z, above the coverslip as detected by our image processing methods. In agreement with the non-polymer (hard rod) case, the highest density was observed near the bottom of the sediment. The plot shows that the volume fraction remains almost a constant in the densest part of the sediment and then rapidly decays to zero at the sediment boundary. Figure 4.1b reports a 2D confocal image that shows the transition region from a dense to a sparse sediment. The image is taken in the plane parallel to the direction of gravitational field. The lower limit of the region is located about 200 μm ($Z/D \sim 350$) above the coverslip. Since we are mainly interested in the region of the highest ordering,

imaging was conducted in the region close to the cover-slip, well below the transition in volume fraction shown in Fig 4.1b.

To quantify the effect of non-absorbing polymer on ordering, sedimentation experiments were conducted for suspensions of rods of aspect ratio 4.0 and 5.0 at a Peclet number of approximately 10.0. The polymer concentration was varied from 0 to 1.5c/c* while keeping the initial colloidal volume fraction fixed. (The initial rod volume fraction was kept at 2 %, consistent with the experiments of Chapter 3). Suspensions of the rods of aspect ratio 4.0 and 5.0 were centrifuged at 2000 rpm (Pe ~ 10.0) for 12 hours to achieve the rod sediments at varying polymer concentrations. (Experiments of Chapter 3 had indicated that 12 hours was sufficient to achieve steady-state sediments.) Figure 4.2 (a-e) shows confocal microscopy images of the sediments for the colloidal rods of aspect ratio 5.0 as non-adsorbing polymer concentration was increased. The imaging plane in these images is perpendicular to the direction of the effective gravitation field. The images, in which the polymer concentration varies from c/c* = 0 in Figure 4.2a to c/c* = 1.48 in Figure 4.2e, show qualitative effects of how polymer affects the field-assisted orientational ordering of rods of aspect ratio 5.0. Figure 4.2 suggests that orientational ordering and volume fraction of the sediments increase with increasing polymer concentration for these rods. Confocal images for the polymer study of the colloidal rods of aspect ratio 4.0 also show the same qualitative behavior as shown by rods of aspect ratio 5.0. We note that although only 2D images are shown, rods were fully aligned in 3D across the full image volume (of dimension ~ 10 rod lengths). The colloidal volume fractions of the sediments reported in Figure 4.2 are included in Table 4.1.

To additionally establish how increased attractive interactions might affect ordering of rods of higher aspect ratio, Figure 4.3 reports similar confocal micrographs for rods of aspect ratio 8.0. Similar to the rods of smaller aspect ratio, the polymer concentration was varied from 0 to 1.5c/c*. Suspensions of the rods of aspect ratio 8.0 (initial rod volume fraction = 2 %) were centrifuged at 2000 rpm (Pe ~ 10.0) for 12 hours to achieve the rod sediments at varying polymer concentrations. Figure 4.3 (a-e) show confocal microscopy images of the sediments for the colloidal rods of aspect ratio 8.0, in order of increasing polymer concentration. These suspensions had initial polymer concentrations (equivalent c/c* value) of 0, 0.34, 0.52, 0.92 and 1.23 respectively. Images in Figure 4.3, suggest an initial increase in both ordering and volume fraction with an increase in polymer concentration (Figure 4.3 (a-c)). This increase is followed by a decrease in both ordering and volume fraction (Figure 4.3 (c-e)) for the rods of aspect ratio 8.0. The colloidal volume fractions of the sediments reported in Figure 4.3 are included in Table 4.1.

In Figure 4.4, we plot the effect of polymer concentration on the nematic order parameter (*S*) for the rods of aspect ratios 4.0, 5.0 and 8.0 for the rod sediments that are made at a Peclet number of 10.0. Nematic order parameter (*S*) was computed directly from the orientations of the directors of all rods detected in the confocal microscopy image volumes through image processing. We found that a significant change in ordering results from combining the effects of the depletion interactions with the applied gravitational field. For example, for the rods of aspect ratio 4.0 and 5.0, the nematic order parameter (*S*) increased initially with increase in the polymer concentration. S appears to

attain a plateau value at c/c* ~ 1, beyond which there is almost negligible effect of additional polymer on the degree of orientational ordering.

The sediments comprised of aspect ratio 8.0 rods responded differently to the combination of depletion interactions and applied gravitational field than the small aspect ratio rods ($r \leq 5.0$), as also reported in Figure 4.4. In this case, an initial increase in the polymer concentration led to an increase in nematic order parameter ($S$) . At c/c* ~ 0.5 a maximum in the nematic order parameter was achieved. These sediments were the most highly ordered found under any conditions (S ~ 0.68) – this condition corresponds to the confocal micrographs shown in Figure 4.3c. Further increase in the polymer concentration resulted in a monotonic decrease in the measured nematic order parameter ($S$).

The final volume fractions of the sediment structures for these above mentioned polymer studies of aspect ratios 5.0 and 8.0 rods are reported in Table 4.1. For the sediments of aspect ratio 5.0 rods, we observe a slight increase in the volume fraction with increasing polymer concentration (from $\phi = 0.52$ (c/c* = 0.0) to 0.60 (c/c*= 0.92)). Similar to the behavior of nematic order parameter (Figure 4.2), the sediment volume fraction also reaches a plateau value at c/c* ~ 1. For the sediments of aspect ratio 8.0 rods, a steep increase in the volume fraction occurs for up to c/c* ~ 0.5. Beyond this attractive interaction strength, the sediment volume fraction decreases with increasing polymer concentration.

In the previous Chapter, we investigated the effect of gravitational field on assembly and concluded that the applied gravitational field significantly affects the assembly of hard colloidal rods through a number of mechanisms. The primary

mechanism for orientational ordering is that the applied field acts to densify the suspensions to the volume fraction required for *I-N* transition. The conditions at which orientational ordering in the sediments are achieved correlate well with the theoretical predictions for the I-N transition and the measured local volume fraction of the sediment. Secondary mechanism for orientational ordering are non-equilibrium effects of the field on the quantitative magnitude of the order parameter, some pre-ordering in the isotropic phase. Finally, a role of the rod glass transition was inferred from the affect of field strength on sediment volume fraction.

Here we build upon our Chapter 3 findings to investigate the role of intermolecular attractions on the nematic order parameter of sedimenting rods. We propose that the results for the assembly of attractive rods under sedimentation may be explained by hypotheses similar to those developed in Chapter 3 to explain the assembly of hard rods. That is, the primary role of the applied field is to densify the suspensions to high volume fraction. If the local volume fraction exceeds the I-N transition volume fraction, then an elevated value of the nematic order parameter S results. However, in the cases of attractive interactions, the equilibrium *I-N* transition volume fraction is substantially shifted due to the effect of depletion. That is, the addition of the non-adsorbing polymer affects the competition between translational and orientational entropy that determines the *I-N* phase transition boundaries. In particular, classic work by Stroobants and Lekkerkerker (1994) for equilibrium systems has shown that addition of non-adsorbing polymer broadens the region of coexistence of the isotropic and nematic phases, thereby increasing the value of the nematic volume fraction, $\phi_{nem}$. (In this chapter for future reference we call the increased value of nematic volume fraction $\phi_{nem\_polmyer}$ to

distinguish this from $\phi_{nem}$). In addition, concentration of the polymer in the suspension decides the mechanism of the phase transition i.e. nucleation and growth, spinodal decomposition, aggregation and gelation. In the cases, where gelation is the phase separation mechanism, no macroscopic phase separation into isotropic or nematic pahse is observed, instead a gelled phase is formed. In the next few paragraphs, we explain our results in context with these equilibrium theories of the isotropic nematic phase transition.

We tested the hypothesis that the interesting behavior of Figures 4.2 and 4.3 are explained by shifts in the nematic phase boundary due to the presence of attractive forces between the colloids in the following way. First, in Figure 4.5, we plotted the nematic order parameter versus the dimensionless volume fraction ($\phi/\phi_{nem}$) for all the sediment structures. In this plot we included all the hard rod experimental data from Chapter 3 as well. The $\phi_{nem}$ is the volume fraction at which the nematic phase first occurs (Tjipto-Margo and Evans, 1990) for the hard rod (ellipsoid) equilibrium systems (zero polymer case) [25]. The plot allows us to examine the primary effect of the applied field/volume fraction – that applied field affects the local volume fraction of rods and if the volume fraction is sufficiently large, than orientational ordering will occur. We see that all the values of *S* follow a curve with the exception for polymer data for aspect ratio 8.0 rods. These polymer data points appear significantly shifted by a constant on the volume fraction axis.

As discussed earlier, work from Stroobants and Lekkerkerker (1994) has suggested that adding polymer to a suspension of rods increases the isotropic-nematic coexistence region. Therefore the volume fraction at which the nematic phase,

($\phi_{nem\_polymer}$) is first observed is higher than the equilibrium $\phi_{nem}$ for hard rods. The value of $\phi_{nem\_polymer}$ increases with increasing polymer concentration and the effect is more significant for large aspect ratio rods. Therefore, in plot 4.5, we should de-dimensionalize the volume fraction with $\phi_{nem\_polymer}$ instead of $\phi_{nem}$ for the case of polymer studies. However, it is difficult to extract the exact value of $\phi_{nem\_polymer}$ for our experiments from the available simulation and theoretical work, due to the specific values of the parameters in our experiments differ from those considered in the prior literature. Nevertheless, simulations suggest that the value of $\phi_{nem\_polymer}$ is likely between 1.25 $\phi_{nem}$ to 1.75 $\phi_{nem}$ for our set of experiments for rods of aspect ratio 8.0. Given this range, if the volume fraction of the polymer data is de-dimensionalized with $\phi_{nem\_polymer}$ instead of $\phi_{nem}$, there is a good probability that the data would follow the same curve as the remainder of the data.

The above analysis suggests that our hypotheses that: (i) volume fraction governs the phase transition and determines the value order parameter, (ii) gravitation field helps densifying the sediment and (iii) addition of non-adsorbing polymer increases the nematic transition volume, are consistent with our experiments.

To understand the non-monotonic dependence of volume fraction on the polymer concentration, in Figure 4.6, we plot $\phi/\phi_{nem}$ vs c/c* for the aspect ratios 5.0 and 8.0 rods. We observe that for low aspect ratio rods (r = 5.0), the volume fraction plateaus at $\phi = 1.4*\phi_{nem}$, with increasing polymer concentration. In contrast, for rods of aspect ratio 8.0, an increase in the sediment volume fraction is followed by a decrease in it, with increasing polymer concentration once c/c* > 0.5. The possible origin for these behaviors (for both small and long aspect ratios) could very well depend on the microscopic phase

separation mechanism that is responsible for macroscopic phase separation. At low and intermediate polymer concentrations mechanisms like nucleation and growth, spinodal decomposition and aggregation take place. These mechanisms lead to macroscopic phase separation into isotropic and nematic phases. However, at high polymer concentrations the relevant mechanism would likely be gelation or vitrification. Note that here, low, intermediate and high values are relative and are dependent on the quantities like aspect ratio or rods and $R_g/D$. For our system, the polymer concentrations at which we observe a switch from a phase separation to a gelation or vitrification mechanism, are $c/c^* = 1.0$ and $c/c^* = 0.5$ for rods of $r = 5.0$ and $r = 8.0$, respectively. When the polymer concentration in the system is increased above these critical concentrations, a phase with arrested dynamics intervenes thereby freezing the dynamics of the rods, solidifying the entire system, and reducing the overall measured ordered parameter [23].

This transition into a dynamically arrested state can explain the observed plateau of the volume fraction for small aspect ratio rods ($r \leq 5.0$). Interference of a glassy state would not allow the suspension to separate into isotropic and nematic phase. Therefore, no further increase in the sediment volume fraction would be seen with increasing polymer concentration (for $c/c^* > 1.0$). van Bruggen and Lekkerkerker (2000) suggested that an increased concentration of non-adsorbing polymer would lead to a lower glass transition volume fraction. That is, the glassy phase would become less dense with increasing polymer concentration. However, we found that this decrease in transitional volume fraction with increasing $c/c^*$ is more pronounced for long aspect ratio rods than small aspect ratio rods and we observed a decrease in the volume fraction of the final

sediments for large aspect ratio rods (r =8.0) with increasing c/c* (once c/c* >0.5). This decrease in volume fraction leads to the observed decrease in the order parameter.

## 4.4. Conclusions

In this work, we studied the effect of depletion forces on the ordering of colloidal rods while they assemble under gravitational field. We found that applying an external field like centrifugation in combination with depletion can help increase the ordering. We also observed that there is optimum polymer concentration, where maximum ordering can be achieved. The aspect ratio of the rods is an important parameter in deciding the optimum concentration of polymer at a particular Peclet number. For rods of small aspect ratios, a continuous increase in the ordering followed by a plateau is observed with increasing polymer concentration, at a fixed Peclet number. In contrast, slightly longer rods behave differently to the combination of depletion and gravitation. An increase in the ordering is followed by a decrease, with increasing polymer concentration for the rods of aspect ratio 8.0 at a fixed Peclet number. The polymer-induced depletion changes the free energy of the suspension and the gravitational force helps densify the suspension and thereby affect the ordering. Polymer concentration also controls the pathways of phase separation from nucleation to gelation. We observe volume fraction of the final sediment is the main parameter in deciding the phase transition, while polymer concentration could push the phase boundaries.

Although studies have been conducted to understand the individual effect of depletion and gravitation on rod assemblies, the combination of the two was not yet been touched upon. In this first attempt of combining the two effects together, we

observed significant contribution from both the factors in the final ordering. We also observed that the combined effect of the two fields on the assembly is the sum total of the effect of the individual phenomenon's. Combination of depletion forces with gravitation helps achieving higher ordering than only gravitation can yield just by itself. This level of control on the ordering of anisometric colloid is really beneficial for the development of advanced materials like photonic band-gap, microelectronics, chemical sensors and energy transfer materials.

**Table 4-1:** Dependence of volume fractions and nematic order parameter of aspect ratio 5.0 and 8.0 rod sediments on polymer concentration (c/c*).

| **c/c*** | **Φ (r = 5.0)** | **S (r =5.0)** | **Φ (r = 8.0)** | **S (r =8.0)** |
|---|---|---|---|---|
| 0.0 | 0.48±0.02 | 0.32±0.03 | 0.41±0.02 | 0.48±0.02 |
| 0.34 | - | - | 0.60±0.02 | 0.60±0.02 |
| 0.52 | 0.56±0.02 | 0.50±0.03 | 0.61±0.02 | 0.68±0.01 |
| 0.92 | 0.59±0.02 | 0.60±0.03 | 0.56±0.02 | 0.50±0.02 |
| 1.23 | 0.62±0.02 | 0.57±0.03 | 0.44±0.02 | 0.34±0.03 |
| 1.48 | 0.59±0.02 | 0.58±0.03 | - | - |

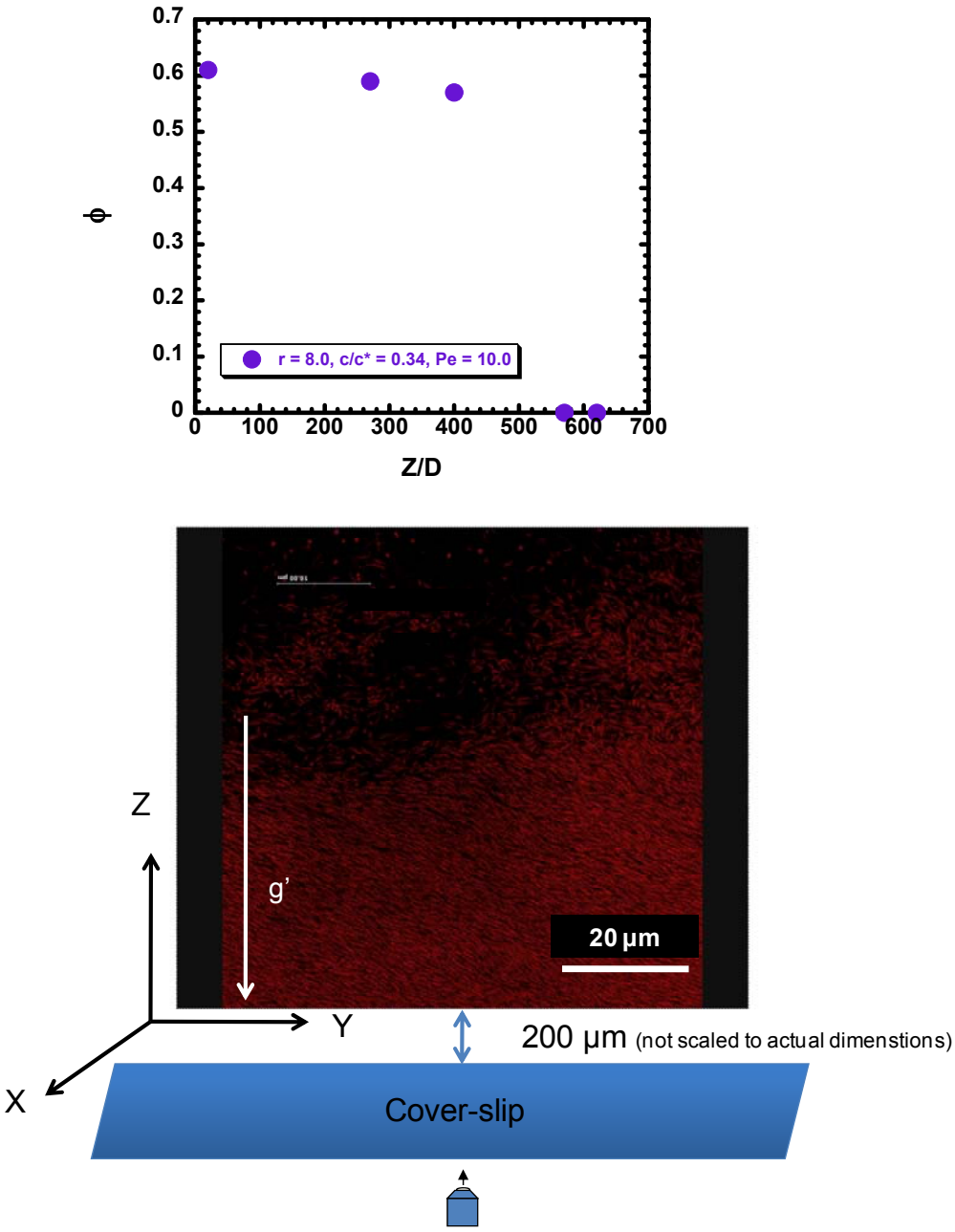


**Figure 4-1:** (a) Dependence of local rod volume fraction on the dimensionless height above the cell bottom for rods of aspect ratio 8.0 ( at c/c* = 0.34, Pe =10.0). (b) Confocal microscopy image of the sediment is showing the transition from dense to sparse sediment structure. The image is acquired at a height of approximately 200 µm above the coverslip in the plane that is parallel to the direction of applied gravitational field.

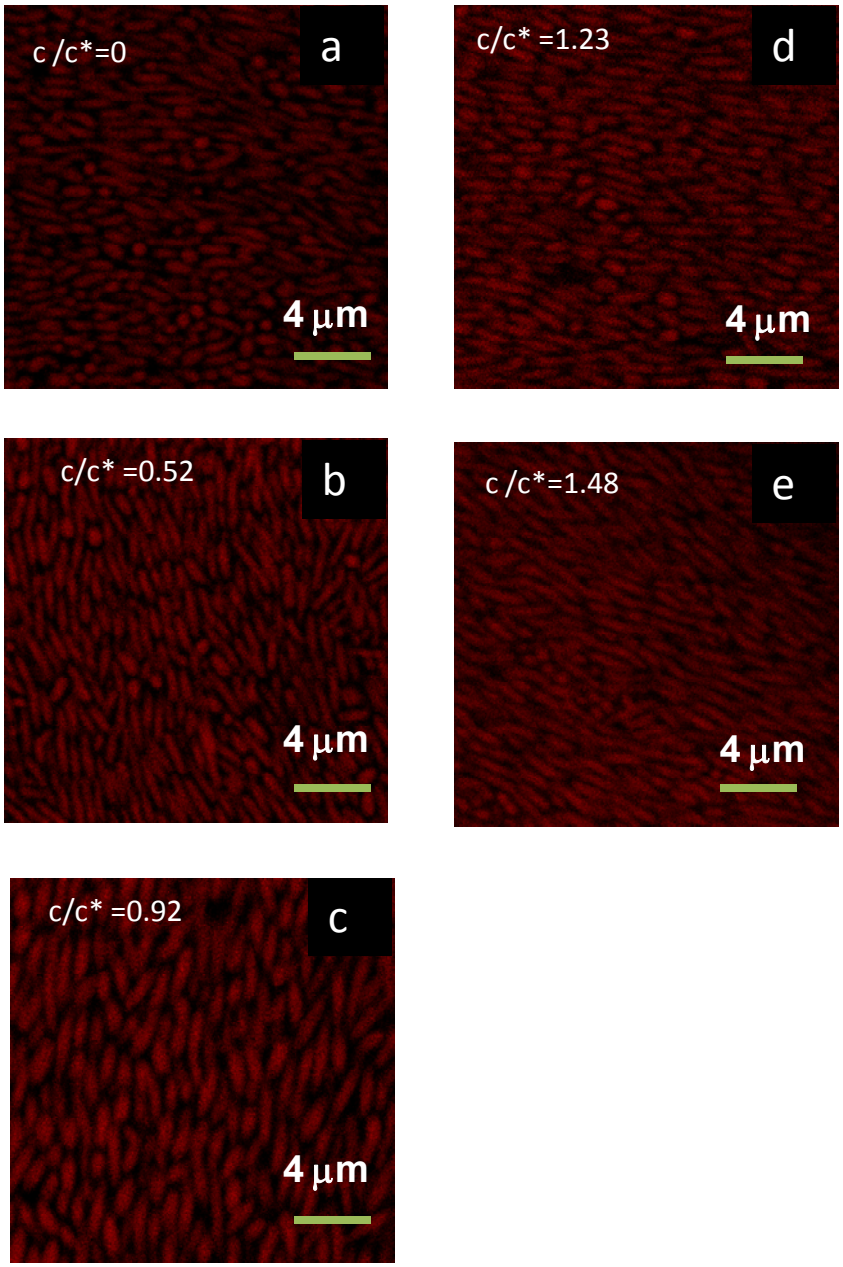


**Figure 4-2:** Confocal Laser scanning microscopy images of sediments of rods of aspect ratio 5.0 made at a Pe =10.0 in the increasing order of polymer conentration. The images are acquired in the plane that is perpendicular to the direction of applied gravitational field.

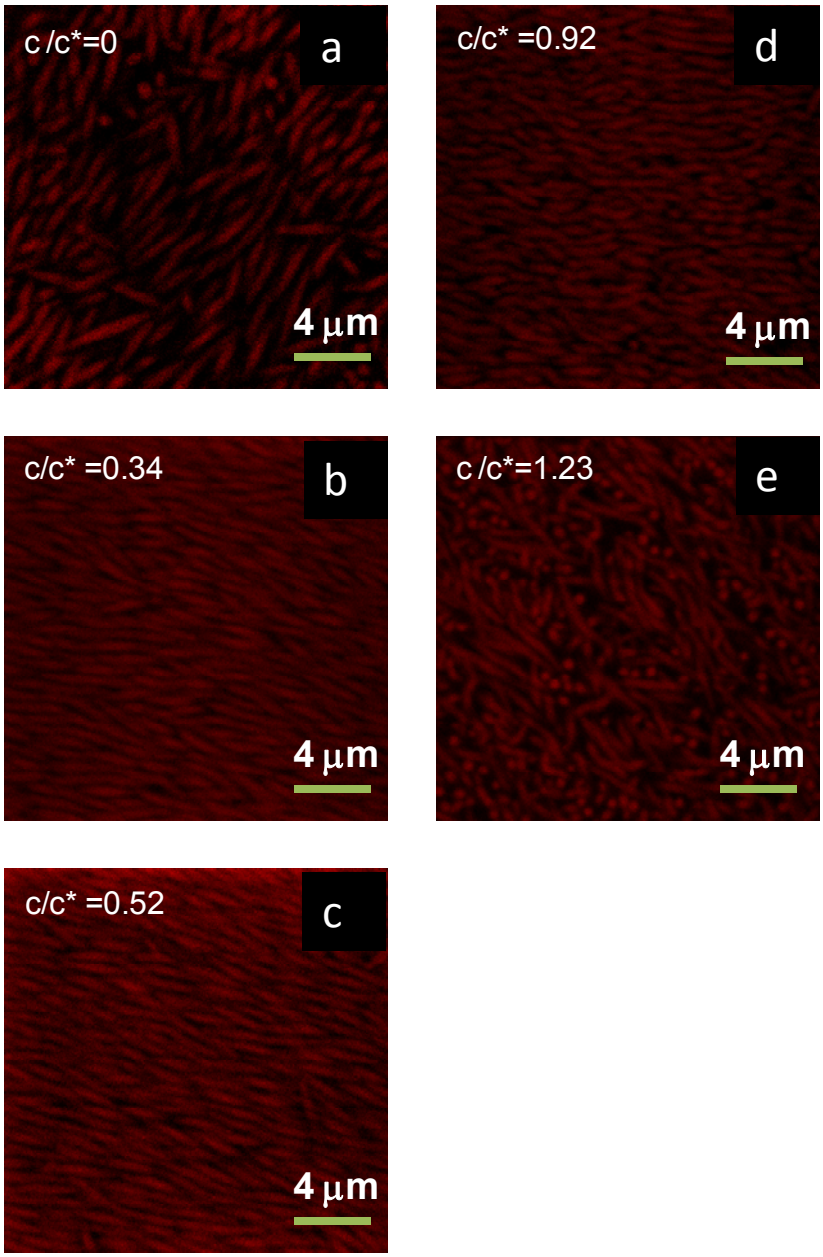


**Figure 4-3:** Confocal Laser scanning microscopy images of sediments of rods of aspect ratio 8.0 made at a Pe =10.0 in the increasing order of polymer conentration. The images are acquired in the plane that is perpendicular to the direction of applied gravitational field.

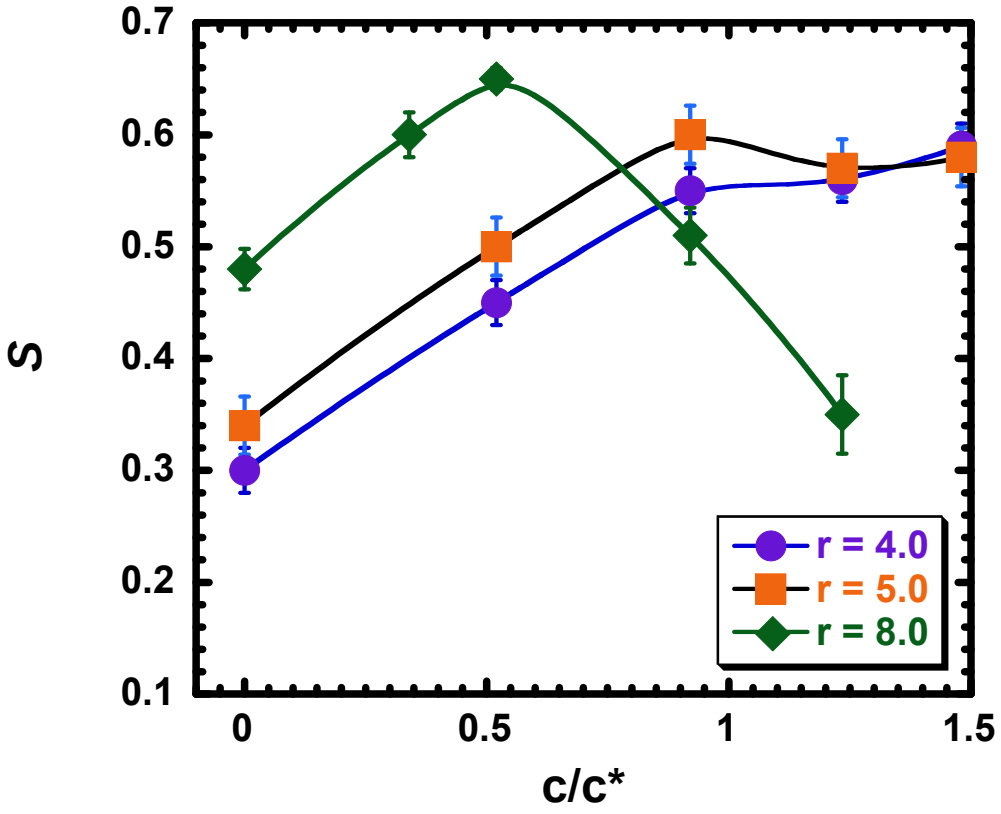


**Figure 4-4:** Dependence of nematic order parameter (S) on the non-adsorbing polymer concentration (c/c*) for the rods of all the aspect ratios 4.0, 5.0 and 8.0.

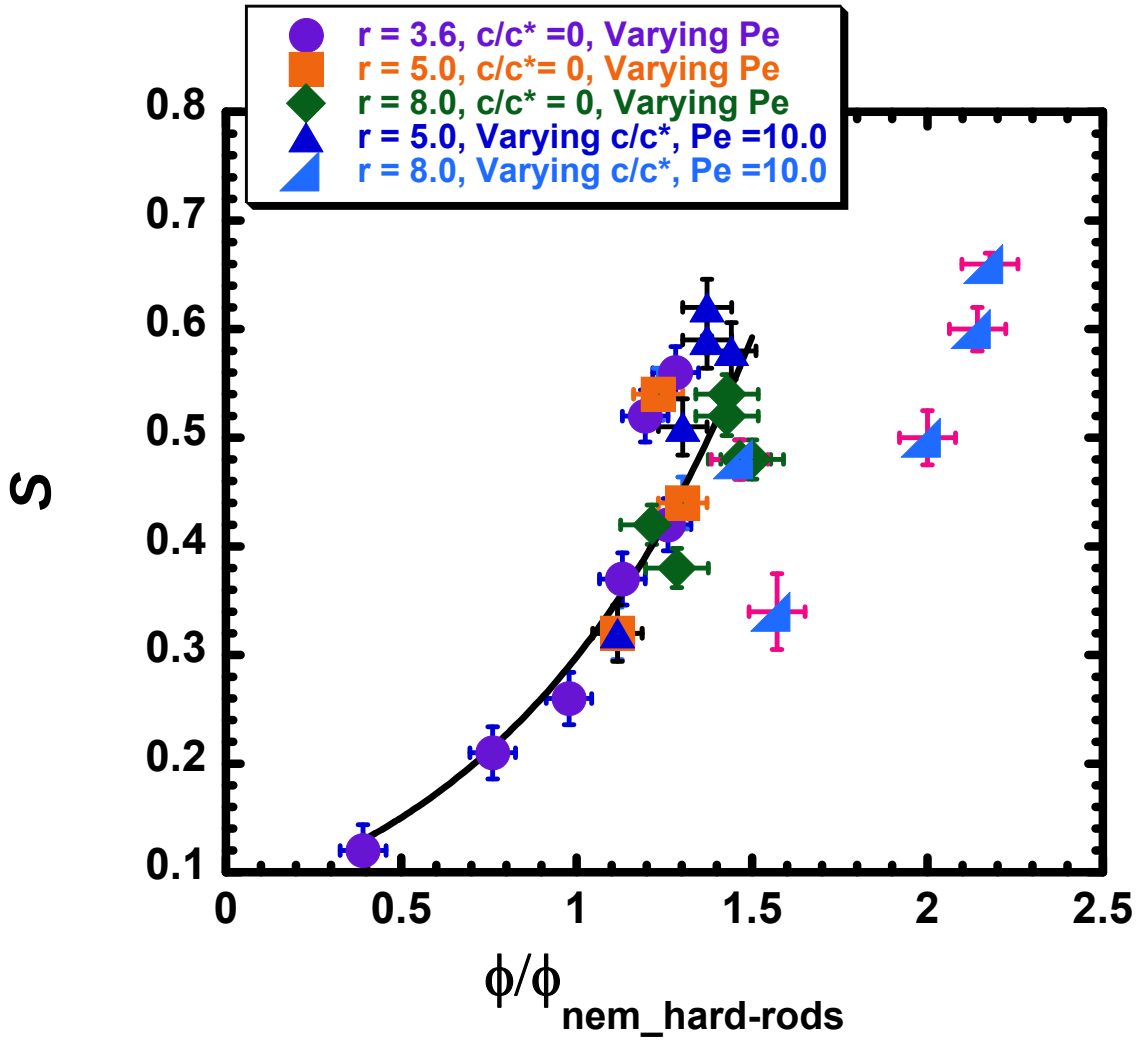


**Figure 4-5:** Plot of Nematic order parameter (S) against the dimensionless volume fractions for all the aspect ratios, suggesting a vital role of volume fraction in bulk phase transition (the values of $\phi_{nem}$ are taken from the theoretical work of Tjipto-Margo and Evans, 1990 for hard ellipsoids).

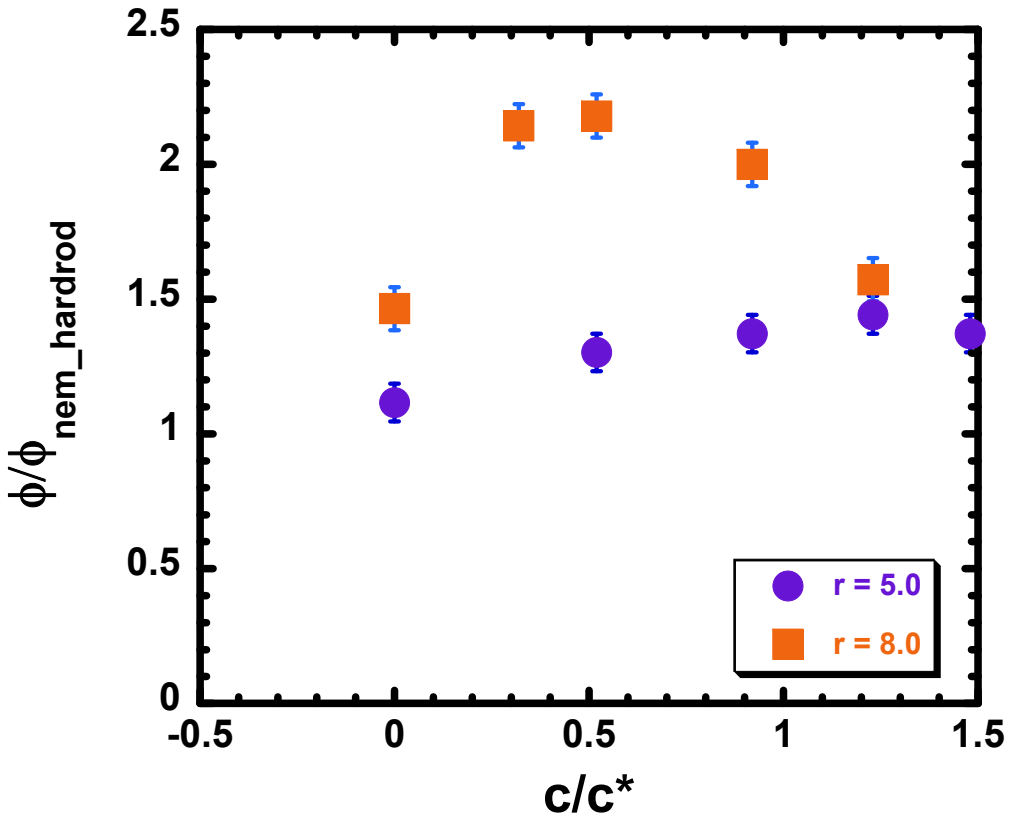


**Figure 4-6:** Dependence of dimensionless volume fraction on the polymer concentration for the rods of aspect ratio 5.0 and 8.0. The values of $\phi_{nem}$ adopted from Tjipto-Margo and Evans, 1990 for hard ellipsoids.

## References


1. R. Cush; D. Dorman; P. S. Russo, *Macromolecules* **2004,** 37, (25), 9577-9584.
2. L. Hong; S. M. Anthony; S. Granick, *Langmuir* **2006,** 22, (17), 7128-7131.
3. M. A. Horsch; Z. Zhang; S. C. Glotzer, *Nano Letters* **2006,** 6, 2406-2413.
4. C. M. van Kats; P. M. Johnson; J. van den Meerakker; A. van Blaaderen, *Langmuir* **2004,** 20, (25), 11201-11207.
5. G. M. Whitesides; M. Boncheva, *Proceedings of the National Academy of Sciences of the United States of America* **2002,** 99, (8), 4769-4774.
6. L. Carbone; C. Nobile; M. De Giorgi; F. D. Sala; G. Morello; P. Pompa; M. Hytch; E. Snoeck; A. Fiore; I. R. Franchini; M. Nadasan; A. F. Silvestre; L. Chiodo; S. Kudera; R. Cingolani; R. Krahne; L. Manna, *Nano Letters* **2007,** 7, (10), 2942-2950.
7. N. Y. Ha; Y. Ohtsuka; S. M. Jeong; S. Nishimura; G. Suzaki; Y. Takanishi; K. Ishikawa; H. Takezoe, *Nature Materials* **2008,** 7, (1), 43-47.
8. Z. Dogic; K. R. Purdy; E. Grelet; M. Adams; S. Fraden, *Physical Review E* **2004,** 69, (5), 051702.
9. A. Nedoluzhko; T. Douglas, *Journal of Inorganic Biochemistry* **2001,** 84, (3-4), 233-240.
10. A. Mohraz; M. J. Solomon, *Langmuir* **2005,** 21, 5298-5306.
11. P. A. Buining; H. N. W. Lekkerkerker, *Journal of Physical Chemistry* **1993,** 97, (44), 11510-11516.
12. H. Maeda; Y. Maeda, *Physical Review Letters* **2003,** 90, (1), 018303.
13. T. Schilling; D. Frenkel, *Physical Review Letters* **2004,** 92, (8), 085505.
14. M. Ripoll; P. Holmqvist; R. G. Winkler; G. Gompper; J. K. G. Dhont; M. P. Lettinga, *Physical Review Letters* **2008,** 101, (16), 168302.
15. V. A. Baulin; A. R. Khokhlov, *Physical Review E* **1999,** 60, (3), 2973-2977.
16. S. Asakura; F. Oosawa, *Journal of Chemical Physics* **1954,** 22, (7), 1255-1256.
17. C. J. Dibble; M. Kogan; M. J. Solomon, *Physical Review E* **2006,** 74, 041403.
18. S. M. Ilett; A. Orrock; W. C. K. Poon; P. N. Pusey, *Physical Review E* **1995,** 51, (2), 1344-1352.
19. M. Adams; Z. Dogic; S. L. Keller; S. Fraden, *Nature* **1998,** 393, (6683), 349-352.
20. H. N. W. Lekkerkerker; A. Stroobants, *Nuovo Cimento Della Societa Italiana Di Fisica D-Condensed Matter Atomic Molecular and Chemical Physics Fluids Plasmas Biophysics* **1994,** 16, (8), 949-962.
21. P. G. Bolhuis; A. Stroobants; D. Frenkel; H. N. W. Lekkerkerker, *Journal of Chemical Physics* **1997,** 107, (5), 1551-1564.
22. S. V. Savenko; M. Dijkstra, *Journal of Chemical Physics* **2006,** 124, (23), 051401.
23. M. P. B. van Bruggen; H. N. W. Lekkerkerker, *Macromolecules* **2000,** 33, (15), 5532-5535.
24. Z. Dogic; S. Fraden, *Current Opinion in Colloid & Interface Science* **2006,** 11, (1), 47-55.

25. B. Tjiptomargo; G. T. Evans, *Journal of Chemical Physics* **1990,** 93, (6), 4254-4265.

# Chapter 5

# Conclusions and Future work

## Conclusions

In this work, we have investigated the dynamics and structure of colloidal rod suspensions by their direct visualization using confocal laser scanning microscopy. Confocal microscopy enables us to characterize the suspensions at single particle level and thereby allows the quantification/ characterization of certain properties that are not possible with other techniques.

In Chapter 2, a direct visualization method is presented to study the Brownian motion of dilute suspensions of colloidal rods in three-dimensional space. Viscosification of the solvents was used to dampen the movement of colloidal particles to the time scales such that capturing of a 3D image volume was possible using confocal laser scanning microscopy without much noise. The full characterization of the motion in 3D was accomplished by characterizing the mean quantities like diffusivity values and distributions of displacement of both translation and rotation. For the first time, rotational diffusivity of colloidal rods was measured using direct visualization. Universal curves were generated for translational and rotational probability distributions that are independent of both aspect ratio and time. Experimental results were found to be in great agreement with theoretical predictions for both diffusivity values as well as probability

distributions. The method can be used effectively to study the dynamics of liquid crystal phases, colloidal glasses and gels, and suspensions subjected to an applied flow[1].

In Chapter 3, we have conducted an experimental study to investigate the role of gravitational field in synthesizing ordered assemblies of colloidal rods. Colloidal rod suspensions at dilute initial particle concentration were subjected to various amount of gravitational force in a centrifuge. Once again use of confocal laser scanning microscopy for imaging was helpful since direct visualization of sediment structure at single particle level allowed us to quantify the ordering. We noticed that the phase transition is principally governed by the volume fraction of the sediment. Gravitational field plays a significant role in desifying the suspension and determining the value of order parameter. We also observed that suspensions of small and long aspect ratio rods respond quite differently to the varying strength of gravitational field. A continuous increase in the ordering was observed with increased field strength for small aspect ratio rods ($r \leq 5.0$), however, the order parameter decreased with increased gravitational field for longer rods ($r= 8.0$) due to formation of a glass phase. The theoretical and simulation work done to understand the effect of gravitational field only considers structural and entropic transition, while dynamic arrest that caused glass transition has not been considered [2, 3]. These experimental results therefore, request development of a new theory; where kinetic and dynamic arrest should also be considered while studying assembly under gravitation.

In Chapter 4, we investigated the possibility of increasing the order parameter of assembly of colloidal rods by introducing gravitational field to the suspensions of attractive rods. Attractive forces were introduced in the form of depletion force by adding

non-adsorbing polymer to the rod suspension. We observed that addition of non-adsorbing polymer during assembly could be beneficial for assembly if optimum concentration of non-adsorbing polymer is used. These optimum concentrations of polymer are a function of rod aspect ratio. Addition of the non-adsorbing polymer to the colloidal rod suspensions affects the phase transition boundaries by broadening the coexistence region, which in effect allows the rods to assemble at higher volume fractions and higher order parameters than compared to hard rod suspensions [4, 5]. The above understanding of phase behavior is really useful for development of advanced materials like photonic band-gap, microelectronics, chemical sensors and energy transfer materials, which require higher degree of ordering.

**Future Work**

The gap between the developed theory and experimental work for anisometric colloids is significant and more experimental studies are needed to verify the developed theory. Direct visualization is a strong technique that can help filling this gap by quantifying almost all the quantities that theory and simulations predicts. The studies in this dissertation present few examples of how direct visualization can help measure the quantities that probe into the dynamics and structure of anisometric colloidal suspensions. The extension of this work would be to use these methods to understand more complex system.

For example, the method we have developed for studying three-dimensional motion of colloidal rods is so far used for dilute suspensions. And a simple next step would be to use the technique to study the internal dynamics of colloidal rod gel

structures. Gels made of colloidal rods behave significantly different than those made of spheres and the method can help understanding the primary reasons behind the differences. Colloidal rod gels can be simply produced by either by adding non-adsorbing polymer to the rod suspension or by introducing any other form of attractive interactions. Also, since the study allows us to characterize the diffusivities of the rods in a system it can be useful to determine the glass transition volume fraction for colloidal rods. The transitional diffusivity of colloidal rods is predicted to be zero in the glass phase [6]. Thereby, design of an experimental system with gradual increase in the volume fraction followed by measurement of translation diffusivity can help achieve the transition volume fraction.

In chapter 3, we identified the use of gravitational field to produce ordered structures of colloidal rods, however the experimental studies were not conducted above an aspect ratio of 8.0 due to limitations in model material synthesis. Most of the theoretical work has been done for long rigid rods and therefore there is a need for experimental work at higher aspect ratios as well. Hence, there is need for an experimental system that is composed of long rigid rods with refractive index matched solvents. Also, we observed a trend reversal of ordering parameter against gravitational field strength when the aspect ratio of rods is increased from 5.0 to 8.0. However, the aspect ratio at which this trend changes is still not known and would need further investigation.

Finally, we have investigated the combined effect of gravitational field and depletion on dilute colloidal rod suspensions. The studies here were conducted for varying polymer concentration while keeping the strength of the gravitational field a

constant. An experimental phase diagram could be useful in understanding this behavior in depth and require that the polymer concentration and gravitational strength be varied simultaneously. Also, the experiments were conducted at a fixed $R_g/D$ (ratio of the polymer radius to the rod diameter), however, theoretical and simulation work suggests a major role is played by this ratio in deciding phase transition [4]. An experimental investigation of the above would be beneficial in verifying the theory as well as could be useful in increasing ordering of the assemblies.

Three-dimensional imaging of colloidal suspensions along with appropriate quantification techniques like image processing could play a major role in understanding the science of anisometric particles. In this thesis, we have taken a step to investigate the dynamics and structure of colloidal rod suspensions using three-dimensional confocal microscopy. Any further extension to this work could help understanding the complexities associated with these systems in greater detail.

## References


1. S. C. Glotzer; M. J. Solomon; N. A. Kotov, *Aiche Journal* **2004,** 50, 2978-2985.
2. V. A. Baulin; A. R. Khokhlov, *Physical Review E* **1999,** 60, (3), 2973-2977.
3. S. V. Savenko; M. Dijkstra, *Physical Review E* **2004,** 70, (5), 051401.
4. H. N. W. Lekkerkerker; A. Stroobants, *Nuovo Cimento Della Societa Italiana Di Fisica D-Condensed Matter Atomic Molecular and Chemical Physics Fluids Plasmas Biophysics* **1994,** 16, (8), 949-962.
5. S. V. Savenko; M. Dijkstra, *Journal of Chemical Physics* **2006,** 124, (23), 234902.
6. S. F. Edwards; K. E. Evans, *Journal of the Chemical Society-Faraday Transactions Ii* **1982,** 78, 113-121.

# Appendix A

# Contact number Measurement

## A.1. Method

In addition to the volume fraction of the sediments along an axis parallel to the applied field, $\phi(z)$, the orientation distribution, $u_i$ and the order parameter S, we also measured the average contact number <c>, for the final sediments. The average number of contacts in a suspension [1] <c>, as reported here, is half of the number of the touching neighbors per particle (i.e. half of the particle coordination number[2, 3]). To measure the average contact number, an estimate of particle shape is required in addition to the centroidal locations and orientation angles. Because the experimental shape of the rods is intermediate between the simple mathematical descriptions of an spherocylinder and a prolate spheroid, we computed contact numbers by approximating the rods as these two reference shapes. Differences in the two methods then determine bounds on the error in the experimentally determined contact number. (For all aspect ratios, the differences between the two methods were small – no more than 10% – and thus the uncertainty in the exact shape of the rods is not a limitation in this analysis.) Below is a brief description of the two methods used to assess the contact number of all rods in the sediments.

Both contact number algorithms are based on calculating the minimum distance between two lines in a 3D space. In this case, those two lines are the rod major axis identified from the image processing centroids and orientation angles. Two rods were counted as contacting if the measured minimum distance between their major axes was less then the sum of their radii at the point of minimum distance.

For the spherocylinder (SC) calculation, a SC of length L and diameter D was constructed by adding a hemisphere of diameter D at the each end of a cylinder of length (L-D) and diameter D. In this model the radius of the rod is taken to be a constant D/2 at all points. For the prolate spheroid (PS) model: a spheroid of length L and diameter D was constructed by overlapping spheres (N = 40 typically) of different radii along the backbone of the rod. The radius of the spheres was systematically varied to fully approximate the spheroidal shape. The performance of the two methods was evaluated by checking the methods for a simulated system of rods. It was found that both of the methods resulted almost the same distribution for most of the cases. However, as the concentration of the rods was increased into the simulated system it was found that PS model results into a more accurate number than SC case. The error in SC case was approximately 8-10%.

## A.2. Results

We used this contact number method to measure average contact numbers of the sediments under gravitational force for both hard and attractive rods. Since the contact probability is density (i.e. volume fraction) dependent, average contact number is a measure of structure. The random contact model described by Philipse relates the average

contact number with the phase transition for hard SCs [1]. The theoretical model is based on excluded volume calculations done by Onsager [4] and Vroege and Lekkerkerker [5]. According to this model, instability in an isotropic hard-rod suspension occurs when average number of contacts per particle is approximately 3.29 and when this value is above 4.19, nematic phase is stable. When the value of the average contact number is between the value of 3.29 and 4.19, a two-phase region is predicted. The model provides us with a relationship between volume fraction (ϕ), aspect ratio (L/D+1) and average contact number (⟨c⟩), given by equation 1.

$$\phi \frac{L}{D}\left[4\frac{D}{L}+\frac{3(L/D)}{3(L/D)+2}\right]=\langle c\rangle \qquad (1)$$

Using our contact number algorithms (both SC and PS models), we measured the average contact number for the gravitational field study for the rods of aspect ratios 3.6 and 8.0 for zero polymer case. In figure A.1, we plot the experimental average contact numbers of the rods in the final sediments (for both the SC and PS shapes) against Peclet number along with the theoretical predictions of the phase transitions. For aspect ratio 3.6 rods, we observe an increase in the average contact number value with increasing Peclet number till Peclet number of 16. However, average contact number does not change much with a further increase in Peclet number after that and stabilizes at a constant value of approximately 4.1. However, for aspect ratio 8.0 rods, the contact number decreases with increasing Peclet number, the trend of the curve for average contact number is similar to its trend for nematic order parameter (*S*) and volume fraction (ϕ).

We found that for our experiments of aspect ratio 3.6 and 8.0 hard rod sediments, the sediments for which we observe high ordering ($S \sim 0.4$) the value of the average

contact number is above 3.29 and close to 4.19 suggesting that these sediments lie either in the two-phase region or stable nematic phase. And the sediments with lower nematic order parameters have average contact number below 3.29. We observe that our results of contact number calculations are in accordance with the theory as well as with the parameters calculated in Chapter 2.

We also calculated the average contact number of the rods sediments made under the combined effect of depletion and gravitational field using our contact number algorithm. In figure A.2, we plot the experimental average contact numbers of the rods in the final sediments (for the spherocylinder shape) and theoretical predictions with respect to increasing polymer concentration for both the aspect ratios 5.0 and 8.0. For aspect ratio 5.0 rods, average contact number of the rods increases with increasing polymer volume fraction as the volume fraction also increases and reaches a constant value of approximately for 4.2. While, for rods of aspect ratio 8.0, an initial increase in average contact number is seen with increasing polymer concentration as the volume fraction also increases and a maximum is reached (~4.5). A further increase in the polymer concentration leads to a decrease in the volume fraction and the average contact number also decreases.

For the above conducted experiments, we find that for sediments that have nematic order parameter ($S$) value above 0.5, the average contact number, $\langle c \rangle$ has a value of $\geq 4.19$. Suggesting, a stable nematic phase; which is also evident from the confocal images. For less ordered sediments ($0.32 < S < 0.50$) the value of $\langle c \rangle$ lies between 3.29 and 4.19, suggesting isotropic to nematic transition region. Therefore, the values of nematic order parameter ($S$) are accordance with the contact number studies.

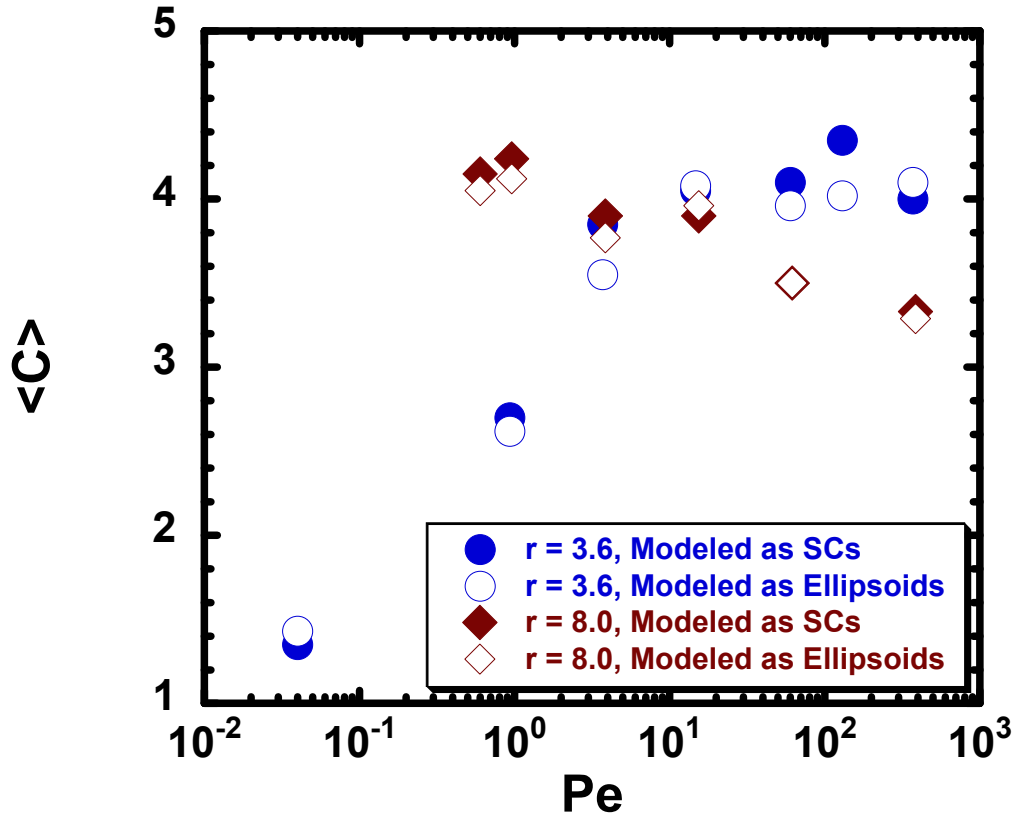


**Figure A-1:** Average contact number of the rods in the sediments plotted against the Peclet number (Pe), measured by assuming both spherocylinder and ellipsoid shape of the rods, for the rods of aspect ratios 3.6 and 8.0.

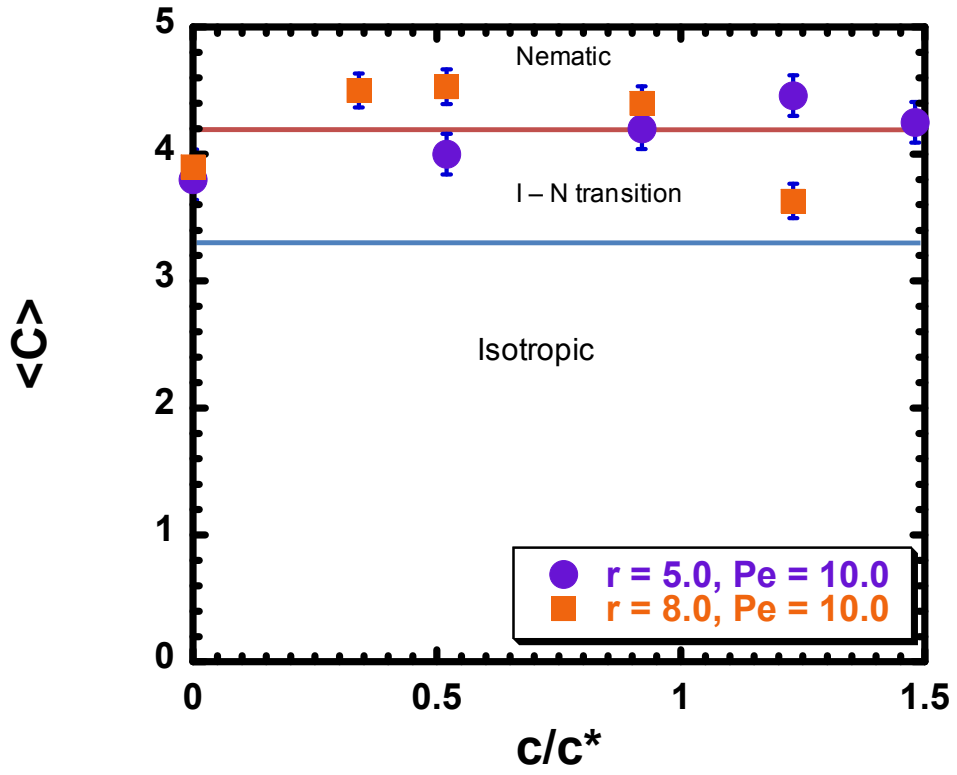


**Figure A-2:** Average contact number of the rods in the sediments of attractive rods plotted against the polymer concentration, measured by spherocylinder shape of the rods, for the rods of aspect ratios 5.0 and 8.0.

## References


1. A. P. Philipse, *Langmuir* **1996,** 12, (24), 5971-5971.
2. S. Sacanna; L. Rossi; A. Wouterse; A. P. Philipse, *Journal of Physics-Condensed Matter* **2007,** 19, 376108.
3. J. Blouwolff; S. Fraden, *Europhysics Letters* **2006,** 76, (6), 1095-1101.
4. L. Onsager, *Annals of the New York Academy of Sciences* **1949,** 51, (4), 627-659.
5. G. J. Vroege; H. N. W. Lekkerkerker, *Reports on Progress in Physics* **1992,** 55, (8), 1241-1309.